Wrocław University of Science and Technology

Doctoral Thesis

Amyloids bio-imaging: two-photon excited autofluorescence and multimodal gold nanoclusters

by

Patryk Obstarczyk, MSc Eng.

Wrocław University of Science and Technology

Faculty of Chemistry

Institute of Advanced Materials

Supervisor:

Joanna Olesiak-Bańska, PhD, DSc, Eng.

Fundacja na rzecz Nauki Polskiej

This research was supported by the First Team program of the Foundation for Polish Science (First TEAM/2017-3/27) co-financed by the European Union.

Wrocław, 2023

Acknowledgments

First and foremost, I would like to express my greatest gratitude to my supervisor, Professor **Joanna Olesiak-Bańska,** for the invaluable guidance and support that she provided during my studies, and throughout my scientific journey. Her profound knowledge, unwavering curiosity, and commitment to excellence have been constantly motivating me to ask questions, formulate and test hypotheses and seek answers, therefore to grow as a scientist. I have had the privilege of working under **Joanna's** supervision and sharing exciting scientific discoveries with her – it shaped how I perceive the world today. I am immensely grateful for every hour of our talks, where impossible matters were often reforged into possible. Thank you for being an exceptional mentor, wonderful person and for showing me what being a true leader means.

I would further like to thank Professors **Marek Samoć**, **Nonappa,** and **Thomas Bürgi** for their precious time spent on our joint projects. I am grateful for all the opportunities they have provided me to expand my knowledge and skills – it is an honor.

I am thankful beyond words to my wife **Kasia** who always believed in me and constantly inspired me. Thank you for your patience, understanding, and support that bloomed into our success. You are the reason why I carried on through all the downs along the way, and – because I love you – I intend to still do so and never give up. I dedicate this dissertation to you.

I would like to express a very special acknowledgment to **Anna Pniakowska**, **Maciej Lipok**, **Agata Hajda,** and **Manuela Grelich-Mucha**, as you shaped the friendly and positive environment at work, even in the hardest times. It is not possible to briefly describe all of our adventures, however, I would like you to know that I am thankful for every lunch, drink, and activity outside the laboratory. With people like you, I felt like I belong. You are irreplaceable and I wish you all the best!

In addition, I would like to thank **Dr. Andrzej Żak**, who contaminated my mind with the passion to transmission electron-microscopy, I hope it will never disappear. It was exciting to jointly do all the detective work within the frames of the famous "*bottom*", where at, allegedly, "*there's plenty of room*". Thank you for your time, passion sharing, and all the long talks outside the work.

I like to also thank **Sylwia Nowak** and the Laboratory of Microscopic Techniques, Faculty of Biological Sciences (University of Wroclaw) for help with the TEM sample preparation. It was a pleasure to discuss and overcome the challenges behind the preparative methodology with you.

Next, I would like to thank **Dr. Karol Synoradzki**, **Dr. Kamil Ciesielski,** and **Izabela Wolańska** for the moments that we shared before I ultimately decided to choose science. Please accept my heartfelt thanks for our collaboration as well as the laughs and talks along the way. It was you who initially showed me an alternative carrier pathway, where wonders of the unknown are explored daily. Thank you for introducing me to the world of scientists.

I am grateful to all people from the Institute of Advanced Materials (from Wroclaw University of Science and Technology) that I have had a chance to interact with. The quality of your scientific work is exceptional, at every level – from students to professors. It was a pleasure to participate in our seminars to absorb the knowledge, discuss all the remarkable ideas, and work alongside the aspiring scientists.

Last but not least, I would also like to thank **Ewa Kawińska** and the rest of the administration team, who kept me informed and took care of all the necessary documentation throughout my studies.

You are changing the world, please keep going – thank you all for your commitment!

Abstract

Despite the remarkable progress in modern medicine, numerous pathological conditions associated with aging (e.g. Alzheimer's, and Parkinson's diseases), due to their complex nature, remain uncurable. It is well-established that the aforementioned neurodegenerative diseases are linked with self-assembly (aggregation) of misfolded proteins – amyloids - which were found in the form of plaques or intracellular inclusions in *post-mortem* examined tissues. However, amyloids are structurally intricate and their role in pathology persists elusive. Therefore, the elucidation of the structural properties of amyloid fibrils is of great importance. The development of new amyloids bio-imaging techniques may provide insight into their formation mechanism, bio-functions (including toxicity), and, in further perspective, contribute to the progress in the development of novel therapeutic strategies.

This doctoral thesis presents the results of interdisciplinary research on amyloid bio-imaging, based on the selected imaging techniques (*i.e.* fluorescence, two-photon, polarized light, atomic force and electron microscopies) and exploring various aspects of imaging (*i.e.* multimodality, label-free imaging and functional labelling). Within the framework of this thesis, polarization-sensitive two-photon microscopy was utilized to image the organization of amyloid fibrils by analysis of conical distribution of two-photon excited emission dipole moments of amyloids intrinsic fluorescence (autofluorescence). As shown on an ordered model, namely amyloid spherulites, two-photon excited emission of amyloids is highly polarized and distributed in a 29° cone around the long fibril's axis. Therefore, I correlated the two-photon excited intrinsic fluorescence of amyloids with the orientation of fibrils in the sample plane, which is a promising tool for label-free amyloid imaging. Additionally, the data derived from the fluorescence imaging were supported with transmission electron microscopy (TEM) imaging. In detail, the ultra-thin cross-sections of fixed amyloid spherulites were investigated under TEM and the resulting images allowed to discuss the ultrastructure of the spherulite, *i.e.* to localize and describe regions of distinctive fibrils organization and amyloid structures contents. Correlated TEM and fluorescence imaging confirmed that the as-discovered polarization-dependent two-photon excited amyloid autofluorescence can report on and differentiate between well-developed amyloids fibrils from the amorphous structures, intermediate states or distorted fibrils. In general, the heterogenous internal structure of spherulites was successfully resolved. This discovery is of great significance and may contribute to a better understanding of amyloidogenesis at various levels of amyloid plaque formation. Last but not least, the scientific endeavors related to the synthesis, characterization, and application of ultra-small gold nanoclusters stabilized with a supramolecular ligand (12-crown-4 ether) for functional and multimodal amyloid imaging are presented. Presented herein nanoclusters are characterized by a molecule-like optical behavior (discrete electronic structure), near infra-red (NIR) fluorescence, amphiphilicity, and high electron density. Therefore, they were applied for amyloid spherulites and fibrils staining and imaging under fluorescence and electron microscopy, respectively. I showed that 12-crown-4 ether-capped gold nanoclusters exhibit a high affinity to hydrophobic bio-surfaces. In contrast to hydrophilic markers, my nanoclusters immediately bonded to amyloid spherulites and their pattering on

individual amyloid fibrils corresponds to the spatial distribution of domains with hydrophobic amino acids. Therefore, I presented the potential of nanoclusters as multimodal markers in the structural characterization of bio-interfaces based on its amphiphilic character.

Abstract in Polish (Streszczenie po polsku)

Pomimo niezwykłych postępów we współczesnej medycynie, wiele chorób związanych ze starzeniem się (m.in. choroba Alzheimera i Parkinsona), ze względu na swój złożony charakter, pozostaje nieuleczalna. Powszechnie wiadomo, że wspomniane powyżej zespoły chorobowe (zaliczane do chorób neurodegeneracyjnych) są związane z samoorganizacją (agregacją) nieprawidłowo sfałdowanych białek – amyloidów – których obecność w postaci blaszek lub inkluzji wewnątrzkomórkowych stwierdzono w tkankach przebadanych *post mortem*. Jednakże amyloidy są strukturalnie skomplikowane, a ich rola w patologii chorób neurodegeneracyjnych wciąż stanowi przedmiot debat. Z uwagi na powyższe, opis właściwości strukturalnych włókien amyloidowych ma ogromne znaczenie. Rozwój nowych technik bio-obrazowania amyloidów może zapewnić wgląd w mechanizmy ich powstawania, funkcje biologiczne (w tym toksyczność), a w dalszej perspektywie, przyczynić się do postępu w rozwoju nowych strategii terapeutycznych.

Niniejsza rozprawa doktorska przedstawia wyniki interdyscyplinarnych badań nad bio-obrazowaniem amyloidów, w oparciu o wybrane techniki (tj. mikroskopie: fluorescencyjną, dwu-fotonową, polaryzacyjną, sił atomowych i elektronową) i aspekty obrazowania (tj. multimodalność, obrazowanie bez znaczników i obrazowanie z funkcjonalnymi znacznikami). W ramach niniejszej pracy czuła na polaryzację mikroskopia dwu-fotonowa została wykorzystana do obrazowania ułożenia włókien amyloidowych przez analizę właściwej włóknom amyloidowym auto-fluorescencji i rozkładu kątowego związanych z nią momentów dipolowych emisji wzbudzonej dwoma fotonami. Praca ta pokazuje, na podstawie uporządkowanego modelu (sferolit), że auto-fluorescencja amyloidów wzbudzona dwoma fotonami jest silnie spolaryzowana, a jej dystrybucja kątowa rozmieszczona jest w zakresie 29° wokół długiej osi włókna amyloidowego. Oznacza to, że wzbudzona dwoma fotonami autofluorescencja pochodząca od włókien amyloidowych została pioniersko skorelowana z ich orientacją w płaszczyźnie próbki. Stanowi to obiecujące narzędzie do obrazowania agregatów białkowych (amyloidów), bez wstępnego barwienia jakimikolwiek znacznikami. Następnie, badania nad nieliniowymi właściwościami optycznymi amyloidów zostały rozszerzone. W efekcie, zobrazowano lokalne uporządkowanie w super-strukturach amyloidowych – sferolitach – ponownie, bez wykorzystania znaczników fluorescencyjnych. Dzięki wprowadzeniu skorelowanego obrazowania mikroskopii fluorescencyjnej i transmisyjnej mikroskopii elektronowej (TEM) odkryte zostało, że wspomniana wcześniej zależna od polaryzacji i dwu-fotonowo wzbudzana auto-fluorescencja włókien amyloidowych może zostać wykorzystana do ich detekcji i wyróżnienia zniekształceń strukturalnych, stanów pośrednich, jak i amorficznych agregatów. Połączenie obu technik pozwoliło na zobrazowanie heterogenicznej struktury wewnętrznej sferolitów amyloidowych. Odkrycie zaprezentowane w ramach tej pracy ma duże znaczenie w kontekście badań nad genezą struktur amyloidowych, ponieważ może zostać z powodzeniem wykorzystane na różnych etapach ich agregacji – bezinwazyjnie. Następnie, przedstawiono prace naukowe związane z syntezą, charakteryzacją i zastosowaniem ultra małych nano-klastrów złota stabilizowanych ligandem supramolekularnym (eterem koronowym). Materiał ten został zaprojektowany do funkcjonalnego i multimodalnego obrazowania agregatów białkowych – amyloidów. Prezentowany w ramach tej pracy nano-materiał charakteryzuje się dyskretną strukturą elektronową, fluorescencją w bliskiej podczerwieni (NIR), amfifilowością i wysoką gęstością

elektronową. Z uwagi na wspomniane właściwości, został on wykorzystany do barwienia i obrazowania sferolitów oraz włókien amyloidowych, odpowiednio, pod mikroskopem fluorescencyjnym i elektronowym. Co więcej, nanoklastry stabilizowane eterem koronowym wykazują wysokie powinowactwo do hydrofobowych powierzchni dostępnych w materiałach pochodzenia biologicznego. W przeciwieństwie do znaczników o charakterze hydrofilowym, wspomniane nanoklastry natychmiast wiążą się ze sferolitami amyloidowymi. W przypadku włókien, organizacja klastrów na ich powierzchni tworzy wzór odpowiadający przestrzennemu rozmieszczeniu domen z hydrofobowymi aminokwasami. W związku z powyższym, amfifilowe właściwości zaprezentowanych nanoklastrów są potencjalnie atrakcyjne dla funkcjonalnego obrazowania szeregu różnych struktur biologicznych.

Research aims and objectives

Intracellular inclusions and structurally complex plaques composed of proteinous and fibril-like structures are linked to a variety of age-related pathologies, including Alzheimer's disease, Parkinson's disease, and type II diabetes. The aforementioned structures, classified by a characteristic cross-β organization, are called amyloids. A comprehensive understanding of amyloid formation, structure, and pathology is of great importance for the societies of the 21 century, as life expectancy tends to grow and amyloids are linked with the age related and uncurable diseases. Although plenty of amyloid structures have been resolved with near-atomic resolution due to the most recent advances in structural biology (based on cryo-electron microscopy and solid-state NMR spectroscopy), their relationship with life-threatening diseases is still poorly understood. Interestingly, these proteinous structures develop a peculiar intrinsic optical properties (e.g. intrinsic fluorescence – autofluorescence), which origin is widely debated.

What is the most important, recently reported breakthroughs in amyloid structural characterization have not been translated yet into effective therapies to successfully treat amyloid-related diseases. Several factors related to this problem can be enlisted:

- **The complexity of the diseases** – Amyloid-related diseases are multifaced as they involve multiple tissues and biological processes. It is challenging to develop drugs and therapies targeting amyloids without potential side effects. Additionally, it remains under debate whether targeting amyloid structures is an appropriate treatment strategy. Moreover, it is still unclear why some people, with significant accumulation of amyloid-like structures in the brain, do not develop Alzheimer's disease symptoms.
- **The complexity of the amyloid structures** – Studies performed over the last 5 years indicated that the same protein can form multiple structural forms of amyloids, *i.e.* polymorphs. The role of amyloid polymorphism in pathology is barely known, however, it cannot be neglected if any pharmacological studies are planned.
- **Difficulty in diagnosis** – Despite the remarkable progress in modern bio-imaging, most of the imaging techniques are not suitable for *in vivo* applications, e.g. cryo-TEM can be performed solely for *ex vivo* or *in vitro* samples. Therefore, it is challenging to detect, and characterize the amyloid-like deposits at the early stages of disease development, which might be crucial for a successful treatment.
- **Lack of universal markers** – The remarkable number of fluorescent probes able to stain amyloids have been designed. However, due to their chemical composition (organic compounds), their application in multimodal imaging (cross-platform imaging, where an image is generated due to distinctive physical processes, e.g. fluorescence, and electron scattering) is severely limited. However, recently reported probes based on nanomaterials are promising due to their unique physicochemical properties. Unfortunately, the main drawbacks of the majority of amyloid-specific staining agents are the lack of sensitivity for intermediate states of amyloid aggregation (as binding sites are not fully developed in such structures),

excitation and emission in short wavelengths range, as well as limited solubility in water.

Overall, while recent progress in amyloid bio-imaging is promising, more research is needed to comprehensively understand amyloid structure in relation to its function in the development of a disease, for the rapid development of effective therapies.

My research aim is to develop new markers and imaging methods for amyloids. To realize that goal and address the foregoing issues, I formulated a few hypotheses, as enlisted below:

I. It is possible to utilize the intrinsic nonlinear optical properties of amyloids to develop a label-free imaging method based on the two-photon excited fluorescence microscopy.
II. It is possible to utilize the polarization analysis of two-photon excited amyloid autofluorescence to resolve the structural ordering in a densely packed sample and identify the distorted or intermediate states of amyloid fibrils.
III. It is possible to design a near-infra-red emitting and functional probe based on electron-dense nanomaterials (e.g. gold nanoclusters) for multimodal amyloid imaging (fluorescence and electron microscopy).

Dissertation Contents and Overview

In **Chapter I**, I present the definitions as well as the state-of-the-art research review on crucial aspects of amyloids bio-imaging. In detail, five subsections were distinguished, where (1) amyloids, (2) imaging multimodality, (3) gold nanoclusters (4) multiphoton microscopy, and (5) crown ethers are discussed, respectively. Therefore, **Chapter I** provides the necessary theoretical background allowing to fully understand the ideas behind my interdisciplinary scientific endeavors.

Chapter II is focused on the description of the custom-built polarization-sensitive two-photon excited fluorescence microscopy (PS-2PFM), which is my method of choice in amyloids autofluorescence imaging. Therefore, **Chapter II** was introduced to explain the assumptions and operating principles of my main experimental method. However, one should note that my research is based on multiple imaging and spectroscopic techniques, which are described in the following chapters (**III** – **V**).

Chapter III contains the experimental results as well as the discussion on the two-photon excited amyloids autofluorescence and angular relationship between the long axis of amyloid fibrils and the corresponding autofluorescence polarization. Therefore, In **Chapter III**, I show that polarization analysis of intrinsic nonlinear optical properties of amyloids can reveal information on their orientation and structure.

Chapter IV is devoted to the idea of structural bio-imaging of complex amyloid superstructures – spherulites. I show that the research results described in chapter no. III can be utilized to resolve the structure of densely packed amyloids. I compare the two-photon excited amyloid autofluorescence and Thioflavin-T dye two-photon excited emission and discuss their utility to resolve the local organization of amyloid fibrils and the possibility of detection of amyloid intermediate states.

Chapter V is focused on the idea of multimodal imaging of amyloids. I describe the design and synthesis of electron-dense, amphiphilic and near-infrared fluorescent nanoclusters stabilized with a supramolecular ligand. Additionally, I utilize the peculiar physicochemical properties of these clusters for bio-imaging of insulin amyloid fibrils and spherulites at micro- and nano-scale, with fluorescence and electron microscopy.

Finally, in **Chapter VI**, I present the general conclusions derived from my research with comments on their scientific impact. The aforementioned chapter is also supplemented by the discussion on perspectives regarding future research.

Table of contents

CHAPTER I – Literature review 13
1 Amyloids 14
1.1. Amyloid definition 15
1.2. Amyloids' impact on society 16
1.3. Amyloid superstructures – spherulites 17
1.4. Past, present and future – techniques for studies on amyloids 19
1.5. Insulin amyloids 21
1.6. Amyloid autofluorescence (intrinsic fluorescence) 24
1.7. Amyloid bio-imaging markers 25
2 Multimodality 27
2.1. Imaging modality 28
2.2. Multimodal imaging 30
2.3. Nanotechnology: multimodal markers 31
3 Gold nanoclusters 33
3.1. Gold nanoclusters definition 34
3.2. Gold atom number – towards atomic precision: structure versus optical properties 35
3.3. Ligands importance and functionality 38
3.4. Nanoclusters in bio-imaging 41
4 Multiphoton microscopy 43
4.1. Two-photon fluorescence microscopy: principles and advantages 44
4.2. Multiphoton properties: nanoclusters 47
4.3. Multiphoton imaging of amyloids 49
5 Crown ethers 52
5.1. Crown ethers: structure and functionality 53
5.2. Gold nanoparticles stabilized with functionalized (-SH) crown ethers 54
5.3. Amyloids and crown ethers 55
CHAPTER II – Experimental – PS-2PFM 57
1 Photo-selection: one-, two-, and three-photon excitation 58
2 PS-2PFM: microscope setup and the open cone model 60
CHAPTER III – Results – Two-photon excited polarization-dependent autofluorescence of amyloids . 65
1 Introduction: the scientific problem 66
2 Comments and acknowledgments 67
3 Materials and experimental methods 67
3.1. Chemicals 67
3.2. Amyloid spherulites incubation 67

3.3. Sample preparation for microscopy 68
3.4. UV-Vis spectroscopy 68
3.5. Fluorescence, bright-field, polarized light, atomic force, and scanning electron microscopy 68
3.6. Polarization-sensitive two-photon microscopy (PS-2PFM) – the open-cone model adaptation and additional assumptions 69
4 Results and discussion 71
5 Conclusions 78
CHAPTER IV – Results – Amyloid spherulites: local ordering revealed by polarization analysis of two-photon excited autofluorescence 79
1 Introduction: the scientific problem 80
2 Comments and acknowledgments 81
3 Materials and experimental methods 81
3.1. Sample preparation for TEM imaging 82
3.2. Amyloid spherulites TEM imaging 82
4 Results and discussion 83
5 Conclusions 90
CHAPTER V – Results – Multimodal imaging with gold nanoclusters 91
1 Introduction: the scientific problem 92
2 Comment and acknowledgements 93
3 Materials and experimental methods 94
3.1. Chemicals 94
3.2. Gold nanoclusters synthesis: 12-crown-4 ligand 94
3.3. Gold nanoclusters synthesis: glutathione ligand 94
3.4. Gold nanoclusters phase transfer: preferential solvent and process reversibility 95
3.5. Amyloid incubation: fibrils and spherulites 95
3.6. UV-Vis and FT-IR spectroscopy 95
3.7. Multimodal imaging 96
4 Results and discussion 97
5 Conclusions 108
Chapter VI – Summary and perspectives 109
Bibliography 113
Appendix 126

CHAPTER I – Literature review

In this chapter, I present the definitions as well as the state-of-the-art research on amyloid bio-imaging, which includes the application of nanomaterials and nonlinear optics. Additionally, the idea of multimodal imaging is presented herein.

1 Amyloids

The relationship between the structure, functions and pathogenesis of amyloidogenic proteins, peptides remains not fully understood. Despite the remarkable progress made over the last decades, numerous amyloid-related diseases (*e.g.* Alzheimer's and Parkinson's diseases) persist uncurable. Therefore, an unmeasurable hope is placed in modern science to contribute to the understanding of neurodegeneration, which may be categorized as one of the main scientific challenges in the medicine of the 21st century.

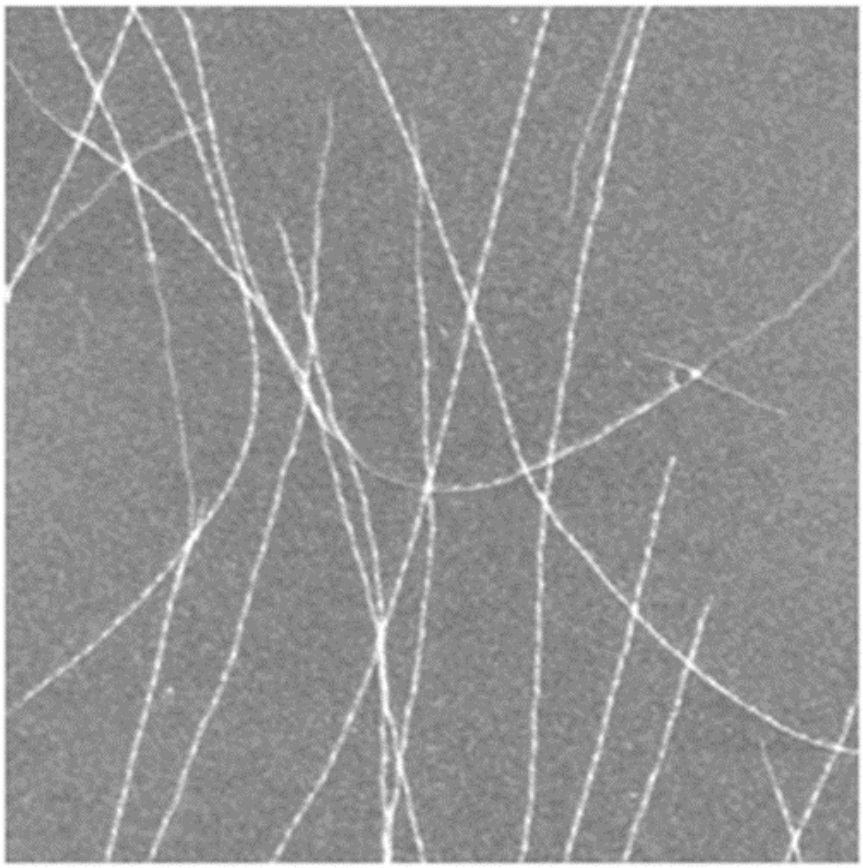

This sub-chapter will introduce the reader to the topic of amyloids, including their definition, impact on society, state of the art research summary, challenges, and perspectives.

1.1. Amyloid definition

Amyloids are insoluble aggregates of proteins and peptides undergoing conformational changes throughout the misfolding process. Amyloidogenic proteins tend to self-organize into fibrils being characterized and distinguished by a repeatedly occurring (every ~4.7 – 4.8 Å) motif of protein secondary structures - β-sheets. They are connected laterally by hydrogen bonds and run perpendicularly to the long fibril axis[1] (see figure no. 1). Two types of β-sheets arrangement are possible: parallel and anti-parallel. Mature amyloid fibrils are usually composed of protofilaments, *i.e.* β-sheet-rich structural components, twisted together. Moreover, distinct fibril morphologies may arise from alternative packing of identical amyloidogenic protein (or peptide) subunits, which gives rise to rich amyloid structural polymorphism[2]. Generally, fibrillar amyloids can be considered as nanostructures due to typical transverse dimensions up to 10 nm. However, their length may vary and ranging up to several micrometers[3]. Up to the present day, roughly 50 proteins or peptides are known to form amyloid fibrils (*e.g.* amyloid-β peptide, tau protein, α-synuclein, insulin, and lysozyme[4]. It is widely accepted that amyloids form *via* polymerization mechanism[5]. In the first step, a protein (or a peptide) partially misfolds and forms stable nuclei, which, in the next step, is followed by the attachment of monomers to the growing ends.

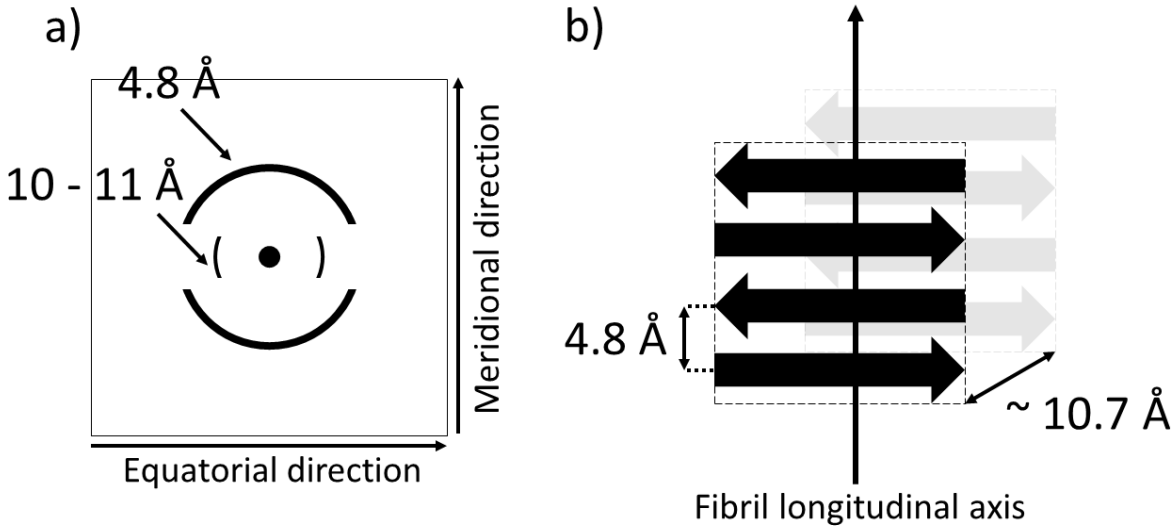

Figure 1. Schematic representation of the characteristic structural features of amyloid fibrils. a) Cross-β spacing obtained from amyloid fibrils X-ray diffraction: bold 4.8 Å refraction pattern corresponds to the hydrogen bonding distance between β-strands and more diffused ~ 10 Å pattern corresponds to the inter-sheet distance, b) repeating anti-parallel arrangement of β-strands relative to amyloid fibril longitudinal axis. The scheme was prepared based on experimental data available in the literature[1, 6].

1.2. Amyloids' impact on society

The accumulation and deposition of amyloid fibrils in multiple organs are the hallmarks of neurodegenerative diseases (e.g. Alzheimer's disease (AD), Parkinson's disease (PD)) with onsets above 65 years of age[6]. AD is a form of neurodegenerative disorder contributing to 70 – 80% of all registered cases of dementia[7]. Moreover, up to date, there are no effective treatments to significantly reverse, halt or even prevent Alzheimer's disease, despite research advances over the past decade. The multifactorial nature of AD and its mechanisms imply the need for diversified studies on amyloids[8]. It is extremely important to be aware that despite an undoubtedly positive increase in human longevity, societal aging may affect economic growth and negatively influence multiple aspects of modern civilization's prosperity and development. Based on recent statistical analysis, *circa.* 45 million people suffer from AD in the United States alone, and this number is predicted to rise threefold by 2050 (to > 135 million cases). According to the mathematical analysis of AD treatment and care costs in European countries, performed by Richard Cimler *et al.*[9], none of the simulated scenarios brings about savings. It is forecasted that the treatment and care costs will be ever-growing: €509 billion in 2030, €828 billion in 2050, and €1038 billion in 2080 (see figure no. 2).

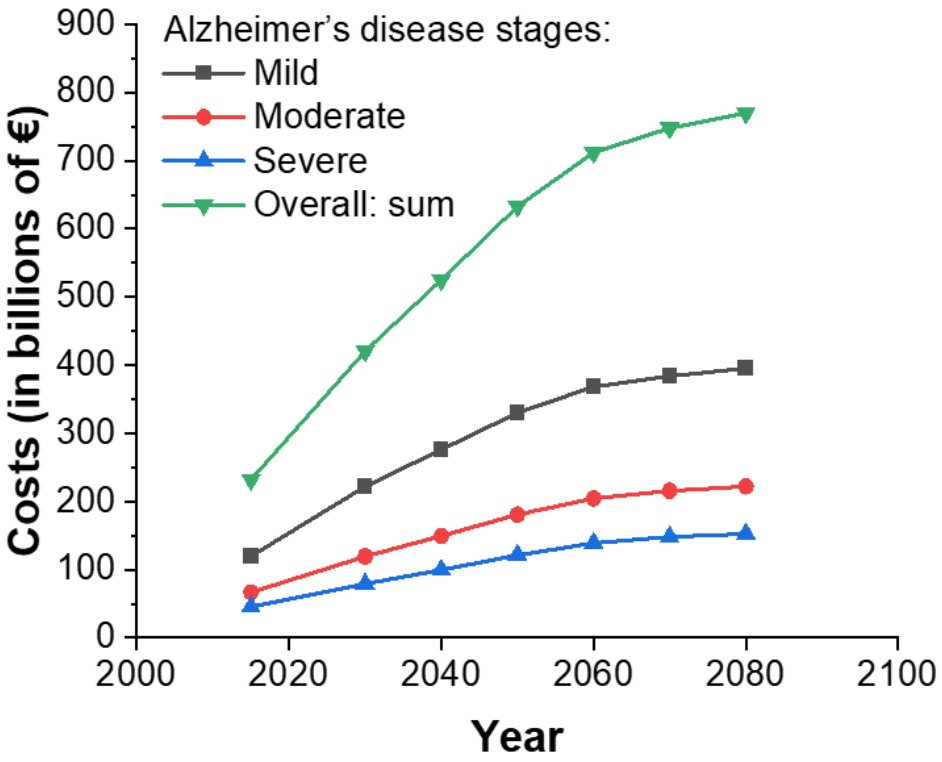

Figure 2. Simulated costs (in billions of EUR) in the 2015 – 2080 timeline for mild, moderate, and severe Alzheimer's disease stages treatment and care. Data acquired from reference no.[9]. Copyright: © 2019 Cimler R, Maresova P, Kuhnova J, Kuca K (2019), Predictions of Alzheimer's disease treatment and care costs in European countries, PLoS ONE 14 (1): e0210958 (https://doi.org/10.1371/journal.pone.0210958).

Additionally, a group of non-neuropathic diseases related to the formation of amyloid fibrils, tangles or plaques has been identified and referred to in scientific and medical literature as amyloidoses[6]. However, as for the AD case, definitively determined causative agents of such diseases are not fully understood and are yet to be identified. There, it is a driving factor for investigations on amyloid structures, functions and pathogenesis for numerous scientists, including me.

1.3. Amyloid superstructures – spherulites

The term "spherulites" is commonly known in the field of synthetic polymers[10-11] where polyethylene is one of the most extensively studied materials known to self-assemble into spherical superstructures. The characteristic feature of spherulitic growth is the regular arrangement of polymer chains, usually radially growing from the less ordered center.

A wide range of proteins exposed to mildly denaturing conditions tends to misfold and aggregate into large polymer-like structures (*e.g.* insulin, amyloid β). Amyloids, in form of fibrils, are commonly recognized and widely studied protein misfolding and aggregation products with a characteristic β-sheet-rich motif. However, several distinct pathways are possible for the protein/peptide, which, besides aggregation, also includes refolding. The relative concentration of the different amyloidogenic protein/peptide states is dependent on the local conditions, thermodynamics, and kinetics[12]. Therefore, a random aggregation and fibril formation as competing processes may result in further self-assembly into spherical superstructures - spherulites[13] (see figure no. 3). Their diameter are ranging up to 150 µm (typically *circa*. 50 µm)[14]. These superstructures have been found in the brain tissues and they have been linked to the onset and progression of Alzheimer's disease[15-16]. Moreover, amyloid spherulites were associated with Creutzfeldt–Jakob disease[17]. However, their exact origin and pathogenesis are under discussion and yet to be discovered.

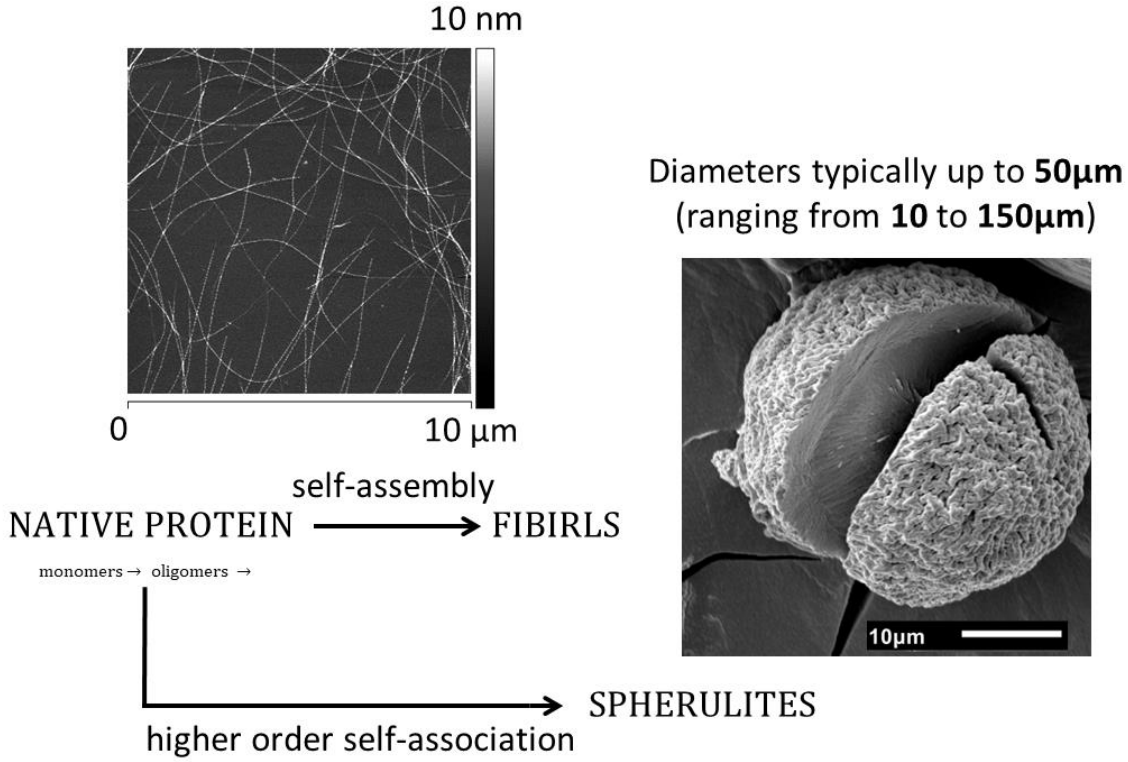

Figure 3. **Scheme presenting native protein aggregation to amyloid structures – fibrils and spherulites.** Initial aggregation leads to the formation of amyloid fibrils (atomic force microscope image (AFM)). However, higher order of self-association may result in the formation of superstructures – spherulites (scanning electron microscope (SEM) image). Own research.

Amyloid spherulites are structurally characterized by core-shell morphology and as imaged under the cross-polarized light microscope they show a distinctive pattern named "Maltese cross" (see figure no. 4). Under crossed polarizers, the contrast arises from the interaction between in plane-polarized light and a birefringent specimen. Without the specimen, the observed plane appears to be blacked out, as crossed polarizers are completely attenuating the light. However, the plane-polarized light can interact with the sample (located between two polarizers) and the light components can become out of phase. By passing the analyzer (second polarizer, located on the top of the sample), the light can be destructively or constructively recombined, which allows to observe the blacked out and bright areas, respectively. "Maltase cross" pattern arises only if observed specimen is characterized by a distinct anisotropic character. In case of spherulites, it is correlated with amyloid fibrils organization. They possess two distinctive refractive indices in correlation to the longitudinal and transverse fibril axis. Moreover, as fibrils (in the spherulite shell) are radially oriented they distinctively refract the incident polarized rays in dependence on their localization in the sample plane. Spherulite core, on the other hand, is nonbirefringent and usually more densely and less regularly packed[18]. It may be composed of distorted fibrils, proteins at various states of aggregation or folding, and α-helix-rich components[14, 19].

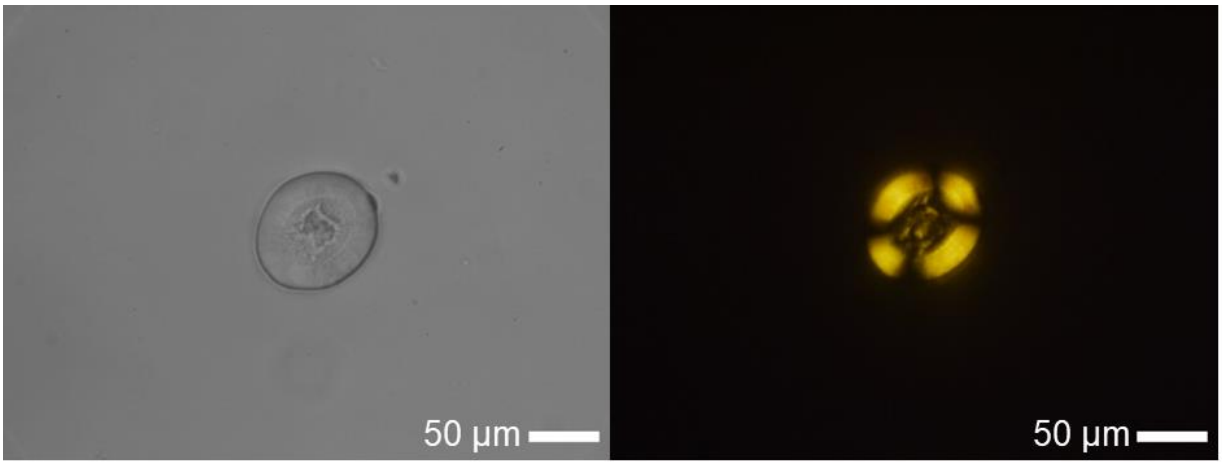

Figure 4. Bovine insulin spherulite. Images were taken under a light optical microscope (left) and with crossed polarizers (right). A characteristic "Maltase cross" pattern is revealed due to the presence of radially organized fibrils and nonbirefringent, less ordered and mostly amorphous core. Own research.

Amyloid spherulites should be reconsidered as semi-crystalline structures that connect protein (or peptide) flexibility with some order of structural rigidity. Recently, it was shown that they are heterogeneous at multiple levels, *i.e.* core-shell morphology of a single spherulite as well as types of spherulitic assemblies within the same sample[20]. Similar to the amyloid fibrils, spherulites also present rich structural polymorphism[19].

1.4. Past, present and future – techniques for studies on amyloids

The history of understanding amyloid folding exceeds from today back to the 17th century. For the first time, amyloids were described in 1639 in studies on the "lardaceous" liver and "white stone-containing" spleen. However, Virchow's work on macroscopic tissue abnormality (stained positively with iodine) allowed him to coin the term "amyloids", as late as 1854. Nevertheless, back in the day, amyloids were misidentified as polysaccharides. The proteinaceous nature of these structures, however, have been discovered in 1859 by Friedrich and Kekulé[21]. These studies were followed by Alois Alzheimer's work on post-mortem brain tissue derived from Auguste Deter (1901). His comprehensive description of the histological alterations, known today as plaques and neurofibrillary tangles, allowed him to link amyloids with neurodegeneration[22]. Later on, subsequent studies based on electron microscopy revealed the presence of fibrillar structures (Cohen and Calkins, 1957)[23-24]. Information related to amyloid fibrils' internal structure, based on β-pleated-sheet conformation, has been discovered via X-ray diffraction analysis performed by Geddes *et al.* [25], in 1968. However, near-atomic structural analysis of amyloids started to be explored in the early 2000s, due to the rapid developments in the methodology (both, for in vitro for ex vivo fibrils preparation) as well as advances in electron microscopy (cryo-) and NMR spectroscopy[1]. Moreover, amyloid polymorphism, as a challenge for molecular imaging and potential therapy, has been studied over the last 5 years, and it is attracting ever-growing attention[2, 26-27].

The biological impact and clinically relevant symptoms may be derived from the amyloid fibril polymorphism and also from the presence of monomers, oligomers, and other intermediate states. As an example, studies on brain extracts of patients diagnosed with AD show distinct size, concentration, and conformational features that correlate with disease severity[28]. Therefore, it is of great importance to employ numerous advanced techniques to obtain as much information on amyloids morphology as possible. I have reviewed the most commonly applied microscopic techniques for the studies on amyloid structure and presented them in a table with a short comment on their capabilities (please see table below, no. 1).

Table 1. A brief review of microscopic techniques employed to investigate amyloid structures.

Technique	Information derived from and exemplary studies
Atomic force microscopy	The commonly used method employed to study fibrils adsorbed on a surface (*e.g.* mica)[29]. Primarily used tool for the initial fibril characterization and determination of fibril size distribution, length, height, width, and a crossover[30]. Suitable for mechanical probing (*e.g.* Young's moduli measurements). Not suitable for the spherulites imaging and *in vivo* experiments , stain-free.
Fluorescence microscopy	Usually based on labeling with fluorescent probes (*e.g.* thioflavin T). Most commonly employed for the initial detection and identification of amyloid fibrils. The non-destructive method. Suitable for hydrated samples. Limited by the diffraction limit, however, super-resolution microscopy has been introduced into the field. State-of-the-art research based on light microscopy allowed for the observation of the aggregation of the amyloidogenic protein at the molecular level: monomers addition to the fibril ends[31]. Moreover, it was also applied to the real-time observations of amyloid spherulite growth[20]. Translatable on *in vivo* experiments[32].
Electron microscopy	Despite the destructive influence of electrons on soft matter[33], electron microscopy, undoubtedly, is the most important set of techniques for modern amyloid research. It has driven the understanding of amyloid structure in the last 20 years. However, it is extremely costly and requires advanced sample preparation[34]. It is not suitable for hydrated samples. Nevertheless, due to remarkable progress in cryo-electron microscopy structural characteristics of amyloid fibrils, with an atomic resolution, have been resolved[35-36].

One should note that modern structural studies on amyloids are advanced and usually employ multiple microscopy techniques at once, and are supported with spectroscopy, x-ray

diffraction analysis or mass spectrometry[37]. Such an approach allows obtaining spatially resolved information regarding sample morphology, as well as some insight into its chemical composition. For instance, methods like fluorimetry, circular dichroism (CD)[38], and Fourier transform infrared (FTIR)[39] are commonly utilized to characterize the secondary structure of fibrils or track their formation (including growth kinetics)[40]. In terms of mass spectrometry (*e.g.* electrospray ionization, side-directed spin labeling), information on the exposed surfaces of fibrils can be obtained[41].

1.5. Insulin amyloids

The insulin molecule is a small globular protein composed of 51 amino acids arranged in two chains, namely: A chain (21 amino acids) and B chain (30 amino acids) being linked by two disulfide bonds. Additionally, one disulfide bond occurs within the frames of the A chain (see figure no. 5). Insulin in its native form is mostly characterized by α-helical secondary structure. It can unfold and aggregate, in a controlled manner, upon change of: protein concentration, elevated temperatures, pH or introduction of metal ions. Despite well described hormonal activity connected with glucose metabolism, insulin also modulate synaptic plasticity and influence signaling pathways in the brain. It participates in the metabolism of amyloid β and tau protein that are constituting the main building blocks of neurofibrillary tangles and also amyloid plaques[42]. Although insulin sequence was fully determined in 1958 and Sanger was awarded a Nobel Price for this achievement, its role in dementia and diabetes, up to this day, is still widely discussed and investigated.

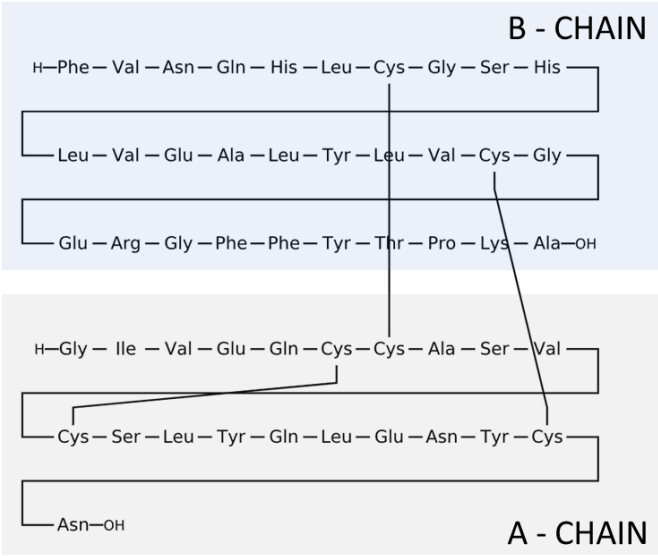

Figure 5. **Simplified bovine insulin molecule amino acid composition.** Image derived from the PubChem database (CID: 90478612, *https://pubchem.ncbi.nlm.nih.gov*).

Insulin gained popularity as a model peptide for amyloid aggregation studies because of its biological significance, accessibility, and primary sequence containing so-called

"amyloidogenic fragments", namely: LVELYL (leucine-valine-glutamic acid-leucine-tyrosine-leucine, B chain), LVEALY (leucine-valine-glutamic acid-alanine-leucine-tyrosine, A chain) and LYQLEN (leucine-tyrosine-glutamine-leucine-glutamic acid-asparagine, A chain)[43]. Amyloidogenic sequences were identified based on the adapted secondary structure, hydrogen bonding, solvent accessibility to the overall surface area, and hydrophobicity. Therefore, the aforementioned properties are crucial for the amyloid formation process and also for the understanding of its pathogenesis.

In terms of structural information, the three-dimensional arrangement of protofilaments composing mature insulin amyloid fibrils has been resolved by cryo-electron microscopy in 2002 by Jiménez *et al.* [44], see figure no. 6.

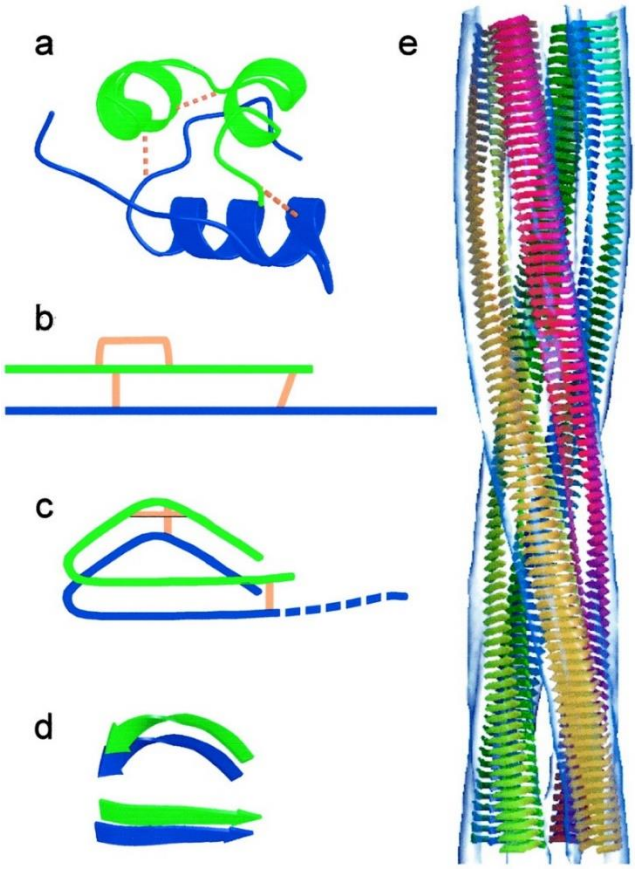

Figure 6. Insulin amyloid fibril model. a), b) Insulin structure (A chain – green, B chain – blue) with three native disulfide bonds (orange lines), c) proposed amyloid protofilament topology, d) β-sheet model of a protofilament, e) four protofilaments (colored separately) β-sheet models enveloped into mature fibrils - allocated within the frames of the experimentally obtained electron density of the fibril (transparent grey boundaries). Image reprinted from the reference[44] (https://doi.org/10.1073/pnas.142459399), Copyright © 2002, The National Academy of Sciences.

Overall, β-sheets, that are constituting the foundation of amyloid protofilaments, accompany the overall mature fibril twist, therefore they are nearly flat-oriented. Protofilaments assemble themselves into pairs (or larger groups) by mutual coiling, which results in a long-range twist. Such morphology originates from the small angle between

initial building blocks: β-strands. Angles in the 1.5 – 2.5° range were observed by Jiménez *et al.*, which corresponded to mature fibril full-pitch repeats of ~1200 – 700 Å, respectively. Their statistical TEM images analysis revealed that a molecule of insulin occupies two β-strands layers along the long fibril axis (for a protofilament with a 30 x 40 Å cross-section). However, distinctive packing within protofilaments is possible and dependent on protein sequence and folding state (*e.g.* due to the constraints arising from disulfide bonds). Moreover, common protofilament units can assemble into fibrils with high structural heterogeneity. Although amyloids possess common β-sheet-based architecture, they also exhibit a rich structural polymorphism at multiple levels (from protofilament build-ups to overall filaments number and their correlative orientation within mature fibrils) and their biological significance remains under debate.

Amyloid fibrils' surface hydrophobicity may highly influence amyloid toxicity. In the case of insulin aggregates, it was studied at the single-particle level with the tip-enhanced Raman scattering (TERS) technique. Deckert-Gauding et al.[45] systematically investigated individual amyloid fibrils at nanometre spatial resolution and correlated their chemical composition with the structural data (see fig. no. 7). It was shown that, in insulin amyloid fibrils, hydrophobic and mixed (partially hydrophobic and hydrophilic) tend to occur alternatively every ~5 or ~10 nm.

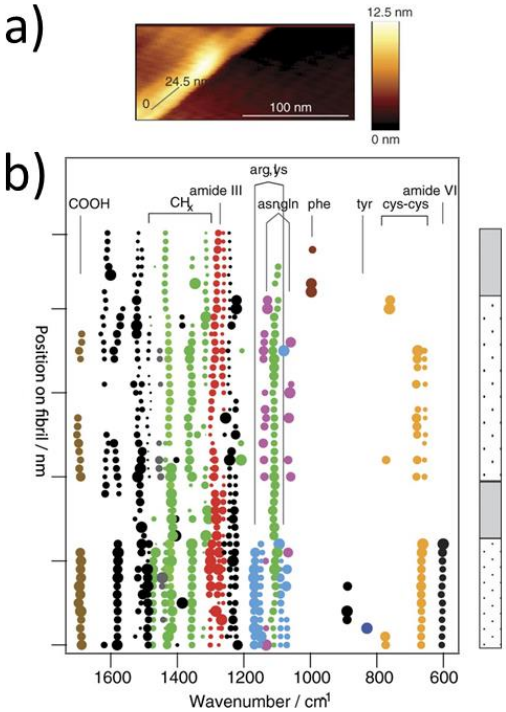

Figure 7. Amyloids surface hydrophobicity spatial distribution. a) AFM topography of an insulin fibril (gray line: an area investigated with TERS technique), b) fitted band parameters derived from TERS spectra. Inset shows the spatial distribution of hydrophobic (gray area) and mixed domains (dotted area) on the scanned fragment of amyloid fibril. The image was constructed from parts of figure no. 1, reprinted from reference[45] (https://doi.org/10.1038/srep33575) under Creative Commons Attribution 4.0 International license.

1.6. Amyloid autofluorescence (intrinsic fluorescence)

Intrinsic fluorescence of proteinaceous structures is usually attributed to the presence of aromatic amino acids (tyrosine, phenylalanine, and tryptophan). For example, tryptophan is the most commonly studied natural fluorophore. Its fluorescent properties (*i.e.* quantum yield (QY), absorption, and emission maxima) are dependent on the microenvironment. In solution, however, it absorbs ~280 nm photons and emits at ~346 nm, with a typical QY up to 20%[46]. Such intrinsic fluoresce, based on natural chromophores, enabled non-invasive studies on numerous biological systems that exclude any molecular perturbation that may arise from the presence of fluorescent probes[47]. Surprisingly, amyloid systems also exhibit intrinsic fluorescence, even if devoid of the aromatic amino acids, *e.g.* amyloid-β fragment (33–42)[48]. The aforementioned amyloid-β fragment, as excited at 450 nm wavelength is characterized by a luminescence (at > 488 nm), with an averaged lifetime in order of nanoseconds. Overall, amyloid systems tends to be luminescent in the 530 – 440 nm range (2.3 – 2.8 eV) , if excided at 380 – 340 nm (3.3 – 3.6 eV). This unique and structure-dependent optical behavior of amyloids, not relying on the presence of aromatic residues or multiple bond conjugation, from now on, will be referred to as “autofluorescence”.

The photophysical mechanisms behind near-UV excitation and characteristic autofluorescence (blue-green emission) of amyloid systems, devoid of aromatic amino acids, remain under debate. However, it appears to be a result of the polypeptide chain folding into a cross-β scaffold, as similar optical properties were reported for crystalline proteins containing a high proportion of β-sheets[49]. It was postulated that hydrogen bonding may be hindering nonradiative relaxations, and simultaneously introducing electron delocalization. A deeper insight into the problem was presented by Pinotsi *et al.*[50] by combining *ab initio* molecular dynamics simulations with fluorescence spectroscopy. They demonstrated that specific H-bonds in amyloid fibrils are permissive to the proton transfer resulting in a double well ground-state potential. In other words, the proton can be found on either the C- or N-terminus of amyloid-like folded amino acids chains (see figure no. 8). Therefore, amyloid-like aggregation alter the relaxation channels as well as absorption spectra of the entire system. In detail, Pinotsi's calculations indicated that the proton transfer mechanism is responsible for lowering the excitation energy levels in amyloids. Moreover, the experimental data show that autofluorescence of amyloid fibrils may be altered upon protonation or deprotonation, namely, to achieve higher and lower QY, respectively.

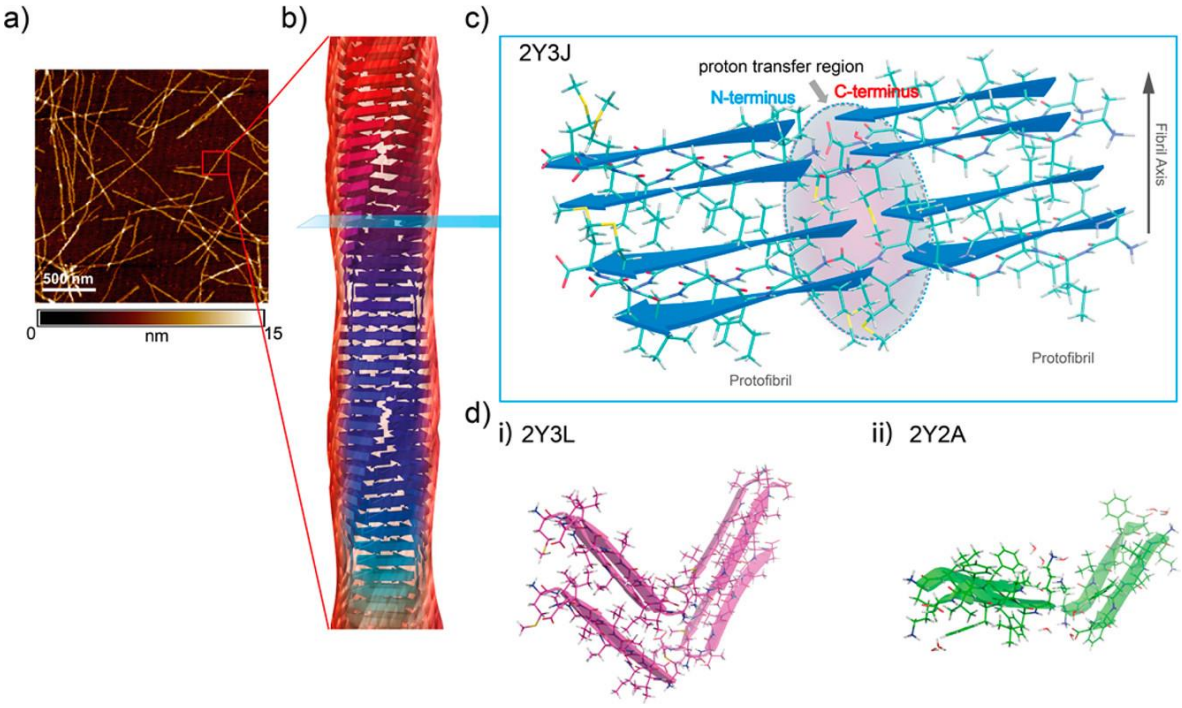

Figure 8. Amyloid autofluorescence – the proton transfer mechanism. a) AFM image of amyloid fibrils, b) schematic view of a 3D protein fibril model (four protofilaments twisted around the common axis), c) depiction of the cross-sections of two adjacent protofilaments creating permissive area (grey) for the proton transfer, d) models of two unit cells constructing mature fibrils (with parallel and antiparallel conformation). Reprinted with permission from reference no.[50] (https://doi.org/10.1021/jacs.5b11012), Copyright © 2016, American Chemical Society.

Grisanti *et al.*[51] also contributed to the field with ab initio static calculations and nonadiabatic dynamics simulations of model amyloids. They proposed that amide groups nπ* states are strongly correlated with amyloids autofluorescence. Moreover, the calculation revealed that the excitation energy of the n→ π* transitions tends to decrease upon deplanarization of the amide group, on which they are localized. Such a phenomenon is possible due to the strong hydrogen bonding that enforces these transitions to be stabilized as energetically lowest ones and emitting in VIS. Therefore, an explanation of amyloid autofluorescence on a molecular level has been proposed.

1.7. Amyloid bio-imaging markers

Simple organic molecules are commonly used as fluorescent labels for amyloid imaging, *e.g.* Thioflavin-T (ThT), Congo Red (CR)[52-54]. The hindrance in free rotation of the amyloid-specific dye upon binding to β-sheet structures suppresses non-emissive relaxation of it and results in a high quantum yield of fluorescence[55]. Thus, such dyes are commonly used for amyloid detection *via* light microscopy as well as for spectroscopy, *e.g.* growth kinetics investigations. Unfortunately, the binding mechanism, dependent on the β-sheet arrangement (see figure no. 9), hinders the sensitivity of ThT and CR for oligomeric forms and other intermediate states of amyloid aggregation[56-57]. It should be noted, however, that the binding mechanism of the ThT to amyloid fibrils is multifactorial and still under debate. Recently, it was

shown that hydrophobic interactions, previously presumed to be the driving factor of ThT binding to fibril surfaces, are also strongly influenced by the positive charge of the dye molecule itself, *i.e.* electrostatic interactions[58]. Moreover, usage in *in vivo* studies of Thioflavin-T, Congo Red (and their derivatives) is also limited[59], due to an emission wavelength below 650 nm. It is beyond the optimal wavelengths from the so-called "biological imaging window" (650 -1350 nm), where light has its maximum penetration through tissues. It also needs to be highlighted that commonly applied fluorescent labels may affect the structural properties of amyloids and the aggregation process itself which is undesirable[60].

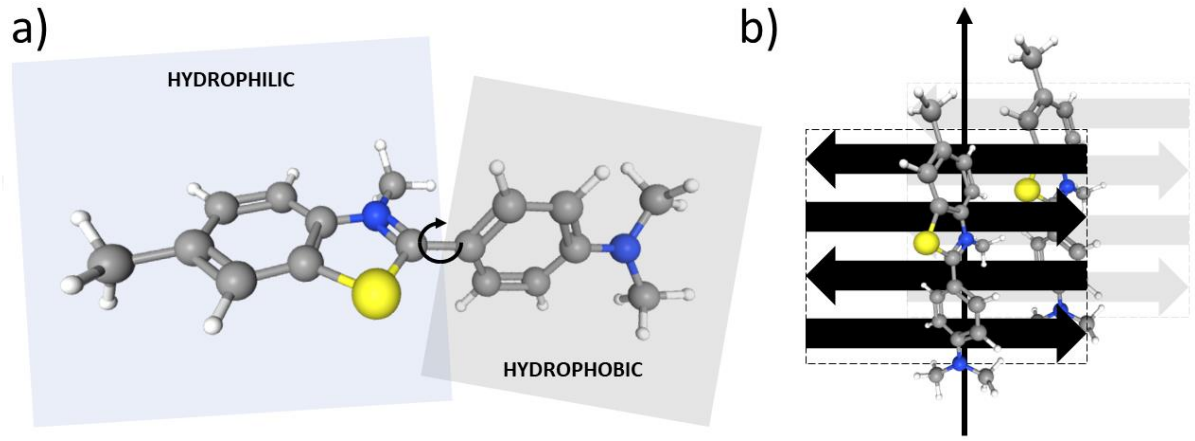

Figure 9. Schematic representation of Thioflavin T structure and binding mode to amyloid fibrils. a) Ball and stick structural model of Thioflavin T (grey – carbon atoms, blue – nitrogen atoms, S – sulfur atom, white – hydrogen atoms) with marked hydrophobic (a dimethyl amino group attached to a phenyl group - grey area) and more polar end (benzothiazole group containing the polar N and S atoms, blue area), b) Schematic representation ThT binding mode to amyloid-like structure (along surface side-chain hydrophobic pockets running parallel to the long axis of the β-sheet arrangement). Molecules are not up to scale. Model based on data from reference no.[55] . Ball and stick model derived from the PubChem database (CID: 16954, https://pubchem.ncbi.nlm.nih.gov).

Despite remarkable progress in the engineering of chemical and optical properties of small organic molecules for amyloid imaging (*i.e.* shift of emission maxima into the NIR (near infra-red) range and the introduction of hydrophilic groups into the molecular framework of the dye)[61], their low electron density causes them to be non-applicable for electron microscopy amyloid characterization. It is of great importance as the idea of the development of a cost-effective method for simultaneous cross-platform imaging (for light- and electron microscopy) constitutes one of the driving factors for studies performed in the frames of this thesis. I believe that the design of a functional probe for amyloid imaging characterized by emission spectra in the NIR (near infra-red) range and with the ability to penetrate the blood-brain barrier (*i.e.* possessing small molecular weights, sizes and control over polarity) and high electron density (for TEM imaging) is of great significance.

2 Multimodality

Numerous imaging techniques are an essential part of the development of clinical treatment methods. Due to light, electrons and even sound-waves interactions with matter, peculiar images can be generated. Thus, structural, metabolic, and functional information on distinctive tissue abnormalities can be resolved. Bio-imaging is an invaluable tool for a better understanding of the mechanisms behind a variety of life-threatening diseases.

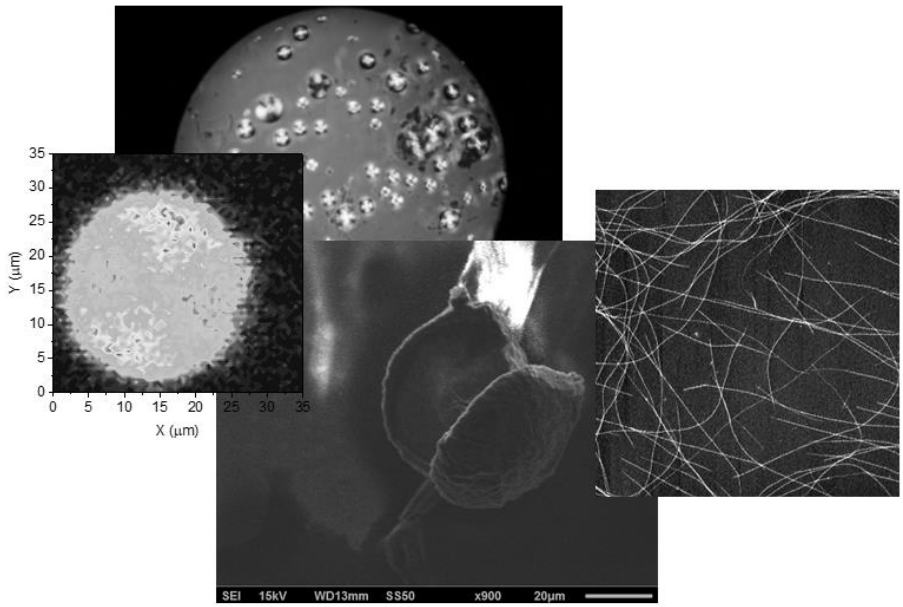

This sub-chapter will introduce the reader to the idea of multimodal imaging, where distinctive techniques of image generation are correlatively used.

2.1. Imaging modality

Distinctive abnormalities resulting from complex bio-physical processes, as a manifestation or an early sign of life-threatening disease, may affect all regions of the human body[62]. Such abnormalities may form from and build up in the four primary types of tissues, *i.e.* nervous, muscle, epithelial and connective tissues (see fig. no. 10). Therefore, advanced methods of detection and structural description of abnormalities within distinctive and complex biological environments are of great importance.

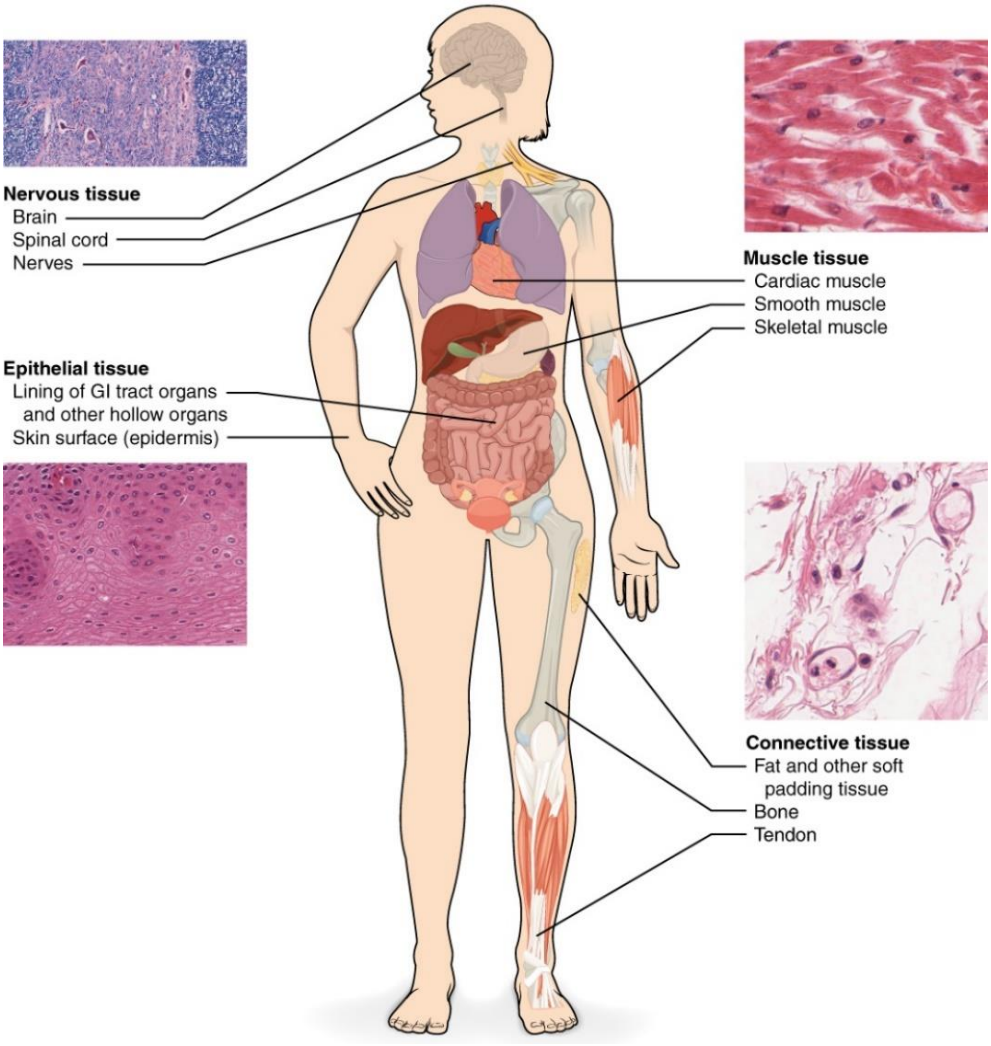

Figure 10. The four primary tissues type in human body. Reprinted from ref. no. [63] under Attribution-ShareAlike 4.0 International (CC BY-SA 4.0). Micrographs provided by the Regents of University of Michigan Medical School © 2012 (*https://histology.medicine.umich.edu*), under Attribution-NonCommercial-ShareAlike 4.0 International (CC BY-NC-SA 4.0).

However, due to the structural variety of abnormalities as well as their distinctive areas/depths of occurrence, it is challenging to characterize them with a single imaging method. Therefore, numerous imaging modalities, categorized by the mechanisms by which images are generated, are utilized in modern bio- and medical imaging[64]. Exemplary modalities and their basic descriptions are presented in the table no. 2.

Table 2. Exemplary modalities and their brief description. Data derived from ref. no.[64-67].

Modality	OI	EM: TEM & SEM	MRI	PET
Image generation mechanism	Interactions with light (e.g. fluorescence)	Interactions with electrons: scattering	Emission of radio frequency signal after nuclear spin excitation	Photon emission resulting from positron annihilation
Average tissue penetration	1 – 10 mm	< 1 µm	> 500 mm	> 500 mm
Average spatial resolution	Typically 1 mm, up to ~150 nm (for advanced techniques, e.g. confocal imaging)	~ Å	~ 100 µm	1 – 2 mm
Average temporal resolution	From seconds to minutes	From seconds to minutes	5 – 30 min	10 – 90 min
Advantages	Non-ionizing, cost-effective, customizable, super-resolution available (*e.g.* PALM), suitable for spectroscopic measurements	Revealing ultrastructural information, sub-atomic resolution	Non-ionizing, good contrast for soft tissues, reveals biochemical information (spectroscopic)	High sensitivity, qualitative data, dynamic
Limitations	Limited tissue penetration depth and spatial resolution, usually based on fluorescent staining agents	Not suited for live imaging (ionizing), limited sensitivity for light atoms (e.g. hydrogen)	Expansive setups and maintenance, not suitable for bone imaging, marker dependent	Requires positron-emitting radioisotope imaging agents, costly
Applications	Cancer imaging, cell trafficking, gene expression, *in vivo* imaging	Ex vivo imaging, structural analysis with a subatomic resolution	Excellent for *in vivo* spectroscopy of soft tissues	Diagnostic imaging in e.g. oncology, and cardiology

OI – optical imaging, EM – electron microscopy (T/S – transmission/scanning), MRI – magnetic resonance imaging, PET – positron emission tomography, PALM – Photo-activated localization microscopy.

It is extremely important to understand that a distinct imaging modality has its trade-offs, and cannot be universally applied. A distinct form of energy (on which a specific imaging modality is based) interacts with matter differently and according to specific laws of physics. Therefore, for every bio-imaging technique, distinct and inherent limitations can be identified, usually based on: temporal resolution (defined as the amount of time necessary to acquire a sufficient amount of data to generate an image), spatial resolution (defined as the possibility of differentiation between the two points), depths of tissue penetration, sample preparation requirements, and potential damaging (lack of bio-compatibility).

Exemplary, the spatial resolution of a microscope can be calculated according to the Abbe diffraction limit (equation 1)[66, 68]:

$$d = \frac{\lambda}{2nsin\theta} = \frac{\lambda}{2NA} \quad (1)$$

Where:

n : medium refractive index
λ : wavelength
θ : half of the maximum angle at which light can be collected by the objective
NA : objective numerical aperture (usually in the 0.2 – 1.4 range)

Therefore, the spatial resolution of an optical microscope operating on blue light (400 nm) is diffraction-limited and equal approximately to 0.25 µm. Hence, objects smaller than the aforementioned dimension cannot be distinguishably depicted by the considered microscopic system. Additionally, blue light is highly absorbed and scattered by the tissues (due to the presence and optical properties of water, melanin, hemoglobin and cytochrome), which also limits the imaging penetration depths[69]. Great scientific and engineering endeavors have been made over the last decade, and the diffraction limit of optical microscopy has been already surpassed. New techniques, described under the super-resolution optical microscopy term, have emerged, e.g. photo-activated localization microscopy (PALM)[65]. However, it is worth noting that these technologies are staining agent dependent, costly, and rely on advanced microscopy setups of ambiguous commercial availability.

2.2. Multimodal imaging

A perfect imaging setup should provide complex information on the sample: structural and functional. The phrase “functional” refers to the physiological, metabolic, or biological characteristics of the sample (e.g. diffusion, perfusion, chemical activity, or surface hydrophobicity). However, the implementation of a single modality cannot fully decipher the inner working of the entire organism, as specific limitations are inherent in a given technology. For example, electron imaging (especially TEM) is an invaluable technique for structural biology[67], as its excellent resolution (up to single atoms) allowed to resolve most of the organelles of a eukaryotic cell[70], as well as the structural features of the human nervous system – composed of separate cells communicating *via* neurotransmitters[71]. However, the main and

simultaneously inherit electron imaging disadvantages are operation in high vacuum and strong X-ray radiation. Therefore, *in vivo* imaging of delicate and soft matter is limited. Moreover, hydrated samples cannot be effortlessly studied with this technique. Overall, electron imaging requires specific sample preparation methodology, based on dehydration and fixation. Therefore, simultaneous or subsequent use of distinct modalities may be beneficial and allow for elucidation of processes leading to abnormalities formation. Such an approach, from now on, will be referred to as "multimodal imaging". Among commercially available multimodal systems, positron emission tomography (PET) correlated with computed tomography (CT) – X-rays attenuation-based technique - are the most prominent for biomedical applications[64, 72]. However, in biological research, especially in structural biology[73], correlative light and electron imaging (CLEM) is of great importance.

2.3. Nanotechnology: multimodal markers

Nanotechnology allows to reveal and utilize unique chemical and physical properties of various materials in the nanoscale (1 – 100 nm). The diversity of nanostructures has already found various biomedical applications, including bio-imaging performed with almost every available modality. For example CdSe quantum dots (OI), Gd_2O_3 paramagnetic nanoparticles (MRI), and gold nanoparticles (TEM)[74]. Nanostructures can be precisely modified and functionalized with numerous chemicals[75], which expands their utility. Interestingly, nanoparticles based on noble metals, in comparison to organic dyes (with low electron density) are excellent candidates for TEM contrasting agents[76-77]. Therefore, nanostructures are an ideal candidate for the design of a multimodal and simultaneously functional imaging markers. Based on the recent data (see figure no. 11) it can be forecasted that the structural design of nanomaterials for imaging will further expand and diversify[78].

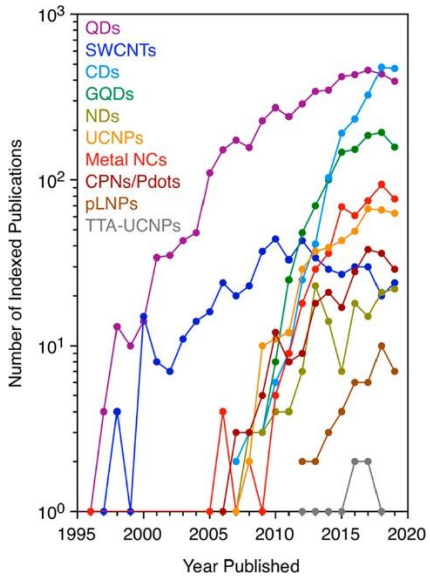

Figure 11. Approximate numbers of indexed publications on luminescent nanoparticles, per year. QDs - semiconductor quantum dots; SWCNTs - single-walled carbon nanotubes; CDs - carbon dots; GQDs - graphene quantum dots; NDs - nanodiamonds; UCNPs - lanthanide-doped up-conversion nanoparticles; metal NCs - metal nanoclusters; CPNs/Pdots - conjugated polymer NPs/semiconducting polymer dots; pLNPs -persistent-luminescence nanoparticles; TTA-UCNPs - triplet-triplet annihilation up-conversion nanoparticles. Reprinted from ref.[78] (*https://doi.org/10.1021/acs.chemrev.0c01176*), Copyright © 2021 American Chemical Society.

The idea of a synergistic fuse of chosen imaging modalities with the functionality of nanoparticles constitutes the inspiration for my work. I believe that complementary information provided by subsequent optical and electron imaging (multimodality) will contribute to a better understanding of the complex proteinous structures – amyloids - being associated with neurodegenerative diseases (e.g. Alzheimer's disease).

3 Gold nanoclusters

Large molecules (such as DNA or proteins) were extensively studied and manipulated on the single-atom scale over the past decade. Similarly, a modern chemist can precisely introduce a specific functional group into the molecules' architecture. However, at the nanoscale, the synthesis of two identical nanoparticles remains challenging. In terms of nano-chemistry, colloidal and plasmonic gold nanoparticles were intensely investigated due to their remarkable functionalities being unavailable for other groups of nanomaterials. However, from the early 2000s a new group of nano-structures, *i.e.* atomically precise nanoclusters, tends to attract ever-growing attention constituting a so-called bridge between bulk material and single molecules.

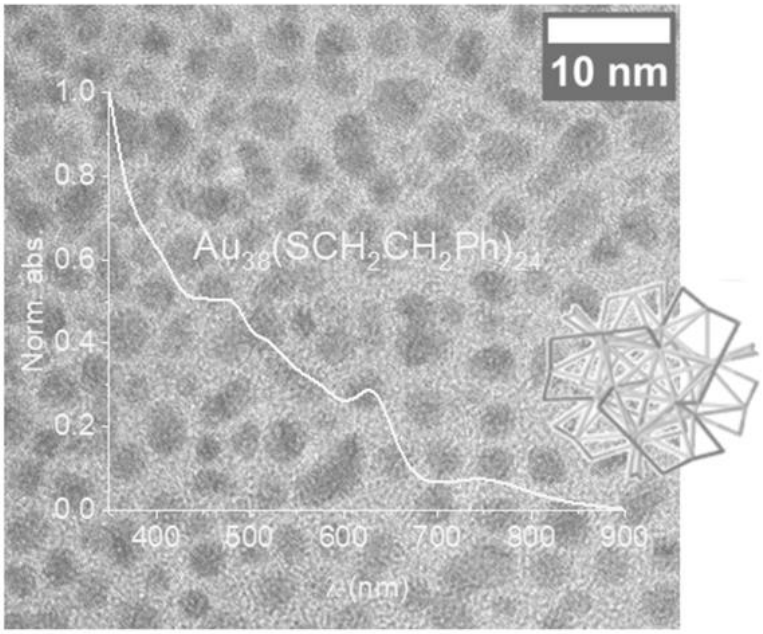

This sub-chapter will introduce the reader to the topic of atomically-precise nanoclusters (based on gold), including their definition, physicochemical properties, applications in bio-imaging, state of art research summary, challenges, and perspectives.

3.1. Gold nanoclusters definition

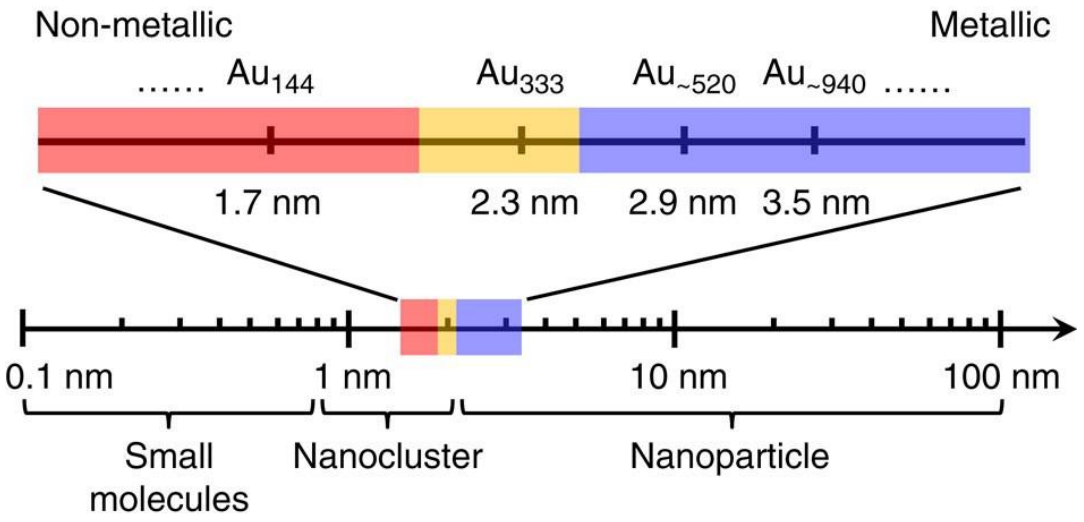

Figure 12. From non-metallic to a metallic state of gold nanoparticles. Size (gold atoms number) dependent evolution of gold nanoparticles metallicity: from molecule-like to plasmonic structures. Reprinted from reference no.[79] (https://doi.org/10.1038/ncomms13240) under Creative Commons Attribution 4.0 International license.

Atomically precise gold nanoclusters (APNCs) can be defined as nanomaterials with dimensions comparable to the Fermi wavelength of electrons in gold (< 2 nm) where metallic character, *i.e.* collective excitation behavior, is no longer maintained (see figure no. 12)[79]. Therefore, free electron gas density does not oscillate coherently upon interaction with the electromagnetic field, *ergo* plasmonic bands are no longer observed. Instead, discrete electron energy levels and HOMO-LUMO gap emerge, which leads to molecule-like behavior of APNCs: single electron transitions and excitons are possible[80]. Due to the well-defined and precisely controlled chemical composition on the atomic scale and to the quantum confinement effects, APCNs present noteworthy properties including enhanced physicochemical stability, tailored quantum yield and lifetimes, large Stokes shifts, and discrete energy levels manifesting as multiple absorption bands in the UV-Vis range wavelengths[81-82]. These properties will be comprehensively discussed in the subsequent subsection of this chapter. Moreover, in contrast to organic dyes, due to the high electron density of gold, APNCs are also excellent TEM imaging agents[77]. When used as **multimodal probes,** they can allow for a better understanding of nano-bio interfaces. Alongside light microscopy, they may contribute to the successful translation of nano-bio imaging into clinical trials[83], which is of great importance and inspired me to conduct my research.

To follow up on the current understanding of APNCs structures, it is significant to dive briefly into their history. In 1997 Whetten and Murray groups started exploring gold nanoclusters chemistry and studies on ligand-stabilized atomically-precise nanoclusters have been rapidly developing[80, 84-85]. In the pioneering work of Tsukuda and co-workers,

glutathione-stabilized clusters with defined numbers of atoms and distinct optical properties were obtained and separated with gel electrophoresis[86]. In the following years, the field rapidly developed and numerous synthetic protocols were published[80, 87-88]. Combined experimental and theoretical (based on DFT calculations and X-ray crystallography) studies led to the "divide and protect" concept explaining the thermodynamic stability differences between nanocluster species (distinguished by number of gold atoms) and revealing the profound role of cluster-protecting ligands in the determination of nanoclusters atomic structure, metal-ligand interface and physicochemical properties[89-91]. Studies concluded that thiolate-protected nanoclusters, investigated in the frames of this thesis, are made of core Au atoms (in the reduced state) that are surrounded by "staple-like motifs" (in a form of -S-Au-S-Au-(..) units) that are further surrounded by organic ligands (see fig. no. 13). What is more, the "*auro*philic" interactions (Au ⋯ Au), analogous to hydrogen bonding, have been identified to be crucial for the nano-chemistry of gold compounds, including APNCs[92]. For clarity, "*auro*philic" bond lengths and energy are well established and are equal to 2.85 – 3.50 Å and 5 – 15 kcal mol^{-1}, respectively[93]. The general chemical formula for thiolate-protected APNCs might be written down as: $(Au_n(SR)_m)^q$, where: n – number of gold atoms (*e.g.* 18, 25, 38), SR - protecting thiol with an organic group "R" (*e.g.* 14, 18, 24, respectively), q – cluster charge.

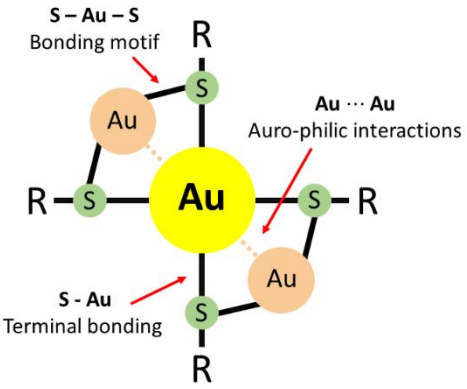

Figure 13. Schematic representation of gold nanoclusters' architecture: $Au_n(SR)_m$. The gold nanocluster core is presented as a yellow circle. Corresponding and simplified structural motifs, contributing to the cluster stability, are marked with red arrows (Au – gold, S – sulfur, R - an organic group). Scheme prepared based on a common architecture of atomically-precise gold nanoclusters reported in literature[94].

3.2. Gold atom number – towards atomic precision: structure versus optical properties

Rapidly developing synthetic routes (*i.e.* pH, solvent or temperature directed size focusing[95]) and separation techniques (based on high-performance liquid chromatography (HPLC), polyacrylamide gel electrophoresis (PAGE) or dialysis) described in the last years allowed to obtain atomically-precise nanoclusters of various sizes, *ergo* optical properties[96-98].

Monodispersity of clusters was a milestone for their physicochemical characterization, including a comprehensive understanding of their size to optical properties correlation. The energy levels of atomically-precise nanoclusters are distinct for specific cluster sizes, non-plasmonic, and extremely sensitive to changes (even at a scale of a single gold atom)[94]. In other words, transitions observed in the UV-Vis spectrum may provide information about the composition and stability of the nanocluster, revealing potential cluster transformations (see figure no. 14)[87].

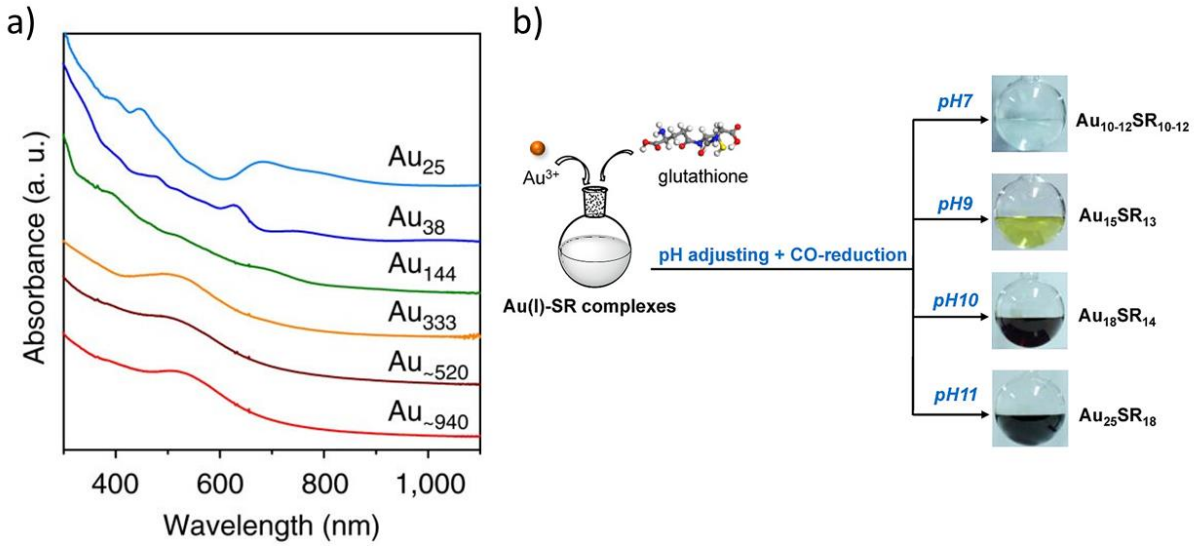

Figure 14. Evolution of gold nanoparticles UV-Vis spectra and an example of the size focusing synthesis. a) Steady-state absorption spectra of gold nanoparticles in dependence of gold atoms number: from plasmonic to molecule-like properties. Reprinted from reference no.[79] (https://doi.org/10.1038/ncomms13240) under Creative Commons Attribution 4.0 International licens. b) Schematic representation of size focusing synthesis based on pH adjustments. Reprinted with permission from reference no.[95] (https://doi.org/10.1021/cm304098x), Copyright © 2013 American Chemical Society.

Up to date, approximately 100 species of noble metal nanoclusters (including poly-metallic alloy clusters) have been reported in the literature, alongside their crystal structure[99]. $Au_{25}(SR)_{18}$ nanoclusters have been synthesized, for the first time, in 1998[84], and structurally resolved in 2008[100]. However, up to this day, $Au_{25}(SR)_{18}$ framework remains extensively studied and constitutes a perfect case study to introduce or contribute to the field of atomically-precise nanochemistry of noble metal molecule-like nano-structures. As understanding of optical properties of nanoclusters is of great importance for this thesis, I will guide the reader through the well-established knowledge regarding the $Au_{25}(SR)_{18}$ APNCs, where SR stands for PET: 1-phenyl ethanethiol (SCH_2CH_2Ph). For clarity, optical properties, despite the same structural framework of the cluster, may be differing due to the overall nanoparticle charge or a type of protecting ligands.

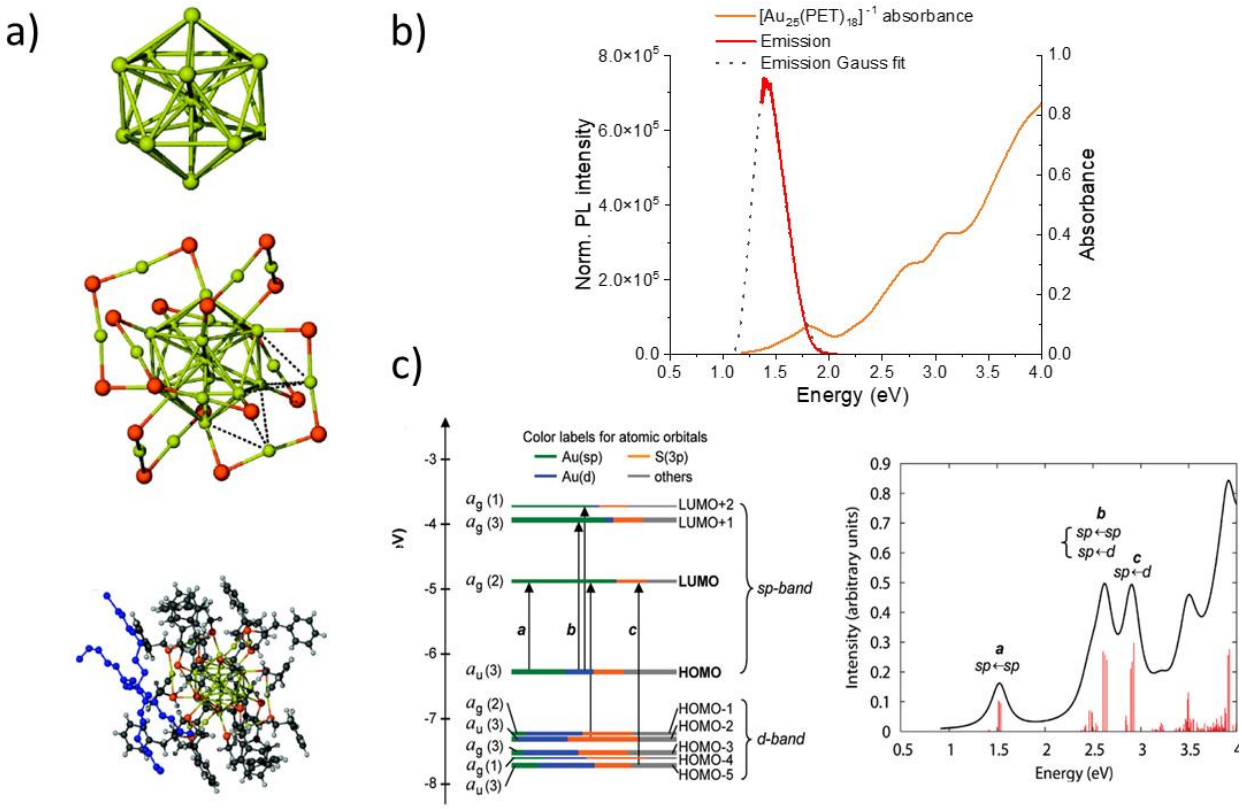

Figure 15. Structural and spectral analysis of $Au_{25}(SR)_{18}$, where SR – 1-phenyl ethanethiol, PET (SCH_2CH_2Ph). a) Au_{13} core: 12 gold atoms on the vertices of an icosahedron and one in the center, "staple-like" motif: $Au_2(SCH_2CH_2Ph)_3$, counter-ion ($N(C_8H_{17})_4^+$) TOA^+ (depicted in blue). Gold – yellow, sulfur – orange, carbon – gray, hydrogen - off-white. Reprinted from ref.[100] (https://doi.org/10.1021/ja800561b), Copyright © 2008 American Chemical Society. b) $Au_{25}(PET)_{18}^-[TOA]^+$ ground state absorption spectra and emission (as excited at 470 nm and divided by the corresponding absorbance at the excitation wavelength), own results. c) Kohn–Sham orbital energy level diagram for a model compound $Au_{25}(SH)_{18}^-$ alongside its theoretical absorption spectrum. Reprinted from ref.[90] (https://doi.org/10.1021/ja801173r), Copyright © 2008 American Chemical Society.

$[Au_{25}(PET)_{18}]^-[TOA]^+$ APNCs are composed of icosahedral Au_{13} core and six orthogonal semirings, *i.e.* staple-like motifs: ($-Au_2(SCH_2CH_2Ph)_3-$). The thiolate ligand is symmetrically distributed on the surface of the entire structure. However, the ethyl-phenyl groups are oriented in a way to accommodate the TOA^+ cation presence, which introduces a disorder in the ligand coverage[100] (see figure no. 15, a). Exemplary experimental absorption and emission spectra of the corresponding structure are presented in figure 15, b). Disclaimer: The 1.3 eV (~900 nm) limit of the present emission spectra is due to the employed detector limitations. Zhu *et al.*[90] have correlated the crystal structure of $Au_{25}(PET)_{18}$ with its ground state absorption spectrum due to time-dependent density functional theory (TDDFT) calculations, performed on a simplified $Au_{25}(SH)_{18}^-$ model. Their work gave a deeper insight into the optical properties of the Au_{25} clusters framework. Most importantly, Zhu *et al.* indicated that the HOMO and lowest LUMOs states are mostly composed of sp atomic orbitals of gold core with contributions from thiolate ligands (see Kohn-Sham molecular orbitals diagram, fig. 15, c). His results ties up the fluorescence of APNCs with core structure, as well as with surface ligand chemistry. In general, the photoluminescence (PL) of APNCs in NIR wavelengths, most likely, arises from the

excited electrons decaying from high energy states in the sp band to hybrid electronic states (composed of core surface gold atoms and thiolate ligands), which can be classified as a intraband process. However, for the emission in the visible range of the spectra: the strong Au(I)-S bonding is crucial. It results in hybrid electronic states that are resulting in an sp to d band transitions (interbad process). Therefore, the PL origin of APNCs can be attributed to the so-called ligand-to-metal charge transfer (LMCT) states[101]. It may explain the large Stokes shifts and long lifetimes (in order of hundreds of nanoseconds), typical for APNCs. However, a comprehensive understanding of the PL mechanisms of APNCs remains elusive, as multiple electronic transitions may be contributing[102].

3.3. Ligands importance and functionality

Multiple studies on ligand exchange were conducted with the assistance of UV-Vis spectroscopy, which is complementary to mass spectrometry and X-ray crystallography[103-104]. In atomically-precise nanochemistry, ligands are of great importance and may serve as a tool to tailor the structural frameworks of the nanoclusters. Exemplary ligand-guided synthesis of gold nanoclusters with distinctive core sizes[105] is presented in figure no. 16. In the aforementioned work, change of the position of $-CH_3$ group within methylbenzene thiol (MTB) molecule results in the formation of clusters with the specific core sizes (130, 104, and 40 core atoms, for para, meta- and ortho-MTB respectively). Authors of the aforementioned publication hypothesized that size-selectivity observed in their synthetic approach may arise from the distinct steric hindrances introduced by isomeric forms of MTB. The closer the $-CH_3$ group is, to the sulfur atoms (in the thiol - MTB), the more efficiently it can protect the gold-sulfur interfaces (by blocking it), thus smaller clusters are prone to form. Therefore, modification of the chemical composition of the ligands is a promising strategy to control gold nanoclusters structure with atomic precision.

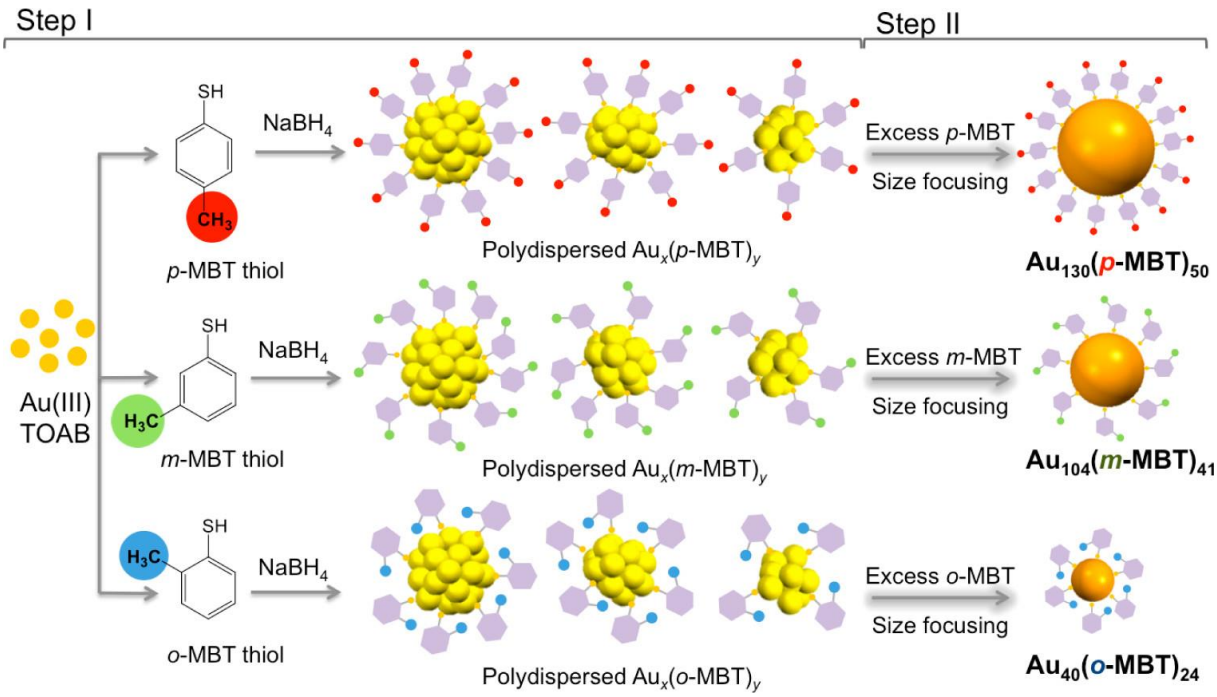

Figure 16. Schematic representation of a size-focusing synthesis controlled by ligand chemical structure. Steric effects introduced by the -CH3 group of the para-, meta- and orto-methylbenzenethiol force formation of nanoclusters with 130, 104, and 40 core atoms numbers, respectively. Reprinted from ref.[105] (*https://doi.org/10.1021/acs.nanolett.5b01122*), Copyright © 2015 American Chemical Society.

It should be emphasized that typical PL-QYs (the photoluminescence quantum yields) of APNCs are usually smaller than 1%, as efficient nonradiative relaxation pathways via surface versus ligand motions are possible[94, 101]. However, the optical properties of nanoclusters are already tailored, and varying ligand compositions regulates the intra-band transitions, which is beneficial for microscopic applications[88, 106]. Generally, it is possible to enhance the PL-QYs of APNCs, even by the order of magnitude. Among others, there are two main strategies based on ligands physiochemistry: 1) to suppress surface-ligand motions, and 2) to enhance charge transfer (LMCT) by introducing a strong electron-donating group.

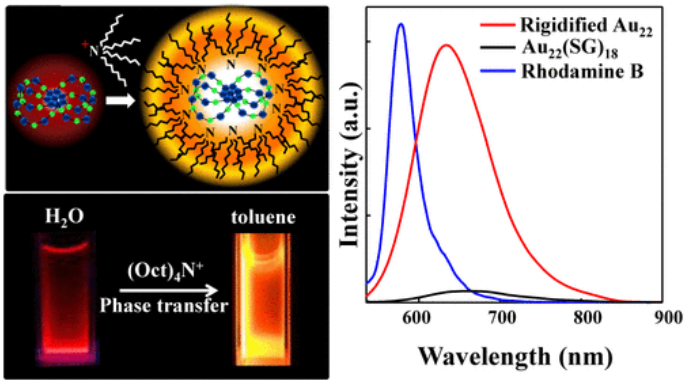

Figure 17. Gold nanoclusters ligands rigidification. Schematic representation of tetraoctyl ammonium (TOA) cation biding to $Au_{22}(SG)_{18}$ nanoclusters and luminescence spectra of aqueous solution of $Au_{22}(SG)_{18}$ clusters alongside its TOA-functionalised counterpart, in toluene. Reprinted from ref.[107] (https://doi.org/10.1021/jacs.5b04210), Copyright © 2015 American Chemical Society.

As presented in figure no. 17, the introduction of tetraoctylamonium (TOA) cation to $Au_{22}(SG)_{18}$ (where SG – glutathione), and its subsequent transfer to the organic phase, resulted in PL-QYs greater than 60%, at room temperature. Analogous enhancement was observed with time-resolved and temperature-dependent measurements, performed below freezing, for TOA-free APNCs. Therefore, ligand shell rigidity highly modulates APNCs' photoluminescence QYs by diminishing the thermal relaxation[107]**.** To discuss the subject of the 2nd strategy of APNCs QY enhancement, I would like to emphasize the $SC_{12}H_{25}$, SC_2H_4Ph, and SC_6H_{13} ligands. In terms of the length of the alkyl chains, the dodecyl group ($C_{12}H_{25}$-) is longer, in comparison to the hexyl group (C_6H_{13}-). The alkyl chain length influences the capability of electron density pushing towards the terminal sulfur atom ($S^{\delta-}$). What is more, the phenyl group additionally enhances the electron-donating capabilities of the molecular system. Therefore, overall charge donating efficiency (to the sulfur atom) lines up the aforementioned ligands in the following order: $SC_2H_4Ph > SC_{12}H_{25} > SC_6H_{13}$. Wu and Jin[108] showed that despite the same clusters core size, QYs of $Au_{25}(SR)_{18})^-$ are ligand-dependent and equal to $\sim 1 \times 10^{-4}$, 5×10^{-5}, and 2×10^{-5}, for $Au_{25}(C_2H_4Ph)_{18}]^-$, $[Au_{25}(C_{12}H_{25})_{18}]^-$, and $[Au_{25}(C_6H_{13})_{18}]^-$, respectively. They concluded that APNCs emission may be enhanced *via* the direct donation of the delocalized electrons from the ligands' electron-rich groups (to the clusters' core) or by utilizing the ligand architectures where electronic distribution is favoring the formation of $S^{\delta-}$. Thus, ligands play a crucial role in the optical properties of APNCs and their chemical composition may be designed to enhance charge transfer to the Au-S bond.

For bio-imaging, nanoparticle surface ligands are also of great importance in terms of binding affinity to various biological structures and their potential selectivity [109-110]. Recent studies indicated that, besides the simple steric anchoring and electrostatic interactions, nanoparticles ligand hydrophobicity and conformation highly influence labeling efficiency[77]. It is an analogous phenomenon to the organic dye polarity problem[111]. As an example, the interaction of double-ligand coated nanoparticles and Aβ(1-42) have been elucidated by atomistic molecular dynamics simulations by Tavanti *et al.*[112]. Their nanoparticle model was

characterized by 2 nm core size and double coating, i.e. 70% MUS (hydrophilic 11-mercapto-1-undecane-sulfonate) : 30% OT (hydrophobic 1-octane thiol). However, a control sample, *i.e.* 0% MUS : OT 100% has been also simulated. They showed that the nanoparticle binding happens on the external Aβ(1-42) protofibril parts, being composed mostly of hydrophobic amino acids. Tavanti *et al.* also emphasized the number of nanoparticles to Aβ(1-42) fibril surface contacts being dependent on the mutual correlation of exposed hydrophobic amino acids and nanoparticles hydrophobic ligands. However, hydrophilic ligands are also required, to maintain solubility in water. Hence, ligand chemistry is a powerful tool to modulate the binding affinity of gold nanoclusters to complex biological surfaces. Factors such as ligands' charge, conformation, and hydrophobicity should be included in the successful design of APNCs for bio-imaging.

3.4. Nanoclusters in bio-imaging

Herein, state-of-the-art imaging utilizing clusters is discussed, to give an insight into their functionality and challenges imposed by the field.. Gold nanoclusters were already applied in state-of-the-art *in vivo* and *in vitro* bioimaging[113-115]. What is beneficial for light microscopy of tissues, it was proven that upon excitation, numerous of APNCs are photoluminescent in a range of Vis and NIR wavelengths[116]. Moreover, reports regarding cell viability revealed good biocompatibility of nanoclusters used for live HeLa cells investigation under confocal microscopy with two-photon excitation[117]. The functionality of gold nanoclusters in studies on the structure of biological materials was presented by Martikainen *et al.*[118]. In their work, hydrophobic pockets of selected enteroviruses (EV1) were targeted by conjugates of gold nanoclusters and selective-binding target agent (so-called “WIN compound”), and TEM-visualized. In detail, Martikainen *et al.* probes were chemically prepared to be selective for the hydrophobic pocket of specific enterovirus capsid protein - VP1 protein. Their probe was composed of (pMBA) capped gold nanocluster (Au_{102}-*p*MBA_{44}) further functionalized with a Pleconarli framework. However, Au_{102} cluster framework is found to be non-fluorescent[119] (as well as any other big clusters, see fig 1), thus for a multimodal (simultaneously suited for the light- and electron- microscopy) imaging, they performed additional functionalization of nanoclusters with a fluorescent dye.

Proteinaceous structures are highly heterogenous if their surface hydrophobicity or electronegativity is reconsidered. Proteins are usually flexible and multiple conformational states are possible, which, for a better understanding of their functions, should be cost-efficiently and easily visualized. Work on that Au_{144} APNCs attached to a protein complex performed by Jagota *et al.*[34] is an outstanding example of nanoclusters' utility in bio-imaging. They resolved 3D coordinates of the protein structure stained with nanoclusters by advanced computational analysis of cryo-TEM tilt-pair images. Simple tracking of APNCs bound to protein surfaces resulted in the evaluation of the structure and molecular motion of a specific protein. Moreover, investigations on amyloids, with ultra-small gold nanoparticles applied as markers, can be found also in the work of Cendrowska and co-workers[77]. They applied charged and zwitterionic gold nanoparticles to detect and characterize amyloid polymorphism in *ex*

vivo and *in vitro* samples. Their work confirms the hypothesis that amyloid formation *in vitro* may vary from those occurring *in vivo* and is of great importance for studies on amyloid formation. Additionally, they hypothesized that staining efficiency being of great importance for any microscopy technique is governed by hydrophilic and hydrophobic interactions between bio-interface and nanoparticles. However, they did not exploit the problem of nanoparticle to nanoclusters transition at all, despite the operative diameters of their probes being equal to 2 nm. Therefore, the overall picture allows to hypothesize that gold nanoclusters are an excellent candidate for the multimodal imaging, that is not possible with simple organic dyes. It is, however, challenging to design nano-structures big enough to be valid for a cost-effective TEM imaging and being simultaneously bio-compatible, water-soluble, with hydrophobic contacts and bright NIR-fluorescent. Additionally, advanced chemical processing is usually coined to selective binding to solely specific proteins, thus it is a limiting factor for the development of more versatile structures. It would be beneficial to prepare probes with some tunability or control over its hydrophobicity.

4 Multiphoton microscopy

Maria Göppert-Mayer published her work on the theory of two-photon transitions of atoms back in the 1930s and provided a solid theoretical foundation for the development of nonlinear optics. Her description of "*two light quanta*" excitation and subsequent emission (as well as Stokes, and anti-Stokes Raman effects) had a significant impact. Nowadays, in the 2020s, we still rely on her equations which opened up the roads to the rapid evolution of multiple fields of science. Herein, I will emphasize on one of them, namely the advanced multiphoton microscopy of biological samples.

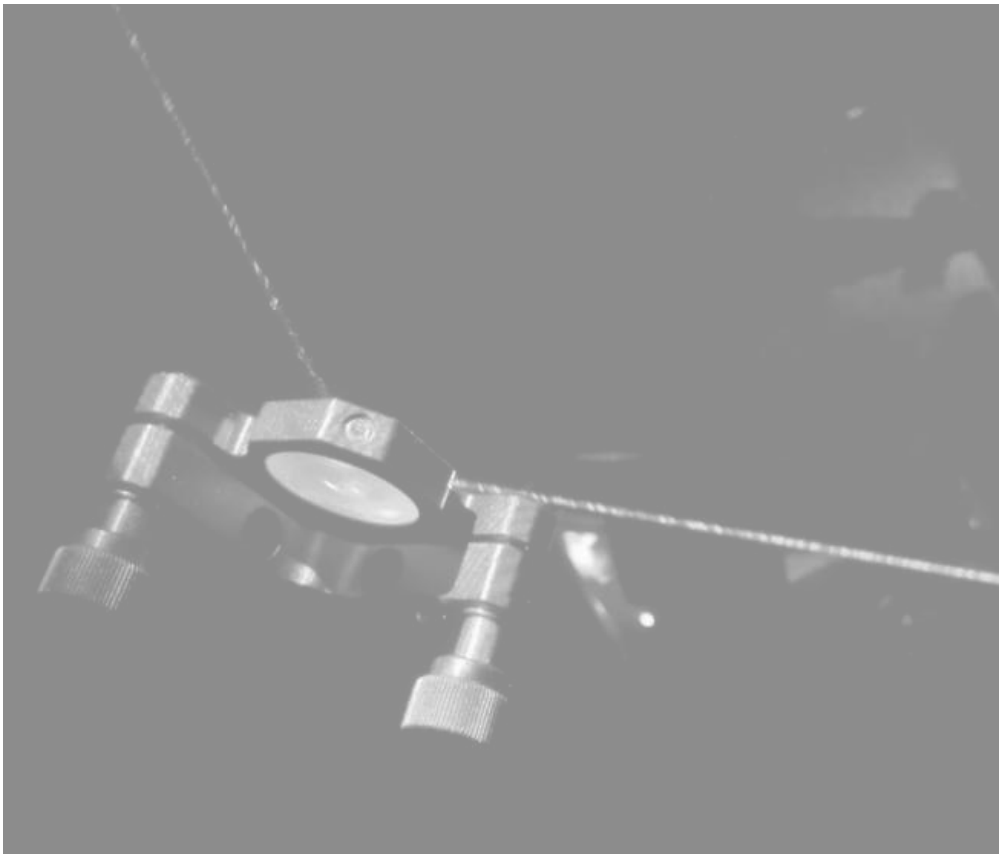

This subchapter will introduce the reader to the topic of polarization-sensitive multi-photon microscopy, including basic concepts in nonlinear optics, multiphoton properties of atomically-precise nanoclusters, and state-of-the-art in amyloid bio-imaging.

4.1. Two-photon fluorescence microscopy: principles and advantages

For efficient imaging of biological samples, there are three specific spectral ranges where the level of absorption and scattering of biocomponents is minimalized, for both, plant and animal tissues[120]. These regions are termed as the optical window I, II, and III (*i.e.* NIR-1 (700 - 1000 nm), NIR-II (1000 – 1350 nm), and NIR-III (1550 - 1755 nm)[121]. These wavelength ranges are defined in such a way due to minimal absorption of oxygenated hemoglobin, melanin, and water, see fig. no. 18. Therefore, **two-photon microscopy (2PM)**, usually operating in the aforementioned NIR-1 region, is a method of choice in bioimaging. It simultaneously provides high axial resolution (fluorophores outside the focal plane are not excited), lower scattering, lower phototoxicity of imaging, and deeper optical penetration in comparison to one-photon fluorescence microscopy techniques[120, 122].

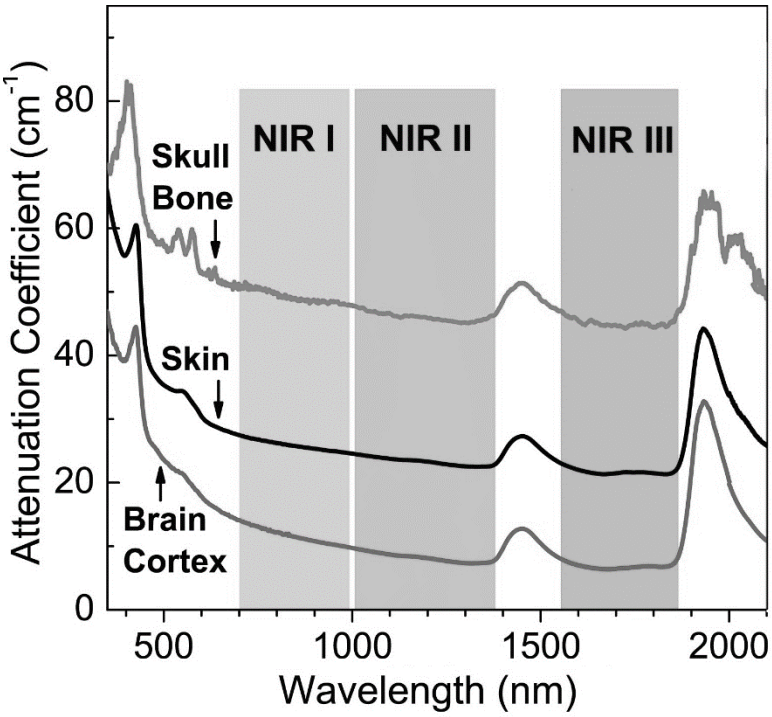

Figure 18. Three optical windows (NIR-I, NIR-II, NIR-III) for bio-imaging. Presented on the example of the head tissues (brain cortex, skull bone and skin) attenuation coefficient wavelength dependence. Adapted from reference no.[123] (https://doi.org/10.1002/jbio.201800141), © 2018 WILEY-VCH Verlag GmbH & Co. KGaA, Weinheim.

Herein, I will discuss the theoretical principles and advantages of 2PM. Then, based on recent literature, I will outline the connections between atomically-precise nanoclusters, multi-photon excited emission, and amyloids. A brief introduction into basics and history of nonlinear optics (NLO) for bio-imaging will be also presented.

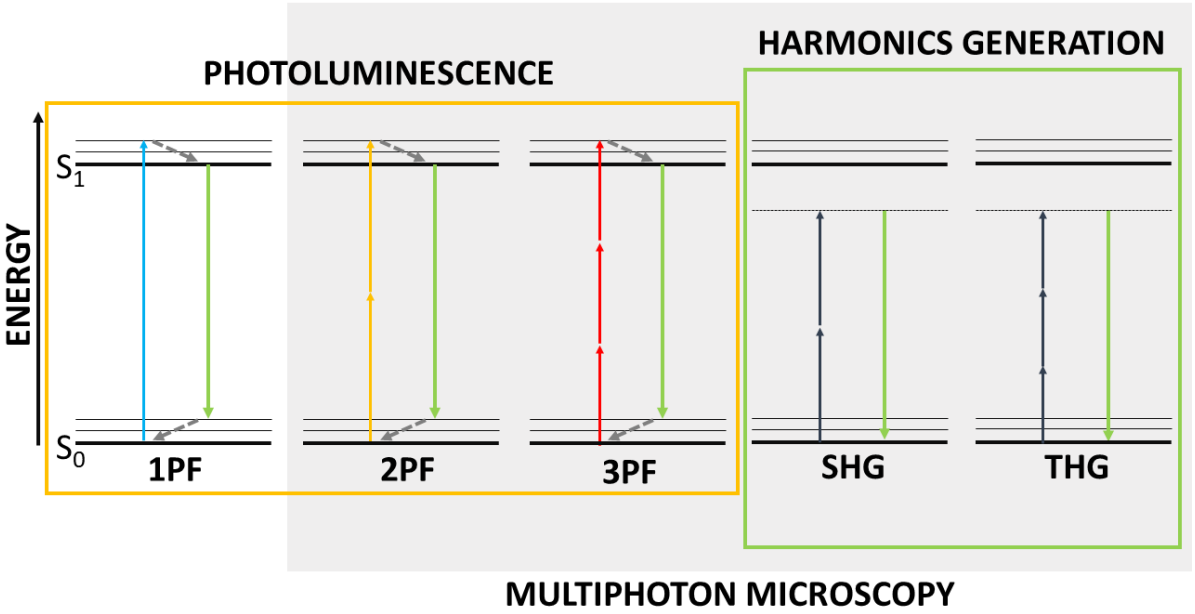

Figure 19. Simplified Jablonski diagrams of one- (1PF), two- (2PF), and three-photon (3PF) photoluminescence (*i.e.* fluorescence), and second and third harmonic generation (SHG, THG, respectively). Excited and ground singlet states are denoted with S_1 and S_0, respectively. Excitation (absorption) – blue, yellow, red, grey; emissive relaxation – green arrows; nonradiative relaxation - grey dashed arrows.

The phenomenon of the photon emission with a quadratic or higher-order dependence on excitation power is assigned to so-called "nonlinear optical properties", for example: multiphoton absorption and fluorescence/phosphorescence; second, third, and higher harmonics generation (SHG, THG and higher); optical Kerr effect; sum and difference frequency generation process. The nonlinear optical phenomena being of great importance for nonlinear microscopy, have been schematically presented in the Jablonski diagram (see fig. no. 19), namely 2PF, 3PF, SHG and THG.

Light (electromagnetic field, but here we will focus on its electric field component, "E") and matter interactions can induce a macroscopic polarization "P" of a matter, according to the equation (2)[120, 124]:

$$P = P_p + \varepsilon_0(\chi^{(1)}E + \chi^{(2)}E^2 + \chi^{(3)}E^3 + (\dots)) \quad (2)$$

Where:

P_p : macroscopic permanent polarization
ε_0 : vacuum permittivity
$\chi^{(n)}$: medium susceptibility (tensor)

The complex refractive index of the material is described by the first order susceptibility $\chi^{(1)}$. It describes the response of the matter upon illumination with low-intensity light. However, if a high-intensity electromagnetic field is applied, the nonlinear tensors $\chi^{(2)}$ and $\chi^{(3)}$ (n^{th}-order

susceptibilities, where n: 2, 3) cannot be neglected. They govern the second- and third-order nonlinear optical properties of a material, respectively. In frames of the scientific endeavors described within this thesis, two-photon absorption - 2PA – (as well as subsequent luminescence) of amyloids will be explored. Therefore, it will be described in more detail, in contrast to the remaining NLO phenomena. Nevertheless, their importance in bio-imaging will be also addressed.

Two-photon absorption (2PA) relies on a quasi-simultaneous absorption of two photons at a sub-femtosecond scale. If the sum of energy of two photons is sufficient and matches the energy gap between the ground and excited states of the fluorophore, an electronic transition may occur. This phenomenon was theoretically predicted by Maria Göppert-Mayer in the 1930s[125]. Interestingly, an experimental work confirming her remarkable predictions was performed nearly 30 years later, when Kaiser *et al.*[126] studied CaF_2: Sm^{2+} crystals. However, the work on imaging of living cells based on two-photon excitation was published as late as 1990, by Denk *et al.*[127]. His work, introducing NLO for microscopy, provided an unprecedented capability for the three-dimensional and spatially resolved analysis of biological samples. This field is still developing, and numerous studies are focused on the technical aspects of 2PM, as well as on the NLO properties of fluorescent markers.

To characterize the third-order NLO properties of the fluorophore, the two-photon absorption coefficient ($\alpha^{(2)}$) and the nonlinear refractive index ($n^{(2)}$) should be introduced. These values are dependent on the intrinsic light intensity, related to the real (*Re*) and imaginary (*Im*) part of the third-order susceptibility ($\chi^{(3)}$), and for fully degenerate case can be derived from equations no. 3, and 4:

$$\alpha^{(2)} = \frac{3\pi}{\varepsilon_0 (n^{(1)})^2 c\lambda} Im[\chi^{(3)}] \quad (3)$$

$$n^{(2)} = \frac{3}{4n^{(1)}} Re[\chi^{(3)}] \quad (4)$$

Where:

c : speed of light
λ : wavelength
$n^{(1)}$: linear refractive index

However, the probability of 2PA process is more commonly expressed in terms of the two-photon absorption cross-section (σ_2) - expressed in Goeppert-Mayer units (GM). GM can be expressed in CGS metric system as cm^4s/photon. Importantly, the aforementioned merit is not dependent on the sample concentration (see equation no. 5):

$$\sigma_2 = \frac{\hbar\omega\alpha^{(2)}}{N} \quad (5)$$

Where:

$\hbar\omega$: energy of incident light
N : number density of molecules

To characterize the fluorophore, the ratio of photons absorbed to photons emitted through the fluorescence process is crucial, as non-emissive relaxation pathways are also possible. It is quantitatively defined by the fluorescence quantum yield (η). The number of photons emitted *via* two-photon excited fluorescence (N^{2PE}), by analogy to one-photon fluorescence, can be calculated according to equation no. 6:

$$N^{2PE} \propto N\ x\ K\ x\ [\eta \frac{1}{2} \sigma_2 I_\omega^2] \quad (6)$$

Where:

K: experimental factor (e.g. the sensitivity of detectors)
I_ω : incident photon flux (photon/cm^2/s)

For two-photon microscopy techniques, to classify and compare the probe's performance, two-photon action cross-section or multi-photon brightness ($\sigma_{2,eff}$) is often used (eq. no. 7):

$$\sigma_{2,eff} = \eta\sigma_2 \quad (7)$$

The polarization of incident light, the angles between the absorption and emission dipole moments of the fluorophore as well as the direction of the signal collection ($\overrightarrow{\mu_I}$) are determining the signal collection efficiency. The intensity of fluorescence is proportional to the square of the dipole moment of the electronic transition ($\overrightarrow{\mu_{em}}$), in detail, from excited (e) to the ground (g) state: (e) → (g). However, the two-photon absorption probability is proportional to $\overrightarrow{\mu_{abs}}$ to the fourth power (corresponding to (g) → (e) electronic transition). Thus, the collected two-photon emission intensity (I_{2PE}) is proportional to (eq. 8):

$$I_{2PE} \propto |\overrightarrow{\mu_{abs}} \times \overrightarrow{E_\omega}|^4 |\overrightarrow{\mu_{em}} \times \overrightarrow{\mu_I}|^2 \quad (8)$$

Where:

$\overrightarrow{E_\omega}$: vector describing the polarization of the incident electromagnetic field

Due to the cubic dependence of two-photon collected emission intensity on the excitation power, a spatial confinement at the focal point is stronger for a multi-photon excitation, in comparison to one-photon process. Therefore, it can be employed to enhance performance in microscopy. Moreover, polarization analysis of multi-photon excited emission can be utilized to discuss the orientation of emitting species, within the sample plane. It will be comprehensively described in the subsequent chapter, as polarization-sensitive two-photon microscopy is the method of choice, utilized in this thesis.

4.2. Multiphoton properties: nanoclusters

Two-photon absorbing molecules are usually based on intramolecular charge transfer, non-centrosymmetric dipolar molecular backbones, or π-conjugated systems[128]. Their architectures, despite being well understood, may inherently limit the development of new strategies for their performance enhancement. Usually, increasing the conjugation length is

associated with enhanced multi-photon performance of the dye[129]as average hole–electron distance upon excitation will be increased in such systems[130]. However, the organic dyes chains cannot be indefinitely elongated, as the coherence of electron wavefunction will split into local minima bounded to the specific region of the molecule. It naturally sets the boundaries for the optimization of multi-photon properties. Therefore, an alternative approach is beneficial to explore. Impactful and inspiring studies on third-order NLO response of nanoclusters were performed by Antoine group[131]. It should also be noted that APNCs (atomically-precise nanoclusters) are studied in terms of nonlinear optical properties, both theoretically and experimentally[132], and our group already contributed to the field[133-135]. Although a complete picture of the photo-physics behind multiphoton excitation of atomically precise gold nanoclusters (APNCs) remains elusive[134], they are promising candidates for applications in nonlinear imaging. It is of great importance to understand that APNCs' nonlinear optical properties, may be tuned by: core size alongside the overall structure (ligands). Similarly to the push and pull molecular systems, for APNCs, charge distribution is crucial. However, the electronic structure of gold nanoclusters can be tuned *via* the metal core size engineering as well as ligands modification[136], and it was found to govern the multiphoton response of these structures (see figure no. 20).

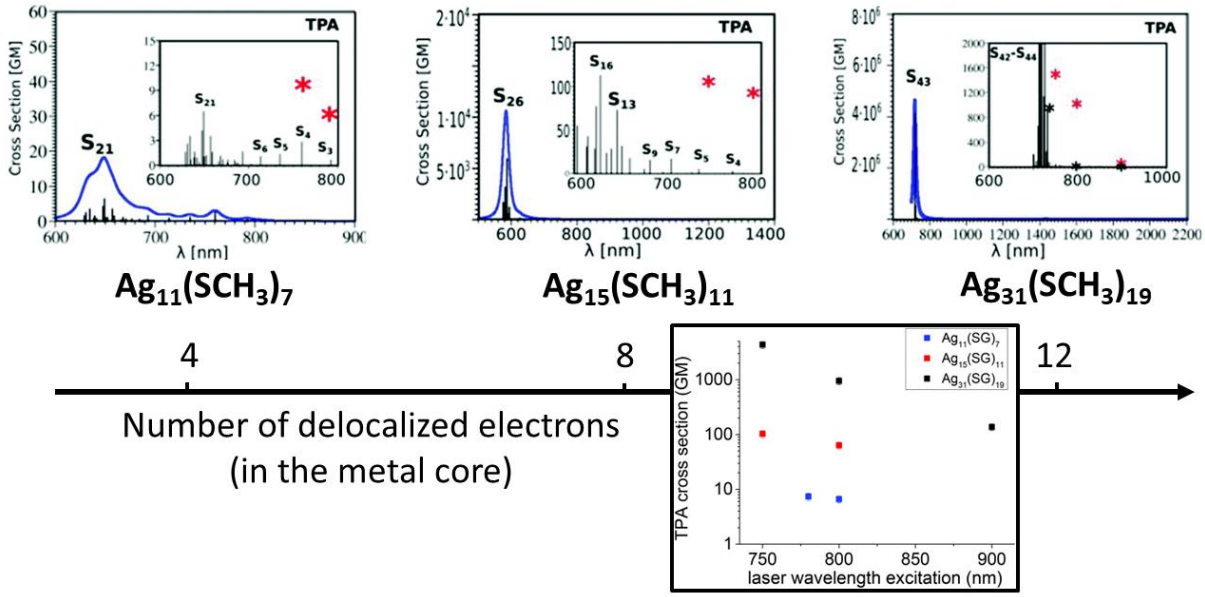

Figure 20. Modulation of two-photon absorption cross-sections of APNCs. Simulated two-photon absorption cross-sections were found to be strongly dependent on the number of delocalized electrons allocated to the metal core. Experimentally measured two-photon absorption cross sections (in GM) increase with the growth of APNCs' core size and are also wavelength dependent (framed inset). Prepared from figures no. 2 and 3, from ref.[136] (https://doi.org/10.1039/C6NR07989J), under Creative Commons Attribution 3.0 Unported (CC BY 3.0) license.

Their two-photon cross sections were reported to be orders of magnitude higher than those for the standard organic dyes (e.g. 2700 GM for Au_{25}, and 10^4 GM for Ag_{29})[132, 136-138]. Strict control over cluster chemical composition is a promising tool to develop new and smart

nanomaterials for applications in bio-imaging, as their electronic structure can be modified by ligands chemistry, doping, or by change of the core atoms number[139-140]. Moreover, ligand immobilization or introduction of bulky counterions may also increase two-photon excited fluorescence response form clusters (e.g. by 30-fold, as reported by Bertorelle *et al.*[131]). Therefore, ligands exchange as well as engineering are valuable strategies to induce significant third-order NLO effects in these systems.

Nevertheless, APNCs' nonlinear optical properties and their relation to clusters' structure are still scarcely described[101, 134]. Limited attention has been given to the cluster' protecting ligand influence on nonlinear optical processes. It is still an inspiring, timely, and prospective topic for numerous research groups, both in terms of theoretical and experimental approaches[132, 136, 141]. Most importantly, the chemical composition of APNCs (high electron density of gold, as well as functionality of ligands) fulfills all prerequisites for multimodal imaging, which, up to this day, is not widely exploited.

4.3. Multiphoton imaging of amyloids

The term "bioimaging" is a complex topic that includes numerous techniques and imposes specific challenges depending on the type of the investigated sample, for instance: animal or plant cells, intracellular components, viruses, or entire organisms[1, 142-143]. One particular and representative group of bio-materials that are of great importance to modern society and present challenges in bio-imaging are amyloids, which were defined and comprehensively described in the Chapter no. I (subchapters 1 – 1.7.) The advantages of 2PM were already successfully implemented in *in vivo* bio-imaging of Alzheimer's disease mouse models and also in the deep brain imaging reaching to the depths of several hundred micrometers[144-145]. However, both of the previously cited works relayed on fluorescent probes, e.g. commercially available CRAND-3 compound. Although it is selectively amyloid- binding, its relatively low excitation efficiency is limiting. The improvement of two-photon performances of NIR probes was outlined as crucial.

In recent years, numerous organic molecules were developed (mostly based on the derivatives of Thioflavin-T and Congo Red) to stain amyloid fibrils[59, 146]. Their functionality is usually based on molecular rotors, which upon binding to amyloids, are immobilized[147]. It results in the dye molecule becoming approximately 1000 times brighter, as non-emissive relaxations are limited. Additionally, the amyloid-specific biding is based on electrostatic, hydrophobic, and steric interactions. It is commonly achieved for planarized aromatic π molecular systems. What is more, to enhance the optical performance of the probe (*i.e.* quantum yield, fluorescence lifetime, Stokes shift), push and pull conjugated systems are widely exploited. Unfortunately, the architectures based on the conjugating bridge (C=C) easily isomerize and photobleach[148]. The LCOs (luminescent conjugated oligothiophenes), e.g. HS-169 or HS-84, are an exemplary group of such molecular probes, already utilized for *in vivo* multiphoton imaging[149].

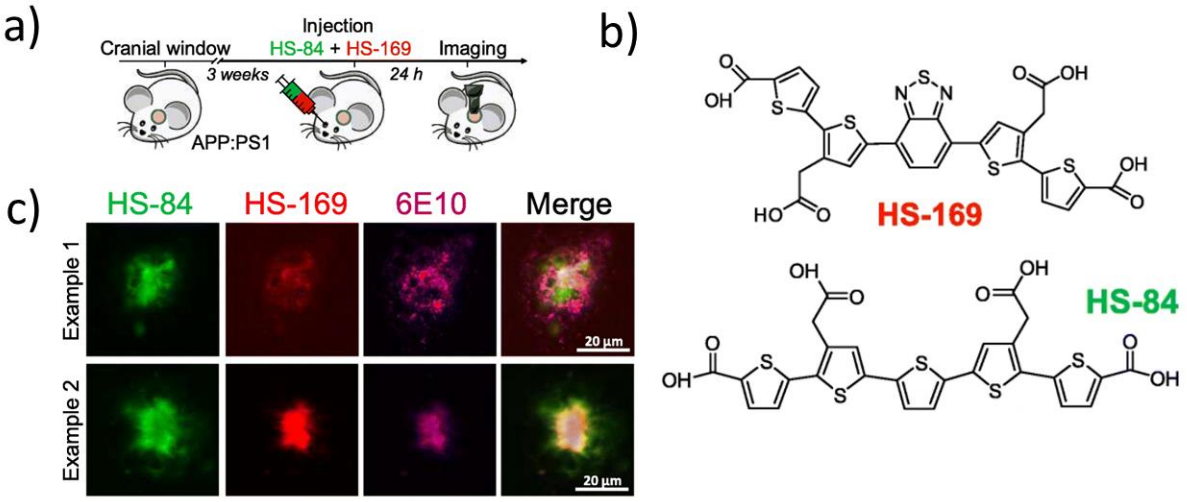

Figure 21. ***In vivo*** **multiphoton imaging of structurally heterogenic amyloid plaques**. a) Schematic representation of the experimental procedure, b) HS-84 and HS-169 molecular structures, c) exemplary amyloid plaques stained with luminescent conjugated oligothiophenes and 6E10 antibody and imaged under a two-photon microscope. Prepared from figure no. 5, from ref.[149] (https://doi.org/10.1186/s40478-019-0832-1), under Creative Commons Attribution 4.0 (CC BY 4.0) license.

The importance of molecular architectures design, for amyloid staining, can be visualized in HS-84 and HS-169 examples. The co-injection of these dyes allowed for the detection of amyloid-β plaques heterogeneity (see figure no. 21c), in the specific area of the living brain, *via* two-photon imaging.

The intrinsic optical properties of amyloids in the nonlinear regime have been already discussed in the literature. Hanczyc *et al.*[150] showed that insulin, lysozyme, and α-synuclein amyloids can be efficiently excited *via* two-, three- or higher multiphoton absorption, being dependent on the excitation wavelengths. Their corresponding two-photon absorption cross-sections were reported to be equal to 2600 GM, 1640 GM, and 5250 GM for 550, 570 and 550 nm excitation, respectively. The origin of peculiar two-photon absorption of amyloids have been attributed to the through-space dipolar coupling between excited states of densely packed and stabilized hydrogen bonding proteins, mostly from aromatic amino acids. Interestingly, multiphoton excited fluorescence as well as SHG from amyloids were utilized for label-free imaging of bovine insulin spherulites (see figure no. 22)[151].

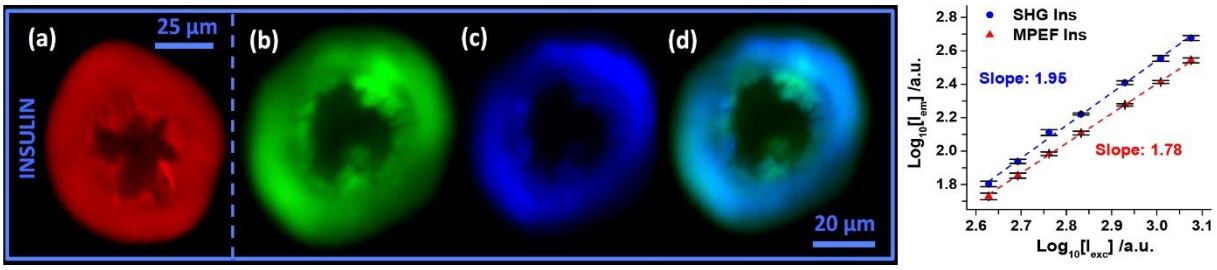

Figure 22. Label-free multiphoton imaging of amyloid spherulites. Bovine insulin spherulites imaged with: a) confocal fluorescence microscopy (excitation wavelength: 405 nm), b) multiphoton excited fluorescence (excitation wavelength: 910 nm), c) SHG (wavelengths: 910 nm). d) Nonlinear optical images overlay (b, c). The graph on the right side of the panel shows the power dependences for SHG and multiphoton excited fluorescence and its linear fit slopes. Reproduced from figure no. 3, from ref.[151] (https://doi.org/10.1364/BOE.8.000743), open access, © Johansson and Koelsch [2017] Optica Publishing Group.

Johansson and Koelsch pioneeringly obtained images of amyloid spherulites with two-photon microscope. They utilized SHG and multiphoton excited autofluorescence of amyloids to resolve and discuss the structural characteristic of spherulites. Images analyses of both, SHG as well as multiphoton excited autofluorescence, revealed the core-shell structure of spherulites, which corresponds well to previous work on this topic. The authors suggested that this phenomenon may be connected to highly organized amyloid fibrils in the shell structure (fluorescent) and amorphous proteins (non-luminescent) in the core region. They showed that imaging of these structures can be performed in a non-destructive and label-free manner, which is of great importance for potential *in vivo* applications.

Although the 2PM probes are extensively studied, their fluorescence in NIR wavelengths, photostability, good water solubility as well as efficient two-photon absorption properties (with two-photon absorption cross-sections in order of several hundred GM) is still challenging to achieve. There are numerous probes sensitive to the polarity of amyloids (or bio-interfaces in general) [146, 152]. However, their hydrophobicity cannot be modulated at will by the local environment and is directly bound to the probe's molecular architecture - functional groups. It should be noted, that up-to-date there is no NIR-emitting probe being simultaneously (1) an efficient two-photon absorber and (2) tunable in sensitivity for bio-interface polarity, and (3) multimodally applicable. Moreover, despite being useful for non-invasive, non-destructive, and label-free imaging, the autofluorescence of amyloids remains poorly described in the literature, especially under two-photon excitation. Additionally, its origin is still under debate and it has not been discussed at all in terms of amyloid polymorphism.

5 Crown ethers

Cations, anions, and even neutral molecules can selectively enter the cavities of compounds of extraordinary and fascinating architecture, called crown ethers. The discovery of these ring-like structures was awarded a Nobel prize for Chemistry in 1987 for Charles J. Pedersen, Donald J. Cram, and J-M. Lehn. Their work, where intermolecular forces play a primary role, founded a solid basis for new concepts in organic chemistry and the term "supramolecular chemistry" was born. Research on crown ethers (including the translation into gold nanochemistry) and their supramolecular properties, is fascinating and may lead to functional applications in bio-imaging.

This subchapter will introduce the reader to the topic of crown ethers, including the discussion on their structure and functionality. Their importance for gold nanochemistry will be also presented. Additionally, the current knowledge regarding crown ethers' interactions with amyloid aggregates will be depicted.

5.1. Crown ethers: structure and functionality

Crown ethers (CE) can be defined as cyclic oligomers of ethylene oxide, which classify them as aliphatic compounds[153]. They are composed of 4 to 10 -CH_2-CH_2O- groups, *i.e.* ethylene oxide units (see fig. no. 23). However, crown ethers with architectures based on endocyclic aromatic rings in their structure are also widely studied. Nevertheless, in the frame of this thesis, aliphatic crown ethers will be described. Conventionally, to name the aliphatic crown ether, the most often used nomenclature is: "x-crown-y", where: x – is the overall number of atoms in the macrocyclic cavity, and y – is the number of oxygen atoms. Therefore, "18-crown-6 ether" stands for a crown ether characterized by the cavity/ring composed of 18 atoms, while 6 of them are oxygen (synonyms: 1,4,7,10,13,16-hexaoxacyclooctadecane or ethylene oxide cyclic hexamer).

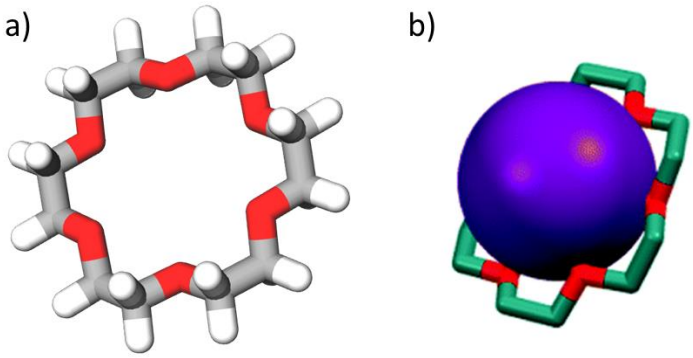

Figure 23. Representative crown ether structure and its supramolecular complex. a) Aliphatic crown ether (18-crown-6) stick model (red – oxygen, grey – carbon, white – hydrogen), b) the supramolecular complex: the potassium cation (violet ball) and 18-crown-6 (red – oxygen, green – carbon, hydrogen atoms omitted). Structure a) was derived from the PubChem database (https://pubchem.ncbi.nlm.nih.gov, CID 28557), while structure b) is reprinted from ref.[154] (https://doi.org/10.1039/D1QO00699A) under Attribution-NonCommercial 3.0 Unported (CC BY-NC 3.0) license.

Remarkable physiochemical properties of crown ethers originate from co-interactions of chemically stable, and conformationally flexible units of ethylene bound to the nucleophilic oxygen atoms. As symmetrically arranged around the ring, an electron-rich cavity able to interact with suitable guests is formed. Moreover, as crown ethers are built of ethylene oxide units, where ethylene is hydrophobic and oxygen atoms are nucleophilic, thus hydrophilic, they can be classified as relatively amphiphilic compounds[155]. The well-tailored design of crown ethers is attractive for diverse applications related to molecular recognition, based on the so-called "host–guest" functionality[154]. Combined experimental and theoretical studies reveal the ion selectivity depending on the crown ether size matching the guest ions[156-157]. Exemplary, 18-crown-6 ether was proven to form complexes with NH_4^+ ions by FTIR and ultrafast IR spectroscopy[157], which is of great importance for studies on crown ethers and amino acid interactions. Overall, supramolecular interactions between "host" and "guest" are driven by multiple factors, such as the relative size of the crown ether cavity (e.g. the number and localization of the oxygen atoms), the charge/size of the cation, the steric hindrance on the crown, and the solvent polarity[158]. Moreover, as a group of macrocyclic compounds, crown

ethers are flexible and can adapt multiple conformations in dependence on their local environment, as proved by Gámez *et. al.*[159] by infrared action spectroscopy experiments and *ab initio* molecular dynamics computations. Additionally, host-guest functionality allows for intramolecular interactions of CE with guest molecules which, as reported by Weirich *et al.*[160] resulted in new signatures detected by vibrational circular dichroism, assigned to the macrocycle compound moiety. In other words, it was shown that the chiral guest molecule (*i.e.* methyl benzyl ammonium cation) can change the conformation of a macrocyclic host: from a highly symmetric to a chiral ring. Additionally, organic probes based on CE architectures have been already utilized as fluorescent sensors[161]. The fluorescence of the aforementioned sensors, in some cases, presented enantioselective responses toward chiral analytes, inorganic cations, and L-amino acids. However, as intrinsically non-fluorescent, CE need to be beforehand functionalized, e.g. with covalently linked chromophores.

Due to the intrinsic properties of crown ethers, their production has been already optimized for a large scale, and the number of commercially available molecules based on macrocyclic ethylene oxide oligomers is constantly growing. They are commonly used in organic chemistry as phase transfer agents. Moreover, they find applications in the biomedical industry (e.g. as antitumor agents)[162], sensors, or drug delivery systems[155]. Crown ethers are also employed for molecular recognition or separation (e.g. as stationary phase in chromatography)[163]. Therefore, there is a need for chemical modification of crown ethers – functionalization – realized according to two main approaches: (1) templated macrocyclization, where pre-functionalized starting materials are used, and (2) direct functionalization of macrocyclic compounds. Among numerous functional groups, crown ethers can be also functionalized with a thiol group (-SH), being of great importance for gold nano-chemistry. If functionalized with a thiol group (-SH), crown ethers and their remarkable physicochemistry can be employed to stabilize the atomically-precise nanoclusters, which opens up distinct pathways for the development of nanomaterials which are both, functional and smart, i.e. selectively reacting to the closest environment.

5.2. Gold nanoparticles stabilized with functionalized (-SH) crown ethers

The gold nanoparticles stabilized with a functionalized 18-crown-6 ether (*i.e.* 2-(mercaptomtethyl)-12-crown-4 ether) were studied by UV-Vis spectroscopy, electron microscopy, dynamic light scattering, and zeta potential measurements by M. Brust group[164]. They presented spontaneous nanoparticles agglomeration based on attractive hydrophobic interactions of complexed crown-ethers competing with electrostatic repulsion, which is fully reversible throughout temperature treatment. However, their studies were focused on nanoparticles of plasmonic nature (with a diameter of ~ 7 nm). Interestingly, crown ether mercaptans are effective in the modulation of plasmonic nanoparticles hydrophobicity by interaction with small cations[165-166]. Namely, the directional ion transport from droplets containing barium ions to those containing sulfate has been achieved (in a water-in-chloroform emulsion). Therefore, plasmonic gold nanoparticles were proven to become more hydrophobic upon ligands complexation with Ba^{2+}.

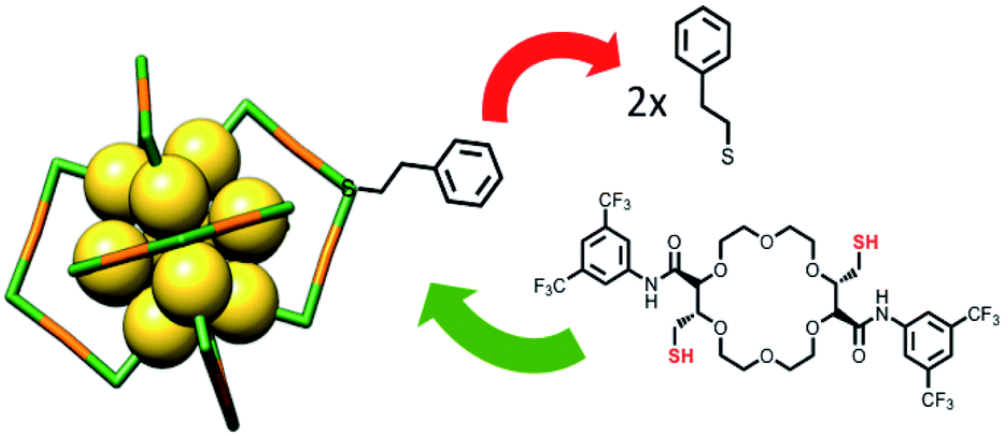

Figure 24. Schematic representation of $Au_{25}(PET)_{18}$ nanoclusters ligands exchange. Ligands: PET (2-phenyl ethanethiol) to C_2-trans t-crown ether. Reprinted from ref.[167] (https://doi.org/10.1039/D1SC01654G) under Attribution-NonCommercial 3.0 Unported (CC BY-NC 3.0) license.

Crown ether mercaptans as ligands for atomically-precise nanoclusters have been scarcely studied. The Bürgi group reported research on combined spectroscopic studies on post-functionalized Au_{25} cluster as an ATR-FTIR sensor for cations (see fig. 24)[168]. Their pioneering work proved that cluster functionalization with di-thiolate crown ether ligand can serve for the detection of K^+, Ba^{2+}, $Gd^{3+,}$ and Eu^{3+} ions, as confirmed by the ATR-FTIR method. They showed that cation complexation leads to the spectral changes of 18-crown-4 moiety (in the 1034 cm^{-1} region, which is corresponding to the C-O stretching vibration of the crown ether unit). Therefore, supramolecular ligands can be utilized for the synthesis of functional nanoclusters, prone to interact with other molecules by non-covalent bonding. However, the amphiphilic properties, being of great importance for interactions with biological samples, have been not probed at all.

5.3. Amyloids and crown ethers

Y. Tian *et al.*[169] showed that 12-crown-4 ether was attenuating the aggregation process of amyloid-β (Aβ), due to the complex formation with positively charged amino acids, by forming hydrogen bonds. In detail, they hypothesized that 12-crown-4 ether interacts non-covalently with R5 (arginine-5), K16, K28 (lysine-16, 28), and H13, H14 (histidine-14, 14). It was established that K16 and K23 are crucial amino acids for the misfolding process of amyloid-β because they participate in the formation of the intra-peptide salt bridges (with aspartate (D23)), which stabilize the entire structure of the amyloid-β fibrils. Interestingly, zeta-potential tests showed that 12-crown-4 ether alters the surface charges of Aβ (from -48 mV to -4 mV). Therefore, crown ether was found to perturbate the hydrophobicity and surface charge of amyloid-β oligomers, attenuating aggregation into mature fibrils. Similar observations were reported for lysozyme amyloids, for which the presence of 18-crown-6 ether significantly retarded or even stopped the aggregation process[170]. Moreover, 12-crown-4 interaction with amyloid-β trimer has been studied by molecular dynamics simulations. Agrawal and Skelton[171]

observed three possible binding modes of 12-crown-4 ether to amyloid fibrils, being closely dependent on the hydrophobic core of the fibril itself (see fig. 25).

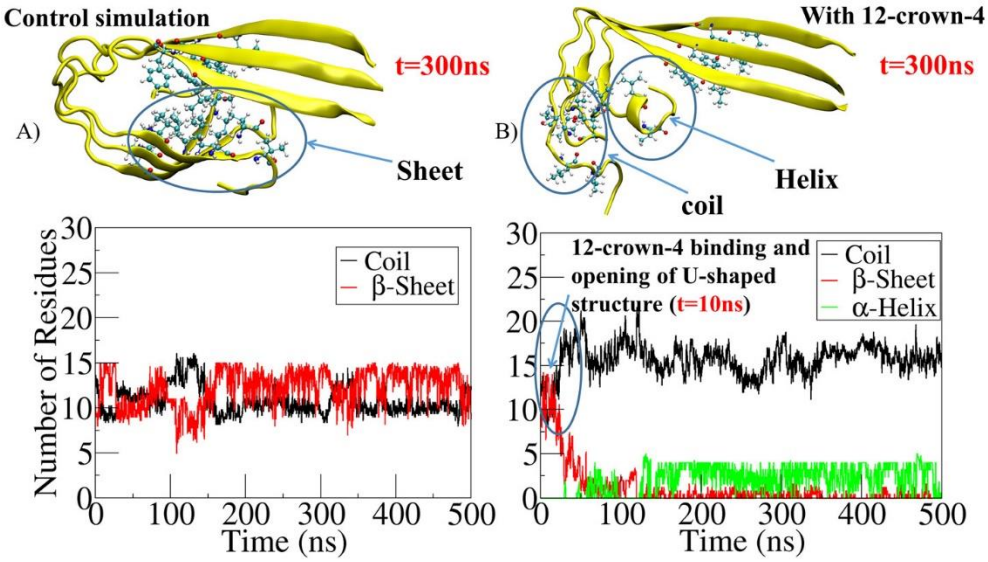

Figure 25. Amyloid fibrils and crown ethers: simulation. Left panel – control sample (Aβ-40) and corresponding time evolution of amyloid secondary structure (dominated by β-sheets over entire simulated timescale). Right panel – Aβ-40 interactions with 12-crown-4 ether and corresponding time evolution of amyloid secondary structure: conversion of β-sheets to α-helixes. Reprinted from ref.[171] (https://doi.org/10.1021/acschemneuro.6b00185), Copyright © 2016 American Chemical Society.

According to their simulations, crown ether enters between two corresponding β-sheets and interacts with hydrophobic residues *via* van der Waals interactions. As a result, the hydrogen bonds network is disrupted and the conversion of β-sheet into a random coil and α-helix becomes favorable. Therefore, bare 12-crown-4 ether remodels the entire structure of amyloid-β-40 fibrils: breaks the Asp23 – Lys28 salt bridge, and interlocks Lys16 (that stabilizes antiparallel arrangement of the cross-β network).

The amphiphilic properties of crown ethers are already of great importance for studies on amyloid aggregation, as highlighted in the paragraphs above. However, their physicochemical properties are simultaneously attractive for bio-imaging, in general. With an assumption that a staining agent based on crown ether architecture inherits supramolecular properties, it might be prone to interact with hydrophobic domains of a variety of biomaterials. Spatially resolved description of e.g. protein surface polarity (and other properties based on non-covalent interactions) is costly, and time-consuming[172]. Since the majority of markers for fluorescence microscopy are target-selective, their range of applications is limited to the specific structures[111], and they are also dependent on complex chemical processing, being time and resource consuming. In contrast, a limited attention has been given to the cost-effective functional and multimodal bio-imaging methods for preliminary structural studies on bio-interfaces. Therefore, the introduction of multimodal probes being prone to simultaneously interact with multiple bio-materials and potentially detect the hydrophobic domains is of great need, and may be valuable for preliminary description of variety of bio-materials.

CHAPTER II – Experimental – PS-2PFM

The interdisciplinary nature of my studies resulted in the involvement of multiple research techniques, e.g. polarized light microscopy, fluorescence microscopy, atomic force microscopy, transmission/scanning electron microscopy, UV-Vis spectroscopy, and FT-IR (Fourier-transform infrared) spectroscopy. Techniques enlisted herein are commercially available and widely exploited in modern science, therefore only a brief characterization of them will be given in the following chapters. However, polarization-sensitive two-photon excited fluorescence microscopy (PS-2PFM) is my method of choice and the main source of data presented in the Chapters, no. III, and IV. Research performed with this technique was based on a complex and non-commercially available optical setup, thus its description will be provided down below. The description will be based on works of S. Brasselet and J. Zyss[173 174] at ENS de Cachan in France, and employed for the interpretation of polarization of two-photon excited fluorescence (2PF) and second harmonic generation (SHG) in the molecular assemblies, monolayers, crystals, and gold surface. J. Olesiak-Bańska and co-workers[175-176] broadened the range of PS-2PFM to systems of biological origin (DNA liquid crystals) and nanotechnology (single gold nanoparticles). In this dissertation the intrinsic nonlinear optical properties of amyloids (*i.e.* two-photon excited autofluorescence) and their correlations with the amyloids' structural features were pioneeringly studied with PS-2PFM.

1 Photo-selection: one-, two-, and three-photon excitation

To describe the photo-selection phenomena, let us consider an isotropic sample characterized by fixed dipoles, and parallel orientation of absorption and emission dipole moments, in the XY macroscopic plane. When an incident field (E, with a chosen polarization angle α) is applied, the highest probability of absorption will be observed for molecules whose transition dipole moments are parallel to the incident polarization. Nevertheless, molecules that are not parallelly oriented also can be excited, but with significantly lower efficiency. Overall, the probability of absorption (P_n) can be expressed with the equation (9):

$$P_n \propto cos^{2n}\theta \tag{9}$$

Where:

n : number of exciting photons
θ : angle between transition dipole moment and incident filed polarization

The mutual relation of the angle between molecular transition dipole moments and incident field polarization (denoted as θ) is governing the probability of absorption between the |0> and |1> molecular energy levels. If two dimensional (2D) plane is considered (XY plane), a characteristic angular distribution of excited states is expected, see figure no. 26. Nevertheless, in three-dimensional space (3D), the angular distribution of excited states can be described by a function of cylindrical symmetry. However, for two- and three-photon excitation, the absorption probability is proportional to $cos^4\theta$, and $cos^6\theta$, respectively. Therefore, under the multiphoton excitation, the width of the polarimetric response, *i.e.* angular distribution of emission intensity (as analyzed both, in 2D and 3D), is expected to be reduced. Consequently, the higher order excitation can provide higher accuracy for the read-out and subsequent calculation of the molecular orientation.

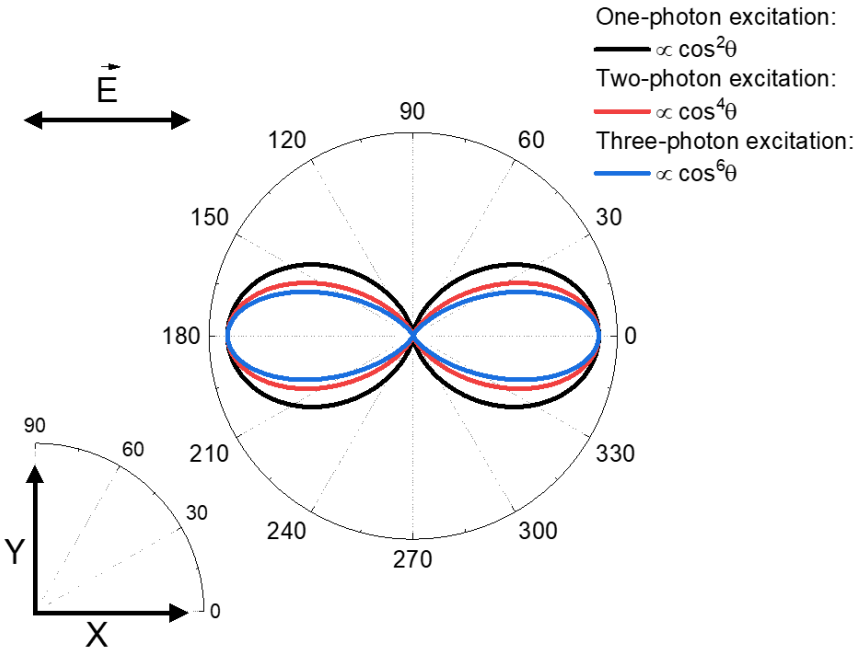

Figure 26. Excitation photo-selection. Two-dimensional fluorescence intensity angular distribution of an isotropic sample, as excited by one-, two- and three-photon processes (black, red, blue, respectively). Polarization of the incident field is denoted with the double-headed arrow (horizontal, to the XY macroscopic sample plane).

Therefore, due to the photo-selection phenomena, PS-2PFM can reveal information about molecular ordering within the sample.

2 PS-2PFM: microscope setup and the open cone model

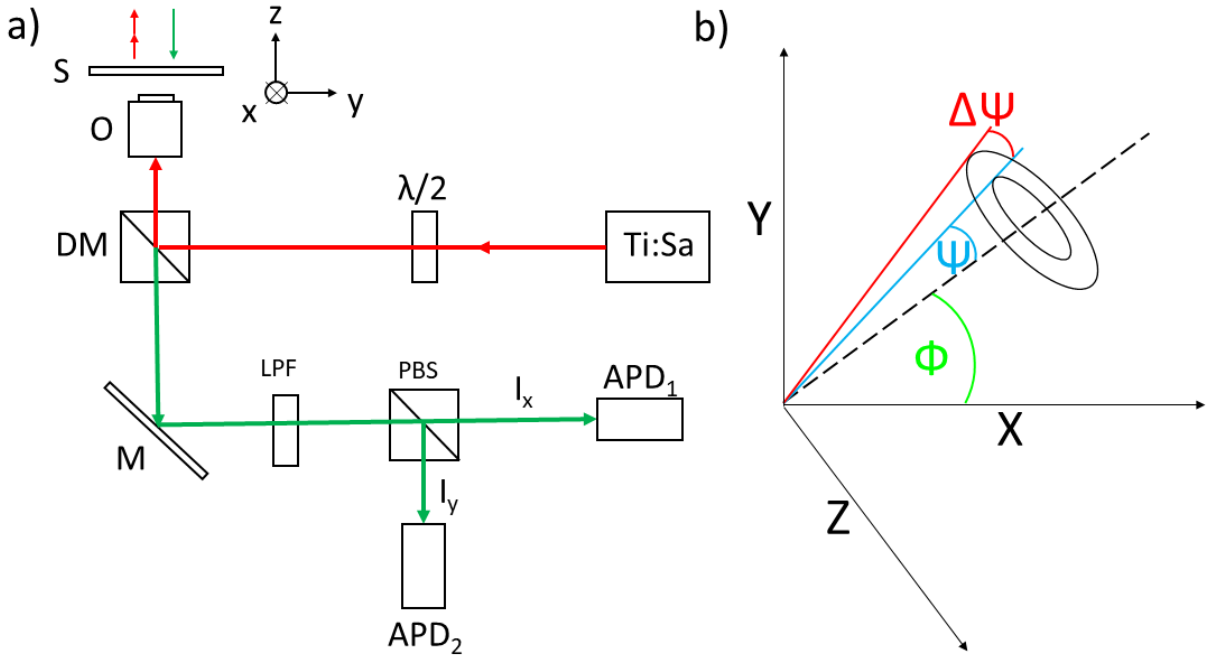

Figure 27. Experimental setup and corresponding to it schematic representation of a mathematical model for the data analysis. a) PS-2PFM setup: S –sample on a piezo stage, O – objective, DM – dichroic mirror, λ/2 – half-wave plate, Ti:Sa – Ti:Sapphire laser source, M – mirror,LPF – optical filter, PBS – polarizing beam splitter, APD_1, and APD_2 – avalanche photodiodes. Horizontally and vertically polarized emission components are donated with I_x and I_y, respectively. b) Open-cone model: schematic representation of Ψ (half angle of the conical distribution of the emission dipole of the fluorophore), ΔΨ (aberrations of Ψ due to the molecular rotations), and Φ (rotation of the fluorophore (*i.e.* amyloid fibril) in the XY microscope sample plane) angles in the xy microscopic sample plane. Adapted from reference no.[54] (https://doi.org/10.1021/acs.jpclett.0c03511). Copyright © 2021 Patryk Obstarczyk, Maciej Lipok, Maneula Grelich-Mucha, Marek Samoć, Joanna Olesiak-Bańska, Published by American Chemical Society.

Polarization-sensitive two-photon excited luminescence images were retrieved with a custom-built optical system. It was previously described in the dissertation of V. Le Floc'h and J. Olesiak-Bańska, and it was adapted for the needs of my research. A schematic representation of our PS-2PFM setup is presented in figure no. 27 a. In principle, fs mode-locked Ti : Sapphire laser (~100 fs, 80 MHz, Chameleon, Coherent Inc.) - with the incident wavelength range tunability (690 – 1080 nm), and average power of a few mW - was used as the excitation light source. The laser output was passed through a half-wave plate mounted on a rotation stage, to control the polarization angle of the incident electromagnetic field (in relation to the XY sample plane). The samples were mounted on a piezoelectric scanning stage (Piezojena, TRITOR 102) and scanned (in XY plane, for a chosen Z). Our setup operates in epi-detection mode, where the incident and emitted signals are passing by the same objective. The laser beam (of chosen polarization) was reflected by a dichroic mirror and focused on the sample by high-numerical aperture objective (Nikon Plan Apo Oil Immersion 100x/1.4 NA). The

collected signal was split by a polarizing beam-splitter into two orthogonally polarized I_x and I_y components. Both beams were detected by two avalanche photodiodes, APD (IDQ id100). The relative ratio of X-APD and Y-APD detection efficiency was determined beforehand, by using isotropic sample (randomly organized immobilized fluorescein molecules). The emission spectra were collected, with a spectrograph (Shamrock 303i Andor). Polarization data presented in both following chapters (*i.e.* chapters III, and IV) was obtained with the 750 – 810 nm range of excitation. The power of the incident beam was ranging from 100-900 µW to 10-50 µW (for autofluorescence, and ThT labeled samples, respectively). The experimental conditions were set in a way to prevent sample photobleaching and ameliorate a high signal-to-noise ratio.

To analyze the data we adapted the mathematical model previously utilized to reveal the information about molecular ordering of dyes in biological membranes and DNA[173, 177] . However, one should note that presented herein concept is related to distinctive scales, from macroscopic to microscopic. From now on, the molecular assembly in plane will be referred to with the (x, y, z) notation, and defined as the microscopic plane. Correspondingly, the (X, Y, Z) notation will be referring to the macroscopic frame (laboratory frame – sample plane), whereas Z is the direction of propagation of the incident light.

For each fluorophore, the two-photon fluorescence emission intensity (I_{2PE} or 2PEF) is proportional to the probability of two-photon absorption P_{abs2}, being dependent on the transition dipole moment ($\overrightarrow{\mu_{abs}}$), and incident electric field ($\overrightarrow{E_\omega}$). However, in terms of emission, its probability (P_{em}) is dependent on molecular emission dipole ($\overrightarrow{\mu_{em}}$), and the detection polarization analysis axis ($\overrightarrow{\mu_I}$) . The aforementioned relations can be expressed with the following equations (10, 11):

$$P_{abs2} \propto |\overrightarrow{\mu_{abs}} \times \overrightarrow{E_\omega}|^4 \quad (10)$$

$$P_{em} \propto |\overrightarrow{\mu_{em}} \times \overrightarrow{\mu_I}|^2 \quad (11)$$

Thus, the angular analysis of the X and Y components of two-photon excited fluorescence intensity (dependent on the incident light polarization - α) were performed, according to the equation (12):

$$I_{2PE}(\alpha) \propto \int |\overrightarrow{\mu_{abs}}(\Omega) \times \overrightarrow{E_\omega}(\Omega)|^4 \, |\overrightarrow{\mu_{em}}(\Omega) \times \overrightarrow{\mu_I}|^2 d\Omega \quad (12)$$

Whereas, the integration is conducted over the orientation distribution of absorption and emission dipole moments vectors, restricted within the solid angle Ω. Therefore, the function f(Ω) was introduced as a base for the open-cone model (see fig. 27b) and the following paragraphs will briefly describe this concept.

Let us consider the macroscopic experimental framework (X, Y, Z), where the Z direction is perpendicular to the sample plane and parallel to the optical axis of the objective. Consequently, the X and Y axes comprise the sample plane. The incident light propagates along the Z axis with polarizations directions corresponding to X and Y axis (I(α)). Within this experimental framework, a molecule with the transition dipole moment $\vec{\mu}$ can be two-photon

excited. However, in the focal volume, the assembly of molecules is excited. Therefore, we need to take into account the superposition of N single molecules (in the detected focal volume). Consequently, the molecular angular distribution can be expressed as the orientation distribution function (13):

$$N(\Omega)d\Omega = Nf(\Omega)d\Omega \tag{13}$$

Where $d\Omega$ can be defined as the solid angle increment ($d\Omega$ = sin $\theta d\theta d\phi$), and $f(\Omega)$ corresponds to the molecular orientation distribution function, being dependent on Ψ (and ΔΨ), according to the equation (14):

$$f(\theta,\phi) = \frac{exp(-\frac{\phi-\Psi}{\Delta\Psi})^2}{2\pi\sqrt{\pi}\sin(\Psi)\Delta\Psi} sin\theta d\theta d\phi \tag{14}$$

For the assumption that transition dipole moments are colinear ($\overrightarrow{\mu_{abs}} = \overrightarrow{\mu_{em}} \propto \vec{\mu}$), the polar and azimuthal angles θ and ϕ can be used to describe the $\vec{\mu}$ components (figure no. 28, equation no. 15):

$$\begin{bmatrix}\mu_x(\theta,\phi)\\ \mu_y(\theta,\phi)\\ \mu_z(\theta,\phi)\end{bmatrix} = \begin{bmatrix}sin\theta\ cos\phi\\ \sin\theta\ sin\phi\\ cos\theta\end{bmatrix} \tag{15}$$

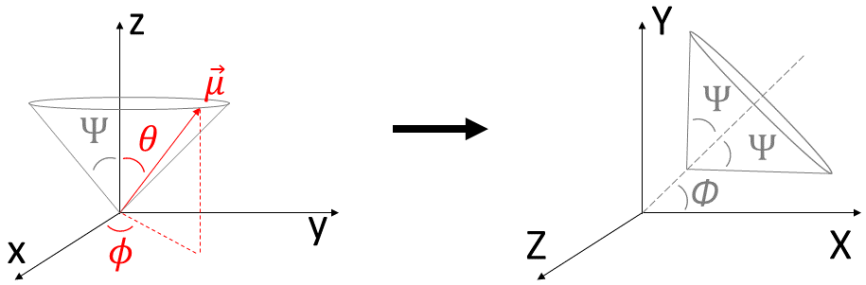

Figure 28. From microscopic to the macroscopic experimental framework. Microscopic experimental framework xyz with a distribution of molecular dipole moments $\vec{\mu}$, in an open-cone, with an aperture Ψ (left). Corresponding XYZ macroscopic framework with an angle Φ, describing cone orientation (right). Based on ref. no.[173] (*https://doi.org/10.1364/AOP.3.000205*).

The description of an incident filed $\overrightarrow{E_\omega}$ can be simplified by using a planar wave function propagating in the Z direction. Under interactions with the optics within the microscope body (e.g. reflection by the dichroic mirror), it can be depolarized, according to equation (16):

$$\overrightarrow{E_\omega}(\alpha,\delta,\varepsilon,\omega t) = \frac{E}{\sqrt{1+(1-\delta)^2}}\begin{pmatrix}\cos(\alpha)\cos(\omega t)\\ (1-\delta)\sin(\alpha)\cos(\omega t+\varepsilon)\\ 0\end{pmatrix} \tag{16}$$

Where:

E : amplitude of the incident field
α : incident polarization angle in the XY reference plane

Parameters ε and δ are factors describing the variation of the incident field by polarization mixing and depolarization effects caused by used optics. The former is defined as the ellipticity (introduced by reflecting on the dichroic mirror), while the latter corresponds to reflectivity differences for a horizontal (X-aligned) and vertical (Y-aligned) polarization of incident light.

Overall, the probability of TPA can be expressed as a summation of tensorial products of absorption dipoles and excitation fields, by using scalar values (eq. 17):

$$P_{abs2} = \mu_{abs,X}^4 E_X^4 + \mu_{abs,Y}^4 E_Y^4 + 6\mu_{abs,X}^2 \mu_{abs,Y}^2 E_X^2 E_Y^2 + 4\mu_{abs,X}^3 \mu_{abs,Y} E_X^3 E_y + 4\mu_{abs,Y}^3 \mu_{abs,X} E_Y^3 E_X \quad (17)$$

The probability of emission is modified by the high numerical aperture objective (focusing), the birefringence of the sample, or by the excitation transfer between fluorophores in highly concentrated samples. Enlisted effects are reflected in the angular dependence of two-photon excited fluorescence. The influence of the dichroic mirror ellipticity, as well as the high numerical aperture of the objective were described in the dissertation of V. Le Floc'h[174] and translated to our model. Overall, the absorption and emission polarization properties of molecules, upholding the assumption: $\overrightarrow{\mu_{abs}} = \overrightarrow{\mu_{em}} \propto \vec{\mu}$, can be described with a f_{WIJKL} factor (18):

$$f_{WWIJKL}(\theta, \phi) = J_W(\theta, \phi)\ x\ a_{IJKL}(\theta, \phi) \quad (18)$$

Where:

W : polarization of the detection (W ∈ [X, Y, Z])
J_W : detection probability
a_{IJKL}: coefficient preceding the field amplitudes (where I, J, K, L - incident light polarization (I, J, K, L ∈ [X, Y]))

Thus, the total two-photon excited fluorescence intensity, collected from the focal plane, can be calculated for a conical distribution of fluorophores according to the equation below (19):

$$I_{2PE}(\alpha, \delta, \varepsilon) = \int_0^{\pi} \int_0^{2\pi} f_{WWIJKL}(\theta, \phi)\ E_I\ E_J\ E_K\ E_L(\alpha, \delta, \varepsilon) sin\theta d\theta d\phi \quad (19)$$

For the needs of this dissertation, the polarization data fitting and numerical calculations were performed with a custom-written Spyder Python 3 IDE (supported by NumPy and SciPy libraries) script, authored by M. Lipok[54, 178]. From now on, I will be operating with several parameters (half aperture of a cone - Ψ, with a variable thickness - $\Delta\Psi$, and its orientation angle - Φ – see fig. no. 27b) derived from calculations based on the as-described open-cone model. The enlisted angular parameters consist the results of analysis of the two orthogonally polarized (to the X and the Y axis, correspondingly) two-photon excited emission components,

supported by point-spread function describing the spatial distribution of the incident beam in a aperture-limited focus of a microscope setup.

CHAPTER III – Results – Two-photon excited polarization-dependent autofluorescence of amyloids

In this chapter, I show that the two-photon excited autofluorescence of amyloids is highly polarized and its angular distribution is tied up to the long axis of the fibrils within the cone ~ 30°. The control sample, consisting of ThT-labelled amyloid structures, was also studied with the polarization-sensitive two-photon fluorescence microscopy (PS-2PFM), and the same conical distribution of the amyloid-specific dye, in comparison to label-free samples, was observed. Herein, amyloid label-free and ThT-stained spherulites were utilized as a model of highly organized fibrillar structures. Within the frames of this thesis, the polarization analysis of the amyloid intrinsic nonlinear optical properties was pioneeringly performed. The research results presented herein may serve as the basis for the application of amyloid autofluorescence polarization analysis for the label-free determination of the organization of fibrils in various structures, or stain-free bio-imaging in general.

1 Introduction: the scientific problem

The modern diagnosis of amyloid-related diseases as well as the investigations on the origin and biological function of amyloid-like structures is limited due to the lack of fast, non-destructive, and sensitive *in vivo* methods[1, 6]. Moreover, in living organisms the detection and structural characterization of proteinous aggregates is extremely challenging as it needs to be performed in densely packed, hydrated, and complex environments. Among others, fluorescence microscopy might be the method of choice for bio-imaging[146, 179]. Due to the distinctive intermolecular interactions with β-sheet-rich structures, Thioflavin-T (ThT) and its analogs have been commonly applied as selective fluorescent markers for amyloids[58]. These dyes, as well as the family of molecules based on Congo Red (CR) architecture, bind to mature fibrils, while their interactions with the oligomeric intermediates are limited[55, 60]. Moreover, the distinctive orientation of the aforementioned molecules, upon binding to amyloid structure, was already utilized in polarization-sensitive techniques. As an example, Brasselet *et al.*[56] studied amyloid fibrils organization by the polarization analysis of ThT and Congo Red fluorescence. Although there are numerous dyes designed to stain amyloid fibrils[61, 69], their presence may strongly perturb the amyloid aggregation process, and even alter the amyloid aggregate structure. For instance, the golden standard of amyloid imaging – ThT – up to this day, arouses controversy over fibril-binding modes and their impact on the aggregation process[53, 55, 180]. In addition, a variety of factors (e.g. ionic strength, or electrostatic interactions with peptides) may affect the binding sites of the dye[58]. Therefore, the development of structural analysis methods for the amyloid aggregates investigations, that can be performed in a label-free manner, would be beneficial.

The amyloid autofluorescence (intrinsic fluorescence of amyloid aggregates), as comprehensively described in the literature review (see chapter I), is a peculiar optical property of β-shit rich structures. In brief, it is characterized by 340 – 450 nm emission[181]. Interestingly, for the aforementioned phenomenon, the presence of aromatic residues or multiple covalent bond conjugations is not a prerequisite[48]. The origin of this amyloid-specific property is still widely debated and poorly understood, especially if the nonlinear optical processes are taken into account[150]. As described before, amyloid autofluorescence may arise from the delocalization of electrons through hydrogen bonding, or due to the proton transfer[50]. However, it is connected to amyloid-like structures molecular architecture, and its utility in *in vivo* imaging was already presented[182].

Bearing in mind the problems and phenomenon presented in the preceding paragraphs, I decided to investigate if the amyloid autofluorescence will present incident light polarization-dependent excitation and emission, under a multiphoton excitation. I hypothesized that emission dipoles (responsible for the autofluorescence) can be correlated to the orientation of amyloid fibrils, as it is a structure-dependent phenomenon. I utilized polarization-sensitive two-photon microscopy (PS-2PFM), as it provides superior optical merits (e.g. reduced angular distribution of photo-selection), in comparison to one-photon processes (as described in Chapter II, subchapter no. 2). Johansson *et al*.[151] already showed that amyloid spherulites can be imaged thanks to their nonlinear optical properties (i.e. SHG, two-photon excited

fluorescence). Therefore, for my studies, amyloid spherulites were chosen as a model of highly organized amyloid fibrils.

2 Comments and acknowledgments

Part of the data presented in this chapter is published in Obstarczyk, P.; Lipok, M.; Grelich-Mucha, M.; Samoć, M.; Olesiak-Bańska, J., Two-Photon Excited Polarization-Dependent Autofluorescence of Amyloids as a Label-Free Method of Fibril Organization Imaging. *The Journal of Physical Chemistry Letters* **2021,** *12* (5), 1432-1437. The experimental data fit was performed with a custom-written script by M. Lipok (see chapter II). The AFM imaging was performed due to courtesy of M. Grelich-Mucha.

3 Materials and experimental methods

3.1. Chemicals

All chemicals were used as purchased, without further purification. Insulin from the bovine pancreas (≥25 units/mg (HPLC), I5500), sodium chloride (NaCl, BioXtra, > 99.5 %), and Thioflavin T (ThT) were purchased from Sigma-Aldrich, in powder form. Mili-Q quality water (resistivity: 18.2 MΩ·cm @ 25 °C) was used throughout all the experiments. Hydrochloric acid (≥37%, APHA ≤10), and DPX mountant for histology (slide mounting medium) were also purchased from Sigma-Aldrich.

3.2. Amyloid spherulites incubation

To prepare amyloid spherulites, 10 mg of bovine insulin powder was dissolved in 1 mL of Mili-Q water/HCl mixture (pH 1.5). In the following step, the solution was incubated in an Eppendorf Thermomixer C (70 ◦C, 24h, 0 rpm). To obtain ThT-labelled spherulites, the same protocol was applied, however, with an addition of 0.5 mg of the ThT dye. The aforementioned processes were conducted in 1.5 mL Eppendorf Safe-Lock Tubes (polypropylene) sealed thoroughly with PTFE thread seal tape.

For the PS-PTFM the main samples (with spherulites) were prepared in salt-free conditions. However, the control samples (in form of amyloid fibrils) were additionally prepared. The same protocol, as described above was utilized. However, the incubation parameters were altered and set to 70 ◦C, 24h, 700 rpm. The corresponding fibril solutions were prepared in salt-free conditions, and with an addition of NaCl. The final concentration of salt was set to 10, 50, and 100 mM.

3.3. Sample preparation for microscopy

To perform imaging in the hydrated environment, the corresponding solutions with amyloid aggregates had to be protected from evaporation. Therefore, sealed samples were prepared. In detail, a 100 µL aliquot of the as-incubated spherulite-containing solution was pipetted into wells in microscope slides (Super White Glass, 76 × 26 × 1 mm, CHEMLAND). In the next step, filled wells were covered with coverslips (Super White Glass, EQUIMED). The as-prepared samples were sealed with DPX mountant, near glass edges (by careful pipetting). After that, samples were left for 24h at 5 °C for the mountant to harden. The sealed microscopic samples design is presented in the figure below (no. 29):

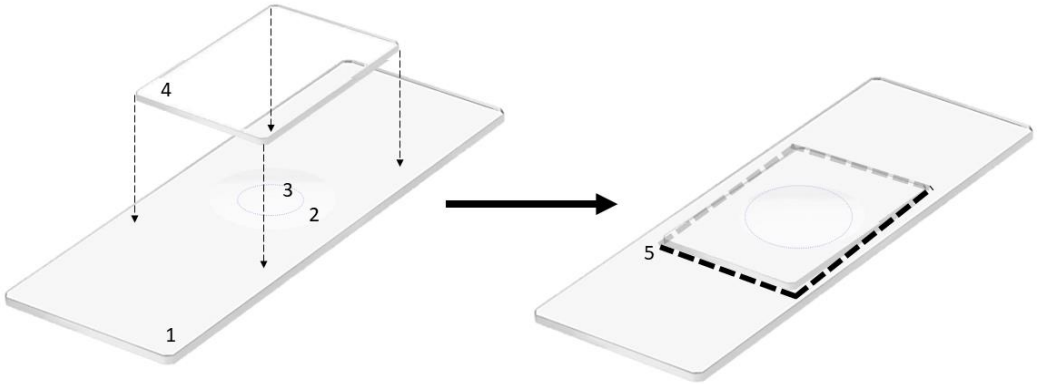

Figure 29. Schematic representation of the sealed sample for microscopy. The solution with spherulites was put between the microscopy slide (with a well), and coverslip. In the following step, the entire system was sealed with hardening polymer. Numbers correspond to 1 – microscopy slide with a well, 2 – well, 3 – a drop of the spherulites-containing solution, 4 – coverslip, and 5 - hardened polymer (DPX mountant).

3.4. UV-Vis spectroscopy

The UV-Vis spectra as well as the fluorescence measurements were performed with a JASCO V-670 spectrometer and Shamrock 303i Andor spectrograph. One-photon autofluorescence of amyloids and ThT emission were registered for 375 nm excitation. All measurements were performed in a QS high-precision cell (10 mm optical length, Hellma Analytics).

3.5. Fluorescence, bright-field, polarized light, atomic force, and scanning electron microscopy

All solutions were imaged being locked in the sealed microscopic samples (as previously described -Chapter III, subchapter 3.3.), excluding SEM (scanning electron microscopy) and AFM (atomic force microscopy) imaging.

For electron microscopy imaging, the as-incubated solution (with spherulites) was drop-casted onto the metallic surface and left to dry. The dehydrated sample was inserted into the vacuum coater/sputter (JEOL JEC-3000FC), and covered with a thin layer (~ 10 nm) of gold. The

resulting product, with enhanced conductivity, was imaged under a scanning electron microscope (JEOL JSM-6610LVnx, 15 kV), thanks to the courtesy of A. Żak and P. Cwynar.

To perform atomic-force microscopy imaging, a 100 µL aliquot of the corresponding amyloid fibrils solution (with 0, 10, 50, and 100 mM NaCl) was pipetted onto the mica surface and left for 1 minute to allow the sedimentation. After that, the mica surface was washed with 5 mL of Mili-Q water and left to dry under ambient conditions. The remaining dry samples were imaged. AFM images were obtained using a Dimension V Veeco AFM instrument (in the tapping mode) and analyzed with the Nanoscope 7.30 software.

The analysis of spherulite population size distribution was performed based on images taken with an Olympus BX60 optical microscope. Fluorescence imaging was performed for the excitation wavelength set in the 300 - 400 nm range, in a wide-field epifluorescence mode. To perform polarized-light microscopy imaging, the aforementioned microscopy setup was additionally equipped with two orthogonally crossed polarizers. The spherulites chosen for PS-2PFM imaging, were localized and photographed in a bright-field mode as well as under crossed polarizers with Nikon Plan Apo Oil Immersion 100x/1.4 NA objective, with a custom-built microscope (PS-2PFM), which was already described in the previous chapter.

3.6. Polarization-sensitive two-photon microscopy (PS-2PFM) – the open-cone model adaptation and additional assumptions

The open-cone model (see Chapter II) correlation to amyloid fibrils architecture is schematically presented in figure no. 30. The amyloid fibrils were found to be composed of several enveloped protofilaments, which results in a helical twist and diverse morphology[44]. The number of the protofilaments that are coiled together is determining the mature fibril cross-sectional width[183]. In our model, the angular distribution of the protofilaments is described with angle Θ. The aforementioned Θ angle serves for the determination of a maximal deviation from the long axis of the mature fibrils. Consequently, the Θ angle contributes to the measured value of Ψ, together with Ψ_0 ($\Psi = \Psi_0 + \Theta$). The Ψ_0 angle describe the deviation of the emitting individuum from the long axis of the protofilament, while Ψ describe the relative angle between the long fibril axis (composed of protofilaments) and the transition dipole moment of fluorophore.

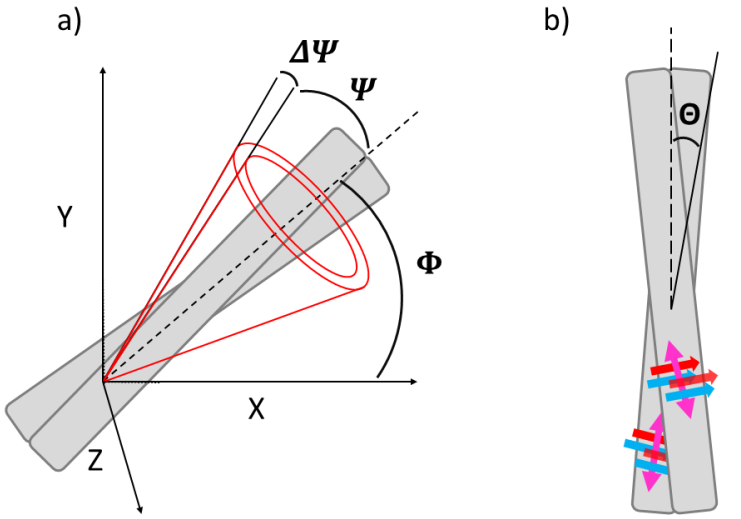

Figure 30. The open cone model for amyloid fibrils. a) The conical distribution of the emission dipole of the dye (half angle, Ψ) to the long fibril axis (dashed line). The rotation of the fibril in the XY microscope sample plane is described by the Φ angle. Aberrations of Ψ due to the molecular rotations in filaments are described by ΔΨ. b) Schematic amyloid fibril model where red and blue arrows represent the β-sheets oriented perpendicularly to the long axis of the protofilament. Emitting dipole binding sites are denoted with a pink double-headed arrow. Θ stands for the angular distribution of the protofilaments that build a fibril (maximal deviation from the long axis of the fibril). Adapted from reference no.[54] (https://doi.org/10.1021/acs.jpclett.0c03511), Copyright © 2021 Patryk Obstarczyk *et al.*, Published by American Chemical Society.

The data sets presented herein were collected and analyzed as described in the previous Chapter, no. II. However, some additional assumptions were made (see fig. no. 30). I aimed to calculate the relative angle between the long fibril axis and the transition dipole moment of autofluorescence - Ψ angle – and compare it to the angular distribution of Thioflavin-T dye bound to amyloid fibrils. In detail, to calculate the Ψ angles, for amyloids stained with ThT as well as for unlabeled ones, 16 data points were used. For the ThT-labelled, and label-free samples correspondingly, two-photon excited photoluminescence of 4 spherulites was mapped and expressed as raster scans. From each of them, 2 spots derived from highly ordered regions were chosen (along X or Y axis) to perform a full polarization analysis. The resulting polar graphs were fitted with model presented in Chapter II.

For calculations, the long fibril axis (Φ angle) was fixed at 0 or 90 degrees, depending on the location of the point which data was collected (either along the X or Y axis). For ThT-labelled samples, the statistical distribution of the Ψ angle was characterized by a gaussian character with the center at 30 – 31 degrees. The label-free samples were characterized by a similar angular characteristic (Ψ = 29) – see fig. no. 31. To calculate the ΔΨ angle, the Ψ value was fixed at 30 degrees. The fit quality was determined according to the R^2 factor, being equal to the 0.71 – 0.81 and 0.81 – 0.89 range for ThT-labelled and label-free samples, respectively.

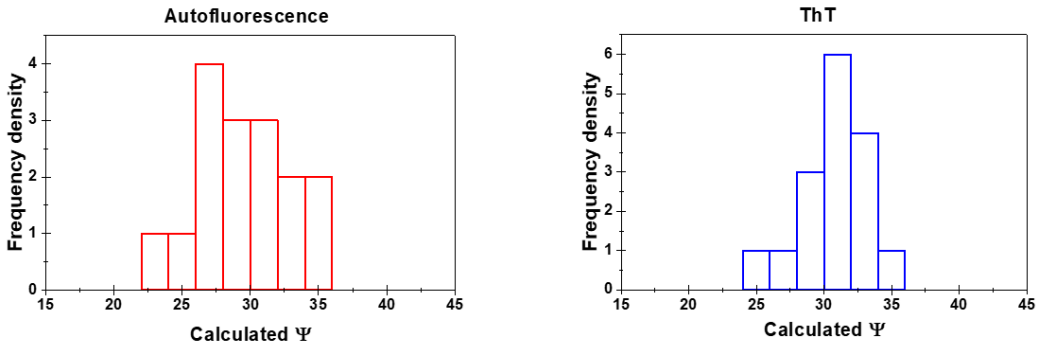

Figure 31. The angular distribution – statistic. The conical distribution of the emission dipole (Ψ) for autofluorescence (red), and thioflavin-T (blue). Adapted from reference no.[54] (https://doi.org/10.1021/acs.jpclett.0c03511), Copyright © 2021 Patryk Obstarczyk *et al.*, Published by American Chemical Society.

4 Results and discussion

I prepared the label-free and ThT-labelled bovine insulin amyloid spherulites. Then, the amyloid aggregates were enclosed in the sealed microscopy samples, as described in the Materials and experimental section (Chapter III, subchapter 3). Subsequently, I performed imaging of the corresponding samples, under the polarized light microscope (with crossed polarizers). As a result, the characteristic anisotropic patterns, namely Maltese crosses, were observed (see figure no. 32), thus the presence of spherulites was confirmed.

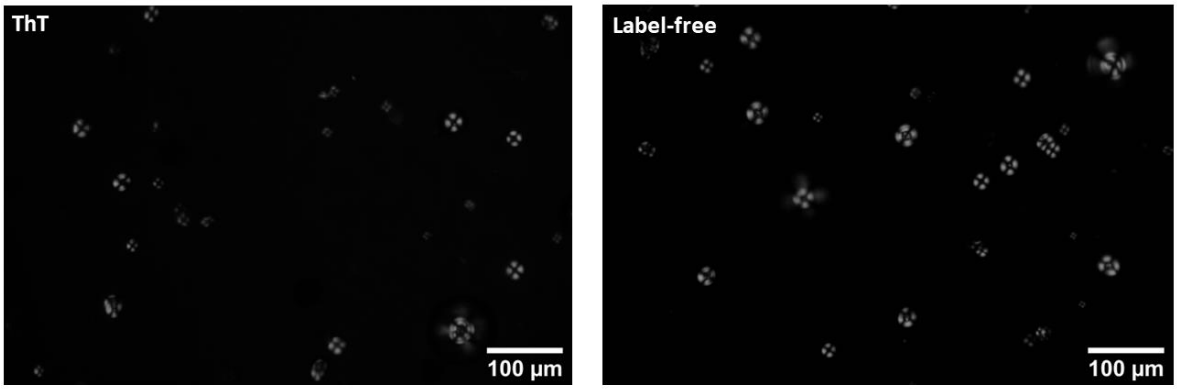

Figure 32. Polarized light optical microscopy images. The population of different sizes of ThT stained and label-free spherulites, as marked in the upper-left corners, was imaged between crossed polarizers.

The Maltase crosses appeared under a microscope with crossed polarizers due to the structural features of amyloid spherulites[14], namely due to the regular arrangement of radially growing amyloid fibrils, being organized around the amorphous core. However, amyloid spherulites are heterogenous in nature[19-20], thus distinct statistical distribution of their sizes was observed for both samples: ThT-labelled and label-free ones. Based on the 150 individual

spherulites (per sample) I measured and analyzed their structural characteristics. The amyloid spherulites' overall diameter was equal to 31.45 ± 9.79 µm and 62.15 ± 49 µm for a stain-free and ThT-labelled samples, respectively. Interestingly, their core sizes were correspondingly equal to 5.41 ± 1.75, and 10.04 ± 2.51 µm. The label-free and ThT-stained spherulites' structural aspect ratio (defined as the overall diameter divided by core diameter) was similar, respectively: 6.55 ± 3.33 and 6.40 ± 1.89 µm. Additionally, SEM imaging of label-free spherulites was performed, as presented in figure no. 33.

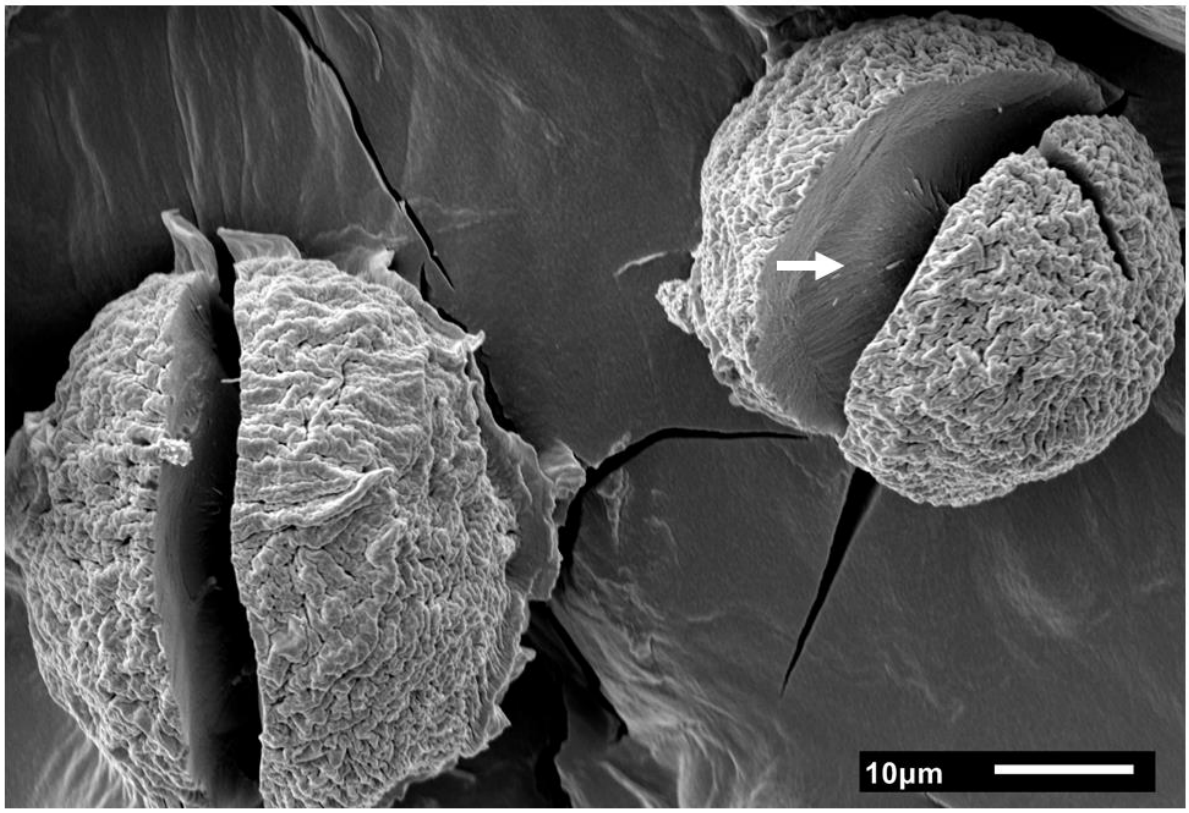

Figure 33. Scanning electron microscope image. The image of the gold-coated (10 nm) and label-free bovine insulin spherulites. Spherulites are dehydrated and cracked, however, the radial organization of fibril-like structures can be spotted, as marked with the white arrow. The scale bar is 10 µm. Adapted from reference no.[54] (https://doi.org/10.1021/acs.jpclett.0c03511), Copyright © 2021 Patryk Obstarczyk *et al.*, Published by American Chemical Society.

Despite the cracking and structural deformations arising due to the dehydration necessary for SEM imaging, the radial organization of fibril-like structures could be visualized (white arrow, figure no. 32). Therefore, the presence of organized fibrils within the spherulites was confirmed, which correspond well to data available in the literature[184].

To perform two-photon excited fluorescence microscopy of spherulites, it was necessary to beforehand investigate the linear optical properties of the samples. Therefore, I measured the one-photon excited emission spectra from both, ThT and unlabeled spherulites-containing solutions (figure no. 34a).

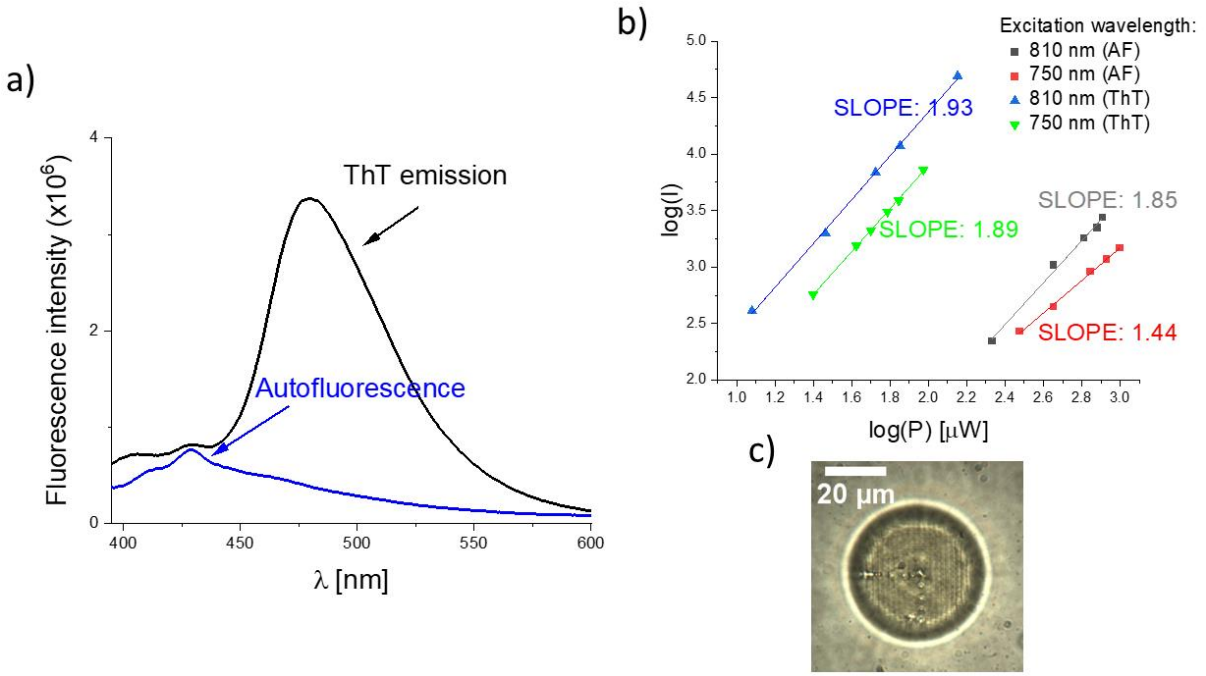

Figure 34. Spherulites optical properties. a) One - photon excited emission of spherulites solution labeled with ThT (excited with 375 nm - black line) and label - free (excited with 375 nm – blue line). b) Two-photon fluorescence (2PF) dependence upon excitation laser power P of thioflavin labeled spherulites (blue and green triangles) and label - free spherulites (grey and red squares) excited with two wavelengths (810 nm and 750 nm, respectively). The presented dependencies are consistent with the two-photon nature of the observed processes. c) Example of a damaged sample, caused by the prelongated laser irradiation. Adapted from reference no.[54] (https://doi.org/10.1021/acs.jpclett.0c03511), Copyright © 2021 Patryk Obstarczyk *et al.*, Published by American Chemical Society.

The registered emission at 425 nm (excited with 375 nm) was in excellent agreement with the literature data[48], thus I identified it as amyloid autofluorescence. Additionally, the emission from the ThT-labelled samples was also corresponding well to the previous reports[53]. In the next step, samples were transferred to the PS-2PFM setup, and excited with the fs mode-locked Ti-sapphire laser (the excitation wavelength was set to 810 and 750 nm). As a result, for the 810 nm excitation, I observed an approximately quadratic dependence of two-photon excited fluorescence (or autofluorescence for label-free samples) on the incident laser power (see figure 34b). Therefore, two-photon excited fluorescence (2PF) was achieved. The laser power was experimentally adjusted to the range allowing to minimalize the structural damage of samples, over an illumination period equal to 60s. Exemplary damaging effects caused by incorrectly adjusted lasing power are presented in Figure 34c.

Due to the insightful analysis of the data presented to this point, I hypothesized that two-photon excited autofluorescence of label-free spherulites can enable their imaging under PS-2PFM. Therefore, I decided to illuminate them with varying directions of the incident light polarization and analyze the directions of two-photon excited emission polarization. Experimental details were comprehensively presented in the Chapter no. II, as well as in the Materials and experimental methods section (Chapter III, subchapter 3).

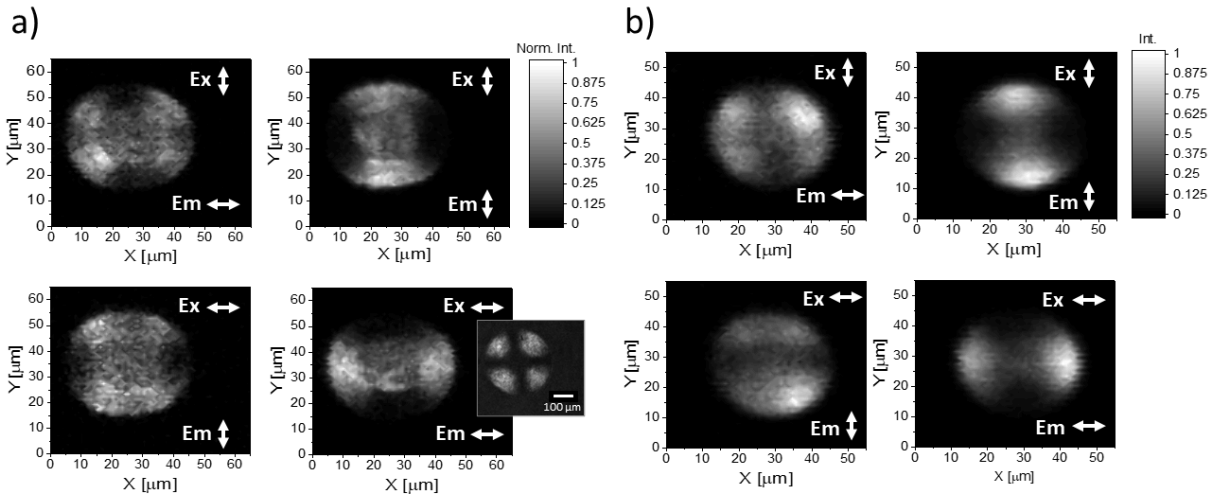

Figure 35. Two-photon excited fluorescence raster scans. Two-photon fluorescence (2PF) intensity raster scans of a label-free (a) and ThT-stained (b) insulin spherulite. The polarization of the excitation beam (Ex) and emission (Em) is denoted with white arrows, and the excitation wavelength was set to 810 nm. Inset shows the same spherulite under a polarized light microscope with crossed polarizers (before two-photon imaging). Adapted from reference no.[54] (https://doi.org/10.1021/acs.jpclett.0c03511), Copyright © 2021 Patryk Obstarczyk *et al.*, Published by American Chemical Society.

I performed two-photon excited fluorescence intensity raster scans of unlabeled and ThT-labelled spherulites (see figure no. 35). The incident light polarization (α angle) was aligned along the X or the Y axis of the sample plane. Horizontal and vertical polarizations are marked with the "Ex" prefix, and white double-headed arrows, in the respective plots. The collected emission components (horizontally or vertically polarized) are similarly marked, however with a different prefix, namely "Em". I observed that the change of the polarization angle of the excitation beam produces the raster scans with patterns characterized by the areas of the strongest two-photon excited fluorescence matching the polarization of the incident light (α angle). In my experiment, the maximum of 2PF was registered for parallel orientation of Ex and Em, thus absorption and emission transition dipole moments are also parallel. Interestingly, the aforementioned phenomenon applies to both, label-free and ThT-stained samples. Moreover, the respective raster scans (see figure no. 34a, and b) present 2PF distribution correlating well with the radial organization of the emitting dipoles. The aforementioned observations, combined with data presented in Figures no. 33 and 34, led me to the conclusion that absorption and emission transition dipole moments of amyloid autofluorescence are mostly parallel to the long axis of the amyloid fibrils. The peculiar structural features of spherulites, namely core-shell morphology and radial organization of fibrils around the amorphous core, were also observed under PS-2PFM. However, in the two-photon excited autofluorescence raster scans (see figure no. 34), some signal is also present in the spherulite nonbirefringent core area, where high ordering or fibrils presence is not expected[185].

The photo-selection phenomenon along with the assumption that molecular transition dipoles of absorption and emission are colinear should produce the highest emission intensity for molecules with the parallel orientation of the aforementioned dipoles in relation to the incident light polarization. Therefore, the simultaneous detection of the X (horizontally) and the Y (vertically) polarized components of 2PF can reveal information about molecular ordering, as for the isotropic sample these components should be perpendicular. Comprehensive description theory as well as the assumptions taken for the need of this experiment were already presented in Chapter II (subchapters 1, and 2) as well as in the Materials and experimental method section (Chapter III, subchapter 3.6.). Hence, to reveal the information about molecular ordering within amyloid spherulites, both the label-free and ThT-stained ones, I measured the angular dependence of 2PF components I_x and I_y on the excitation beam polarization angle α. Thus, several spots from the selected spherulites were chosen and a full polarization analysis (α = 0 - 360°) was performed (see polar graphs, figure no. 36).

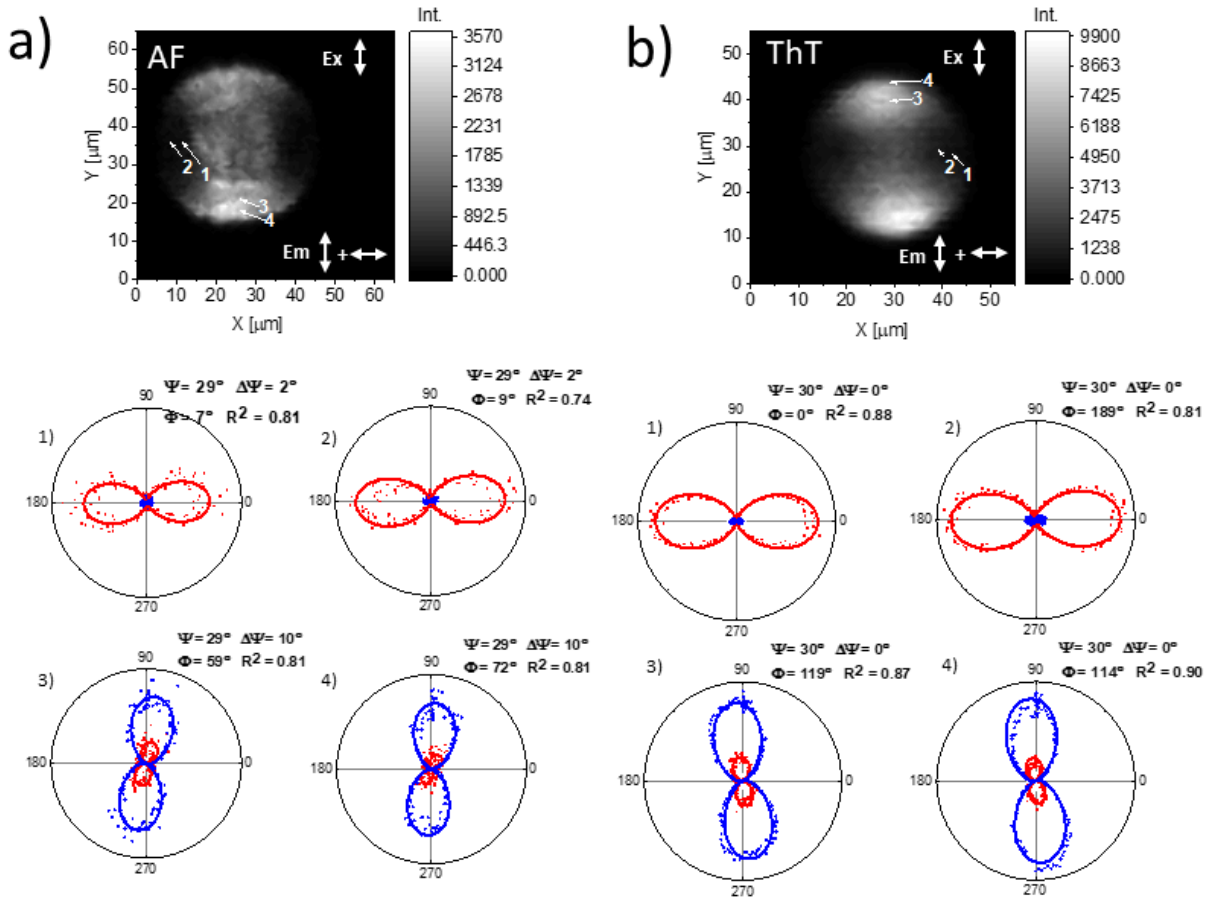

Figure 36. Polarization analysis. 2PF XY raster scans of label-free (a) and ThT-labeled (b) spherulite as excited with vertically polarized light. Polar graphs (1-4) are performed in spots denoted on the scans. Experimental data are presented as dots (I_x, red; I_y, blue), and solid lines present the fitting of the angular dependence of two-photon excited emission. Polarization of the excitation beam (Ex) and emission (Em) are denoted with white arrows. The excitation wavelength was set to 810 nm. Adapted from reference no.[54] (https://doi.org/10.1021/acs.jpclett.0c03511), Copyright © 2021 Patryk Obstarczyk *et al.*, Published by American Chemical Society.

The presented data were fitted according to the model that was already described, see figure no. 30. As a reminder, several angular values are considered, namely the Φ (describing the rotation of the fibril in the XY microscope sample plane), the Ψ (describing the conical distribution of the emission dipole of the dye), the ΔΨ (describing the aberrations of Ψ due to the molecular rotations in filaments), and the Θ (describing the angular distribution of the protofilaments that build a fibril) angles. The calculated and averaged relative angle between the long fibril axis and the transition dipole moments were equal to 29° (ΔΨ = 6°), and 30° (ΔΨ = 0°) for autofluorescence and ThT, respectively. Interestingly, ThT was already proven to reproduce the orientation of the amyloid fibrils, as its molecules were found to selectively bind to β-strands. Therefore, their orientation is perpendicular to the long axis of the fibril protofilaments. In light of the foregoing, two-photon excited amyloid autofluorescence was found to be structure-dependent and able to provide information on fibrils orientation.

However, to comprehensively discuss the angular characteristic of two-photon excited amyloid autofluorescence, some basic information about amyloid fibril architecture is necessary to obtain. Mature amyloid fibrils are composed of several enveloped protofilaments, which leads to the formation of rope-like structures that can be identified by e.g. the helical twist (visit chapter no. I, with literature review on amyloids)[44]. The overall cross-sectional width and rigidity of the fibrils are dependent on the protofilaments number, and organization[183]. As mentioned before, for the needs of my experiments, the angular distribution of protofilaments incorporated into mature fibrils can be defined by the Θ angle, which contributes to Ψ value alongside with Ψ_0 value (expressing the deviation of the emitting species from the long axis of the protofilament). Consequently, the Ψ angle describes the conical distribution of the emission dipole of the fluorophore which corresponds to the long axis of the amyloid fibril (composed of protofilaments). Therefore, Θ, Ψ and Ψ_0 values are intertwined ($\Psi = \Psi_0 + \Theta$) and contain contributions derived from distinctive spatial scales and can describe the large variety of morphology of amyloids.

To approximate the Θ angular range, information on amyloid fibrils morphology must be retrieved. Therefore, individual insulin amyloid fibrils were grown and subsequently imaged under an atomic force microscope (see fig. no. 37), as described in the Materials and experimental methods section (Chapter III, subchapter 3.5.).

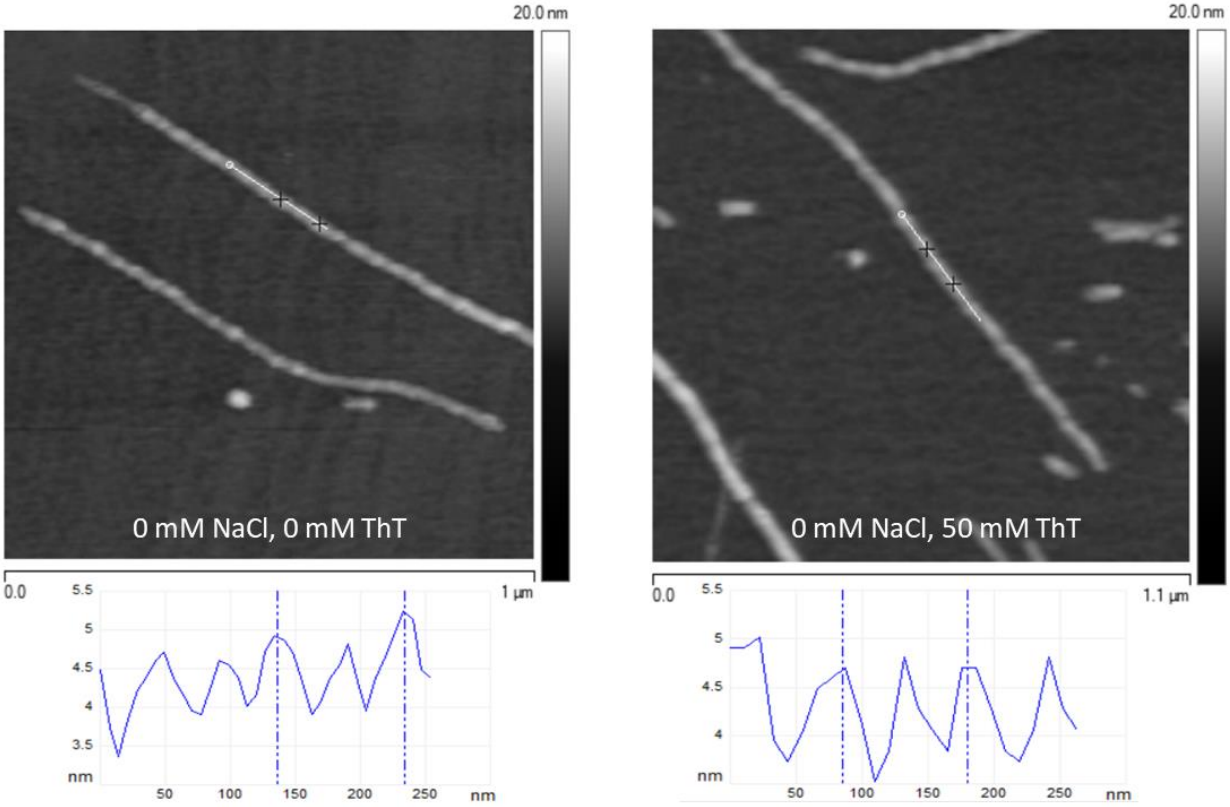

Figure 37. Amyloid fibrils morphology - AFM imaging. Exemplary AFM images of individual insulin amyloid fibrils. These fibrils were incubated in similar conditions as spherulites: stain-free (left) and ThT-labelled (right). Exemplary profiles corresponding to the twist pitch distance are presented in the lower part of the image.

Longitudinal and transverse profiles were measured from AFM images and utilized to characterize the morphological features of the individual amyloid fibrils. Moreover, to test whether ionic strength can impact amyloid fibrils morphology, a variety of incubation conditions were applied (e.g. with or without ThT, and for varying NaCl concentrations: 0, 10, 50, 100 mM). It was observed that the higher salt concentration results in the pitch distance increment. For 100 mM NaCl, amyloid aggregates tend to self-associate in structures of untwisted morphology. The aforementioned data suggest that the salt concentration may alter the angular distribution of the fluorophores (Ψ) within grown spherulites (as they might be composed of fibrils with distinctive morphologies). Overall, the samples studied under AFM were mainly characterized by a twisted ribbon conformation. The mean pitch distance was in the 85-134 nm range, while the amyloid fibrils' mean width and height were equal to 22.4 ± 5.3, and 3.8 ± 1.5 nm, respectively. Thus, with an assumption that spherulites are characterized by the same fibrillar morphology as individual fibrils obtained in similar experimental conditions, the Θ angle was determined to be in the ∼7–18° range, which corresponded well with J. Duboisset *et al.* work[56]. Consequently, the distribution angle (Ψ = 29◦) for two-photon excited autofluorescence measured from fibrils organized within a shell region of the label-free spherulites is higher than θ of individual fibrils. As a result, the Ψ_0 value must fall into the ~ 11-22◦ range. Interestingly, Saibil *et al.*[44], reported that amyloid fibrils with cross-section equal to 30 × 40 Å are composed of up to 6 – 10 protofilaments. Their geometrical arrangement allowed me to estimate the θ values, being in the 7 - 18° range, what corresponds

well with our measurements. Therefore, the presented herein technique revealed that amyloid spherulites may be composed of fibrils with similar morphology, as presented in the AFM images.

The determination of factors contributing to the autofluorescence of amyloid fibrils remains under debate. However, the photophysical mechanism of amyloid autofluorescence proposed by Grisanti *et al.*[50] corresponds well to my results, as it connects the optical phenomenon of autofluorescence with geometrical restrictions in amyloids. According to the aforementioned literature, the deplanarization of amide groups and extended carbonyl groups (i.e. structure-dependent phenomena) results in a red-shifted excitation bands of amyloid fibrils, which opens up excitation channels that may relax radially, in the form of the autofluorescence. Such phenomenon is not observed for a non-aggregated, monomeric structures. Alteration of amide and carbonyl groups geometry arise from the hydrogen bond network formed between corresponding amino acids in amyloids. Additionally, it also results in the restriction of the non-radiative decays of the entire system. Therefore, the origin of amyloid fluorescence based on cross-β structural motifs and arising from it geometrical restrictions can be also connected with the highly polarized two-photon excited autofluorescence registered from amyloid superstructures – spherulites.

5 Conclusions

I pioneeringly showed that two-photon excited amyloid autofluorescence excitation and emission are dependent on incident light polarization. Studies on the unstained amyloid superstructures performed with polarization-sensitive two-photon microscopy allowed me to determine the angular distribution of amyloid autofluorescence, being equal to 29 degrees and distributed around the fibril's long axis. Moreover, it correlated well with the control experiment, where Thioflavin-T-stained amyloids were investigated. In detail, the angular distribution of the amyloid-specific dye bound to amyloid fibrils was determined to be equal to 30 degrees. Thioflavin-T was already proven to reproduce fibrils orientation, therefore, my studies indicate that the same information can be retrieved in a label-free manner, based on the intrinsic two-photon excited autofluorescence of amyloids. The relative angle between the long amyloid fibrils' axis and two-photon excited amyloid autofluorescence transition dipole moments can be dependent on the protofibrils conformation, thus potentially detecting, and differentiating the amyloid polymorphs. My findings provide the basis for the development of new methods of amyloid imaging, without the limitations inherently coined with the staining (*i.e.* dye self-aggregation or toxicity, and influence on amyloid genesis / structure).

CHAPTER IV – Results – Amyloid spherulites: local ordering revealed by polarization analysis of two-photon excited autofluorescence

In this chapter, I utilized the polarization-dependent angular distribution of transition dipoles responsible for two-photon excited amyloid autofluorescence to resolve the local organization of amyloid fibrils in a complex and densely packed environment – within amyloid spherulites. In detail, in a label-free manner, I determined the orientation of amyloid fibrils in the spherulite's shell. I also detected the presence of the amyloid-like structures at various level of disordering in the spherulite's core. In addition, I show the comparison of two-photon excited fluorescence (2PF) profiles of labelled and label-free spherulites which supports our thesis that ThT application in the detection of distorted or amorphous amyloid intermediate fibrillar states may be limited, due to insufficient binding of ThT. The data derived from polarization-sensitive two-photon microscopy are supported by TEM imaging (transmission electron microscopy), which was also pioneeringly performed for amyloid spherulites. My work shows that the aberrations of the angular distribution of two-photon excited amyloid autofluorescence can be used to identify and distinguish between mature amyloid fibrils and amorphous aggregates or intermediate amyloid species, which may occur at different stages of the formation of the amyloid plaques.

1 Introduction: the scientific problem

Amyloidogenic proteins tend to form fibrillar structures with a characteristic motif based on cross-β organization[1], as described in chapter no. I. However, numerous structural forms of amyloid fibrils were already identified to emerge from the same repetitive building unit - polymorphs[186]. Moreover, the mechanism behind amyloid fibrils formation is still under debate[5-6]. Whilst the genesis of amyloid fibrils proceeds by the formation of distinctive forms of protein/peptide oligomers at the variety of organization states, the distorted or intermediate fibrillar structures also exert a significant influence on the process[40, 187]. Although the role of amyloid polymorphs was already linked with distinct pathologies[28, 188], their comprehensive understanding is limited due to the lack of imaging methods able to meet the requirements of clinical diagnosis[2, 8]. Furthermore, recent studies indicate that the presence of amyloid oligomers and intermediate fibrillar structures are crucial for the pre-symptomatic stage of Alzheimer's disease development, and if detected early enough, a quick diagnosis and subsequent treatment implementation could be possible[61]. Thus, the development of non-destructive, and *in vivo* suitable methods for the detection of amyloids at various stages of an organization would be beneficial.

Amyloids can also form spherical structures with diameters ranging from 5 to 150 μm – spherulites – which were previously defined[14]. As a reminder, these peculiar core-shell structures were found in the post-mortem brains of Alzheimer's, Parkinson's, and Crutzfeldt-Jackob disease patients[15]. However, to prepare a biological sample for microscopy, thin tissue sectioning is commonly performed. Therefore, amyloid spherulites can be easily omitted in *ex vivo* imaging of bio-materials, which may be the reason behind the poor description of their origin and biological importance[189]. Their complex structure with the core region that can be undoubtedly distinguished from their corona (shell) is still extensively studied, even today[190]. Nevertheless, amyloid spherulites are heterogenic in nature[20, 191], thus the complex structural description of these densely packed superstructures could contribute to a better understanding of the mechanisms behind their formation.

The remarkable progress in amyloid structural studies is achieved due to the recent developments in solid-state NMR spectroscopy and cryo-electron microscopy[188, 192]. However, the aforementioned methods are not suitable for *in vivo* experiments, thus e*x vivo* and *in vitro* amyloids are mostly studied. Two-photon fluorescence microscopy (2PFM), due to the advantages comprehensively described in chapter no. I, was proven to be crucial for bio-medical *in vivo* visualizing[144]. As already mentioned within the frames of this thesis, 2PFM has been already applied in an Alzheimer's disease mouse model imaging, where with a help of the near-infrared emitting probe deep tissue images could be visualized[145]. Additionally, the polarization analysis of transition dipole moments of the fluorophores may also report on their organization within the sample, thus revealing the structural information (see previous chapter, no III)[52]. Among others, Thioflavin-T (ThT) and Congo Red (CR) are the golden standards of amyloid imaging[37, 55]. The aforementioned molecules were already utilized as probes of the amyloid fibrils organization with a one-photon polarization-sensitive microscopy[56]. ThT and its derivatives' fluorescence tends to increase upon binding to β-sheet rich structures, due to the hindrance of the free rotation of the dye (*i.e.* blocking of the non-emissive relaxation channel). However, the binding mechanism limits the sensitivity of these

molecules for amyloids at intermediate states of aggregation, and may influence on mature amyloids structural properites[58].

To address the foregoing problems, I hypothesized that my discovery on the angular distribution of two-photon excited amyloid autofluorescence bound to the fibril's long axis can be reversibly utilized for label-free imaging of amyloid spherulites. I assumed that amyloid-distorted structures (or intermediate amyloid states) should be characterized by the higher aberrations of the aforementioned angular distribution, in comparison to the fully developed fibrils.

2 Comments and acknowledgments

Part of the data presented in this chapter is published in Obstarczyk, P.; Lipok, M.; Żak, A.; Cwynar, P.; Olesiak-Bańska, J., Amyloid fibrils in superstructures – local ordering revealed by polarization analysis of two-photon excited autofluorescence. *Biomaterials Science* **2022,** *10* (6), 1554-1561. The experimental data fit was performed with a custom-written script by M. Lipok (see Chapters II, and III). TEM imaging was performed under the supervision of A. Żak. MSc Sylwia Nowak from the Laboratory of Microscopic Techniques (Faculty of Biological Sciences) from the University of Wroclaw helped with the TEM sample preparation.

3 Materials and experimental methods

Within the frames of this chapter, the expansion of research on highly polarized two-photon excited amyloid autofluorescence is presented (namely its application in spherulites bio-imaging). Therefore, the materials and experimental methods used are matching previous descriptions. If a detailed description of any specific experiment or sample preparation protocol is needed, please revisit the previous chapters (no. II, and III). However, some changes were introduced herein, as described in the paragraphs below.

Additional chemicals: Ethanol (HPLC grade, ≥99%.), acetone (HPLC grade, ≥99%.), glutaraldehyde, osmium tetroxide, and uranyl acetate were bought from Sigma-Aldrich. Epon 812 was supplied by AgarScientific.

Assumptions for the PS-2PFM data fitting: Values of Ψ angle were set to 30° and 29° for ThT and autofluorescence, respectively. The aforementioned values were determined in the experiments performed, as described in the previous chapter (III), where the correlation of amyloid fibril's long axis and two-photon excited autofluorescence transitions dipole moment was studied.

An additional experimental method – TEM (transmission electron microscopy) - was introduced. Therefore, the corresponding sample fixation protocol was developed, as described in the following subsections (3.1, and 3.2).

3.1. Sample preparation for TEM imaging

For TEM imaging, a typical biological sample must be beforehand dehydrated, stained, and fixed. Otherwise, it would be challenging to perform imaging as bio-materials could not withstand the harsh conditions (i.e. ionizing radiation, and vacuum) within the microscope. Therefore, the as-incubated solutions containing amyloid spherulites (in 1.5 mL polypropylene Eppendorf Safe-Lock tubes) were fixed with 2% glutaraldehyde. After that, the aforementioned samples were post-fixed with 1% osmium tetroxide (~ 30 min). In the next step, the samples were dehydrated via an acetone series of up to 100% acetone. Subsequently, infiltration with 50% and 100% Epon 812 resin was performed, leading to overnight polymerization (at 60 °C). The resulting hardened resin block was trimmed to obtain 80 nm ultra-thin sections (see fig. 38). The cross-sectional cuts were deposited on clean copper grids (AgarScientific, AGG2200C), and stained with 0.5% uranyl acetate.

Figure 38. Photography of hardened resin blocks. The solutions containing spherulites were dehydrated and subsequently fixed in Epon 812 resin, directly in the Eppendorf Safe-Lock tubes – the hardened blocks are presented in the photograph. The dark areas correspond to the high concentration of osmium tetroxide (fixing and contrasting agent).

3.2. Amyloid spherulites TEM imaging

The ultra-thin cross-sectional cuts of hardened polymer containing spherulites were imaged under a light microscope. The small spherulites, with a diameter corresponding to the maximal size of copper grid windows, were found. Their structural integrity was then tested under a polarized light microscope, with crossed polarizers (see figure no. 39). The samples with a characteristic Maltese cross pattern were then imaged under TEM (Hitachi H-800). Imaging was performed under 200 kV in a thermal emission mode from a tungsten filament, and with an EMSIS QuemesaCCD camera.

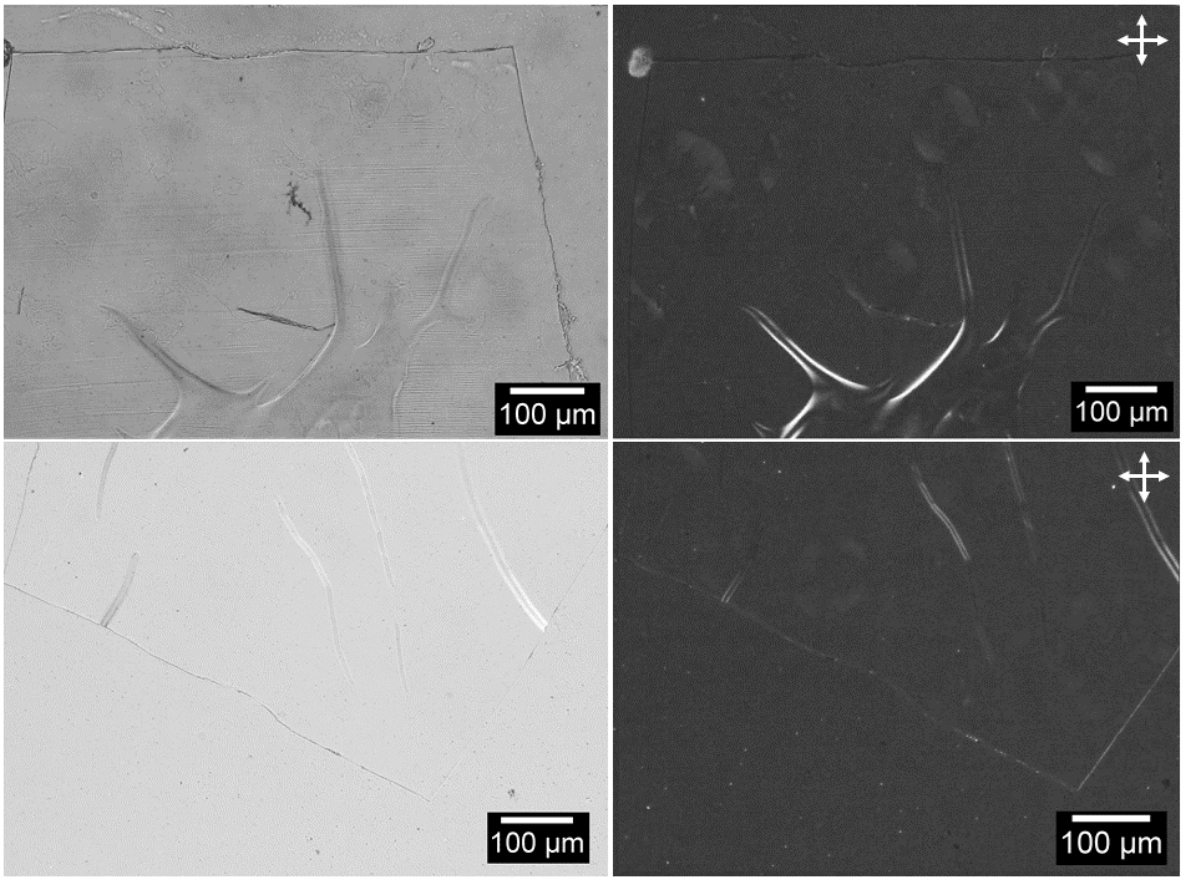

Figure 39. Light microscopy images of TEM-imaged cross-sections. Images taken with crossed polarizers are denoted with white, crossed, and double-headed arrows in the right corners.

4 Results and discussion

The experimental procedure described in the previous chapter was utilized to obtain stain-free as well as ThT-labelled amyloid spherulites from bovine insulin powder. I used polarized light microscopy with crossed polarizers and analyzed the data obtained from the spherulites imaging. I estimated that the overall size of the observed superstructures was ranging from 10 to 90 µm in diameter. In the next step, samples were imaged under a polarization-sensitive two-photon fluorescence microscope (PS-2PFM). To do that, a single spherulite was localized in the sample plane and subsequently illuminated with the incident light being horizontally and vertically polarized (relative to the XY microscope sample plane). Two-photon excited fluorescence (2PF) was split into two orthogonally (I_x, I_Y) polarized components, collected and analyzed. The detailed experimental setup description was already provided, see Chapters II, and III. As a reminder, the intensity of 2PF is expected to be highest for parallel orientation of the transition dipole moment of the fluorophore to the polarization of the incident light. Therefore, due to the photoselection phenomena, characteristic 2PF intensity distribution patterns on the raster scans (corresponding to the XY microscope plane) were expected (figure no. 40a).

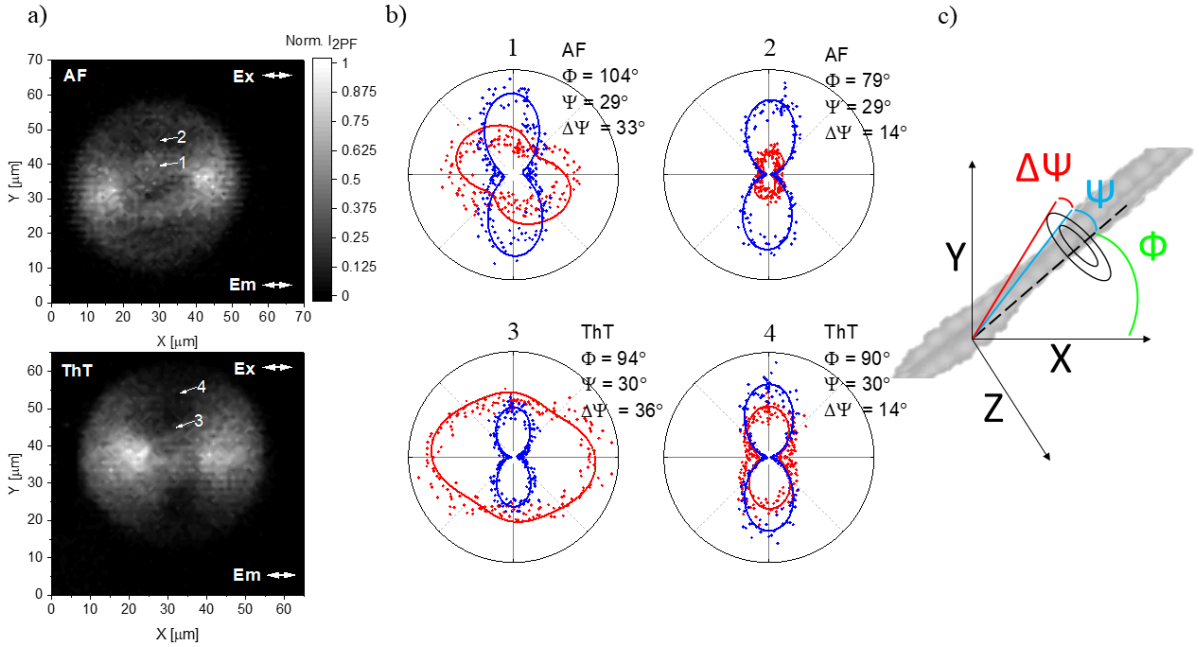

Figure 40. The raster scans of amyloid spherulites. a) Greyscale map presenting two-photon excited amyloid autofluorescence (AF) and ThT fluorescence (ThT) intensity distribution. Polarization of the excitation beam (Ex) and emission (Em) is denoted with double-headed arrows, and the excitation wavelength was set to 810 nm. (b) Exemplary polar graphs from the spots denoted on greyscale maps. Experimental datasets are presented as dots (IX and IY components are red and blue, respectively) and solid lines present the fitting of the angular dependence of the X and Y components of two-photon excited emission. (c) Schematic representation of Ψ, ΔΨ, and Φ angles in the XY microscopic sample plane. Reproduced from ref.[178] (https://doi.org/10.1039/D1BM01768C) with permission from the Royal Society of Chemistry.

Corresponding spots from the distinct areas of spherulites, as denoted on the raster scans, were chosen. Thereafter, I performed a full polarization analysis of two-photon excited fluorescence, for both label-free and ThT-labelled spherulites (see polar graphs, figure no. 40b). This procedure can be performed for any spot from the corresponding raster scans, with the sub-µm resolution. Subsequently, the collected data was fitted with functions derived from the open cone model, according to the protocol described in Chapters II, and III. In brief, the rotation of the fibrils in the XY microscope sample plane is described by the Φ angle, while the conical distribution of the emission dipole of the fluorescent individuum is denoted as half angle Ψ (fig. 40c). For the considerations presented in this chapter, the Ψ was fixed to 29° for the autofluorescence, and 30° for the ThT, with respect to the amyloid fibril's long axis, as determined in the previously described research (Chapter III). However, I hypothesized that any distortion within the amyloid fibril's structure should increase ΔΨ angle, which describes aberrations from the Ψ angle arising from the molecular rotation. Thus, by the analysis of ΔΨ values, the molecular ordering within the sample can be described.

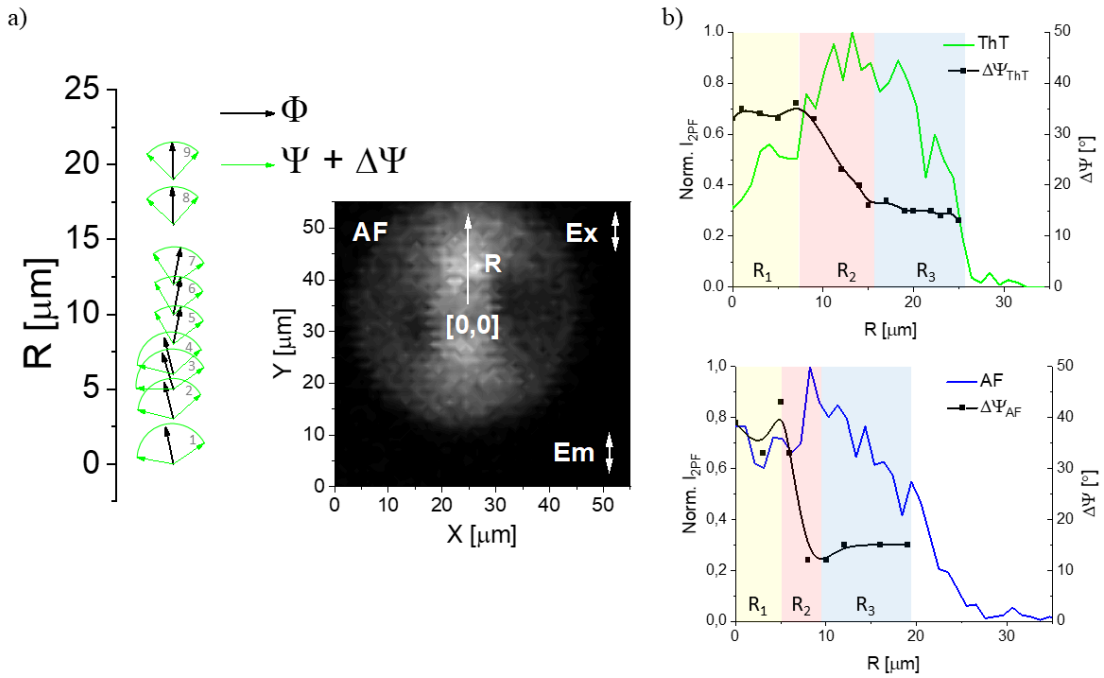

Figure 41. Structural imaging of amyloid spherulites. a) Fibrils direction on spherulite radius, marked as a single-headed white arrow - R - described by Φ angle. The radius starts from the spherulite core and ends on the structure periphery. b) Aberrations of conical distribution of the direction of emission dipole of the fluorophore – ΔΨ – correlated with spherulites radius for label-free (blue line) and ThT-labeled (green line) samples. The Ψ values are 30° and 29° for ThT and AF, respectively. Reproduced from ref.[178] (*https://doi.org/10.1039/D1BM01768C*) with permission from the Royal Society of Chemistry.

Bearing in mind the foregoing considerations, I decided to perform a full-polarization analysis from several spots located at the spherulite's radii, from its core to the corona's periphery (see figure no. 41). The same procedure was applied for the stained as well as for label-free samples. Experimental data fit revealed the fibrils' organization on the spherulite's radii in the XY microscopic plane, as depicted with the cones constructed from black and green arrows corresponding to Φ and Ψ+ΔΨ angles, respectively (figure no. 41a). These results are in a good agreement with the literature, where the radial organization of fibrils within spherulites were already prezented[14]. However, some differences in the direction (Φ) and size of the plotted cones (Ψ+ΔΨ) can be spotted, see spots no. 1-4, 5-7, and 8-9. Thus, I identified three regions of distinct organization within the studied spherulites. These regions can be allocated to the spherulite's core (cones no. 1-3), spherulite's inner (cones no. 5-7), and outer (cones no. 8-9) corona (or shell).

For a quantitative determination of the degree of order within the identified regions, I extracted the ΔΨ values from selected spots for which a full polarization analysis was performed. The resulting two-photon fluorescence intensity profile across the spherulite's radii, with spatially corresponding ΔΨ values (for label-free and ThT-stained samples, respectively) are presented in figure no. 41b. For both cases, three distinct regions can be defined, based on 2PF intensity profiles and sigmoidal plots of ΔΨ values, namely: R_1 (core), R_2 (inner corona), and R_3 (outer corona). The aforementioned regions were marked in figure 40b with yellow, red, and blue shading, respectively. The degree of fibrils organization should

be inversely proportional to ΔΨ value, which, indeed, tends to decrease radially from the spherulites' core to the periphery. Therefore, I show that amyloid spherulite's core is unorganized, in contrast to highly organized peripheral regions. The corresponding Ψ+ΔΨ average values in R_1 are equal to 70° and 64.5° for two-photon excited amyloid autofluorescence (2PAF), and ThT two-photon excited emission (ThT 2PF), respectively. For R_2 and R_3 regions, however, higher ordering was observed, as Ψ+ΔΨ values are equal to 51.5° and 53° for TPAF and ThT 2PF, respectively. In both cases, the sigmoidal shape of ΔΨ plots reveals the complex structural features of amyloid spherulites, however for 2PAF the slope corresponding to R_1-R_2 transition region is characterized by a higher inclination, in comparison to ThT 2PF. Overall, with PS-2PFM, I depicted amyloid spherulites to be composed of an unorganized core (R_1), highly organized fibrils in the outer corona (R_3), and transitioning region (R_2), *i.e.* the inner corona, where intermediate amyloid aggregates as well at fibrils at various states organization may be present.

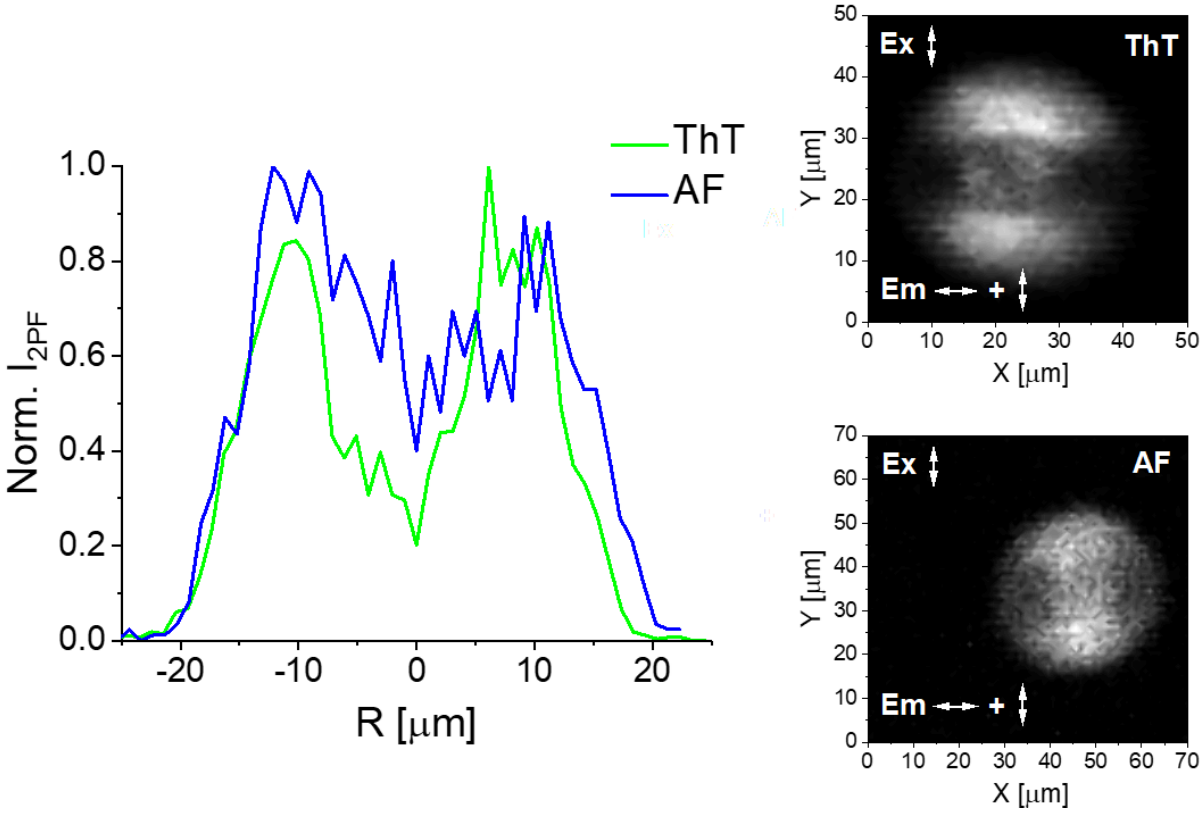

Figure 42. Two-photon excited fluorescence intensity profiles. Correspondingly, label-free (blue line) and ThT-labeled (green line) pair of spherulites. Horizontal axis - R - corresponds to the spherulite radius starting from the structures' center to the periphery. Insets present 2PF intensity raster scans as a sum of horizontally and vertically polarized emission components. Reproduced from ref.[178] (*https://doi.org/10.1039/D1BM01768C*) with permission from the Royal Society of Chemistry.

As already mentioned, Thioflavin-T is amyloid-specific and binds perpendicularly to β-strands of mature amyloid fibrils, therefore is parallelly oriented to the fibril's long axis[52, 60]. However, despite its remarkable properties, the ThT dye sensitivity for amyloid oligomers or intermediate forms is limited as at the aforementioned amyloid aggregation states, the binding sites are not fully developed for molecular docking to occur[55]. Therefore, two-photon excited

emission from ThT molecules within the amyloid spherulites' core, derived from mature fibrils, is expected to be strongly mitigated. Bearing that in mind, I plotted the ThT 2PF as well as TPAF intensity profiles from the corresponding raster stans (see figure no. 42). Interestingly, the relatively strong signal from TPAF could be collected also from the spherulite's core, which raise a question about the origin of this phenomenon. In detail, for the ThT-labeled sample, two-photon excited fluorescence is decreasing by approximately 80 % near the spherulite's core. However, for the autofluorescence, the corresponding intensity drop reached only 60 %. The amyloid spherulites' formation mechanism is associated with the protein/peptides misfolding and self-assembly into amorphous aggregates that function as a nucleus for radial growth, or with the collapse, merge, and disorganization of already existing fibrils[14]. Therefore, as disorganized fibrils could be present in the core, two-photon excited autofluorescence detected in the corresponding region could be originating from them[48]. Alternatively, the strong TPAF signal can originate from the oligomeric species or intermediate forms of fibrils[193]. Moreover, the collapse of mature fibrils theory correlates well with the high decrease in ThT two-photon excited fluorescence intensity near the spherulite's core, as binding sites are expected to also be distorted[57].

To test my hypothesis, I decided to perform additional imaging, under TEM (see the Materials and experimental methods section (Chapter IV, subchapter 3.1.)). However, I do not treat the TEM images quantitatively, and this approach is consistent with the art of ultrathin sections biological imaging. I would like to emphasize the fact that even though the presented herein methodology is based on established protocols of biological sample fixation and preparation for electron microscopy, it was pioneeringly applied in the structural studies on amyloid superstructures, *i.e.* insulin spherulites.

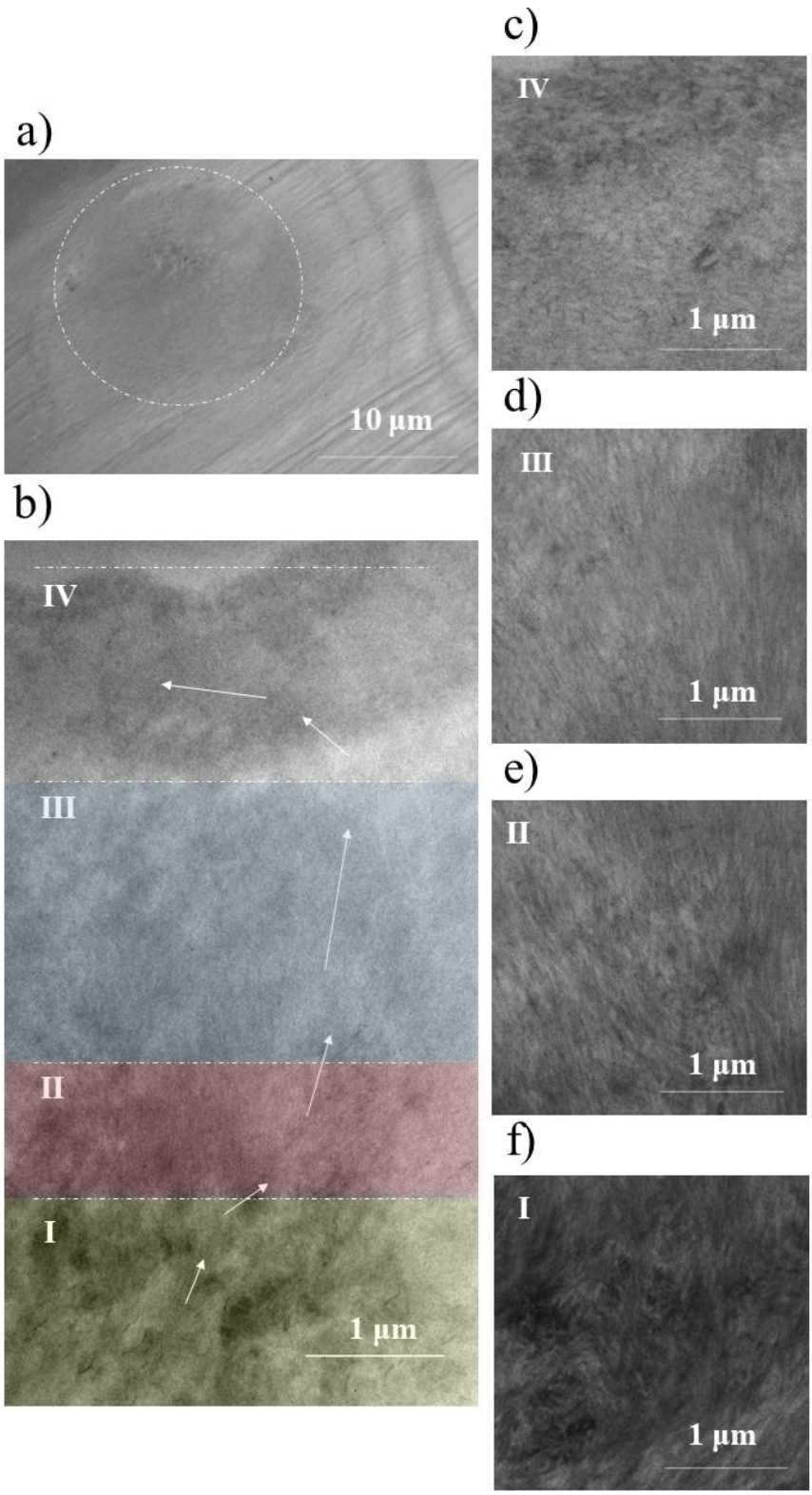

Figure 43. Amyloid spherulites TEM imaging. a) TEM macroscopic view of spherulite in the central cross-section. (b) Cross-section fragment with an example of a fibrils course (arrows) and characteristic elements of the structure: I – densely packed core consisting of a micrometric width of bundles of tangled fibrils and intermediate states, II – tightly packed area of tangled fibrils , III – loosely packed area of fibrils, IV – shell forming fibrils. Magnified view of c) IV, d) III, e) II, f) I regions. Reproduced from ref.[178] (*https://doi.org/10.1039/D1BM01768C*) with permission from the Royal Society of Chemistry.

As viewed at low magnifications, the outer boundary of the spherulite cannot be undoubtedly distinguishable from the background (figure no. 43a) . However, by increasing the magnification, a detailed depiction of the entire ultrastructure became possible (as shown in Figure no. 43b). The ultimate quantification of the directionality in each area of TEM images is challenging due to the molecular crowding and distribution of the contrasting agents, especially for densely packed core where numerous structures are intercrossed or too short to properly measure the angles. Therefore, individual fibril orientation in highly packed and distorted regions cannot be unambiguously determined. However, the general orientation (see white arrows in figure no. 43b) could be estimated from every part of TEM image. After careful image analysis, four distinct regions with characteristic and distinct structural elements could be identified, as marked with I - IV in figure no. 43 (c-f, respectively).

The core region (I) is densely packed, and composed of entangled and disordered fibril-like structures, which are arranged in micrometric-wide and parallelly oriented strands. In addition, non-fibrillar structures (e.g. amorphous aggregates) are also visible, as highly contrasted. Additionally, A. M. Donald's group showed by the correlation of optical microscopy with Raman scattering spectroscopy that the content of β-sheets across the spherulite radii is varying from 75% to 60%, from edge to core, respectively[185]. They also stated that the corresponding random coils content is within the 15 – 25% range, while the remaining percent were assigned to α-helix rich structures. The significant percentage of β-sheets in the spherulite core corresponds well to the fibril-like structures detected under TEM for the corresponding region in my studies. Therefore, if compared to the data from PS-2PFM (i.e. R_1 region), the high two-photon excited autofluorescence registered within this part of the superstructure may indeed originate from these intermediate amyloid states, which simultaneously explains the high drop of ThT two-photon excited emission, if distorted nature of the spherulite's core is considered[60]. Additionally, the distinct values of ΔΨ within the core can be assigned to the amorphous structures or amyloid intermediate states, thus PS-2PFM and two-photon excited amyloid autofluorescence might be utilized to detect amyloids at various states of aggregation.

As moving outward, the fibril-like structures are still densely packed but tends to form radial and partially tangled structure (II), which gradually transition to the region with loosely packed and more organized fibrillar structures (III). These TEM-derived observations correspond well to the data obtained from PS-2PFM, where two distinctive regions, namely the R_2 and R_3, were detected and differentiated by a slight difference in fibrils orientation (Φ angle) as well as in corresponding ΔΨ values. In detail, area no. II (derived from TEM image) is simultaneously more densely packed and distorted in comparison to area no. III, which corresponds to the PS-2PFM R_2 region with higher ΔΨ values, and R_3 region with lower ΔΨ values, respectively. However, the observed herein raise of organization degree between the spherulite's inner and outer corona raise a question about its overall formation mechanism. According to Rogers *et al*.[184], the space in the spherulites' corona can be composed of branched structures, to contain the constant density over the entire structure. However, according to measurements performed herein, no branching was observed *via* TEM or PS-2PFM. Therefore, I hypothesize that secondary nucleation between already grown fibrils during the spherulite's inner corona growth may occur. The colinear growth of fibrils, between

initially formed ones, or de novo nucleation from intermediate states could explain the observed ΔΨ changes between the spherulite's inner, and outer corona, as well as differences in packing density and ordering between regions no. II, and III, as imaged under TEM.

The last distinctive regions observed under TEM (no. IV) consist of the 1.5 µm thick border between the external environment and the superstructure itself. In the spherulite's outer region fibrils are densely packed, and bend by 45°. This particular region cannot be matched with results from PS-2PFM. However, I hypothesized that the formation of additional shell observed under TEM is caused by the sample preparation method, which includes dehydration. The removal of water *via* acetone series can force the free fibrils from the native aqueous solution to coalesce on big, and spherical aggregates (spherulites). I support my hypothesis by the fact, that the bend fibrils should be easily detected by varying polarization of the incident light under PS-2PFM. Therefore, spherulites in the hydrated environment are devoid of the additional shell. I hypothesize that shell observed under TEM is forming due to the dehydration, as free fibrils floating in the solution are coalescing onto superstructures.

5 Conclusions

I demonstrated that analysis of polarization-sensitive two-photon excited amyloid autofluorescence can be utilized to resolve the orientation of amyloid fibrils on a sub-micron scale. My results are in good agreement with recent research on amyloid spherulites organization, indicating that a single spherulite can be highly heterogeneous. I observed the distinctive structural components gradually changing across spherulites' radius. Moreover, TEM imaging pioneeringly performed on spherulites was consistent with PS-TPM investigations. Presented herein results contribute to a better understanding of spherulites' structure and formation mechanisms.

I indicated that the conical distribution aberration of the two-photon excited autofluorescence emission dipoles can report on amyloid fibrils' ordering, distortions, and structural polymorphism. Therefore, these findings allow fora better understanding of the intrinsic nonlinear optical properties of amyloid aggregates. Presented herein technique is promising for differentiating between a variety of amyloid-like structures, which may be useful for the fast detection of amyloid intermediates being preset at the early stages of plaque formation.

I compared the two-photon excited emission intensity from ThT-labeled and label-free spherulites and revealed that the spherulites' cores have low ThT fluorescence, while a significant autofluorescence signal could be still collected. By doing that I indicated that two-photon excited amyloid autofluorescence can be also collected from distorted amyloid fibrils or intermediate amyloid states, which cannot be successfully stained with the ThT dye. Therefore, my stain-free method is not limited by the dye affinity or accessibility to the binding sites. It might be beneficial for a better understanding of diverse aggregation pathways available for a variety of amyloidogenic proteins and peptides.

CHAPTER V – Results – Multimodal imaging with gold nanoclusters

In this chapter, I present the synthesis protocol, basic physicochemical characterization, and initial application (in amyloid multimodal imaging) of 12-crown-4-SH-capped gold nanoclusters (GNCs). My GNCs design allowed for the translation of macrocyclic supramolecular ligand's amphiphilic properties onto ultra-small nanoparticles (~1.7 nm). I confirmed the amphiphilic properties of GNCs by phase-transfer experiments, where clusters spontaneously transferred from aqueous to organic solvent. I utilized the aforementioned property (as well as GNCs' high electron density and NIR fluorescence) for bio-imaging of insulin amyloid fibrils and spherulites at micro- and nano-scale, with fluorescence and electron microscopy, respectively. Additionally, I probed GNCs hydrophilic (glutathione) and amphiphilic (12-crown-4-SH) ligands influence on binding affinity to amyloid spherulites, in a time-resolved manner. My TEM images analysis, supported by data available in the literature, indicated that 12-crown-4-SH capped GNCs may preferentially bind to hydrophobic domains of amyloid fibrils, used as a bio-interface model. Overall, I showed that crown ether stabilized GNCs may be a versatile tool for cost-effective cross-platform imaging as they reveal structural features of amyloid aggregates under fluorescence and electron microscope.

1 Introduction: the scientific problem

In biology, the interlinkage of numerous non-covalent inter/intramolecular interactions (e.g. hydrogen bonding, electrostatic interactions and hydration) plays a crucial role in various physiological processes, including membrane fusion, or enzymatic activity[142, 194]. Interestingly, it is, among others, the surface hydrophobicity that drives the protein folding mechanisms, which ultimately dictates their biological functionality[45, 195]. Therefore, it is important to be able to cost-effectively visualize both hydrophilic and hydrophobic bio-interfaces[111]. Although there is a significant demand for smart probes being sensitive to the polarity of bio-molecules, most of them rely on advanced chemical processing, they are target specific (thus not versatile), and their hydrophobicity cannot be easily adjusted[129]. Moreover, a perfect marker should exhibit some kind of adjustable response to the chosen environmental factor, be adaptable for staining various types of samples and be simultaneously suitable for multimodal imaging to reveal as much structural information as possible[196]. Fluorescent imaging has become a popular research tool in biomedical science due to its sensitivity, spatial and temporal resolution, and non-invasiveness. However, for *in vivo* studies, fluorescent probes should emit in the optical window range of wavelengths (700-1000 nm, NIR-1)[128] to achieve a decent tissue penetration coefficient, as thoroughly discussed in the previous chapters[197]. Most reported probes are based on simple organic dyes (SOD)[198] what shows several limitations. SOD are usually characterized by a lack of optimal selectivity to polarity and moderate physicochemical merits (*i.e.* solubility, Stokes shift, quantum yield, and photostability). Additionally, for multi-photon microscopy, the design of the dye is commonly based on prolonged π conjugated systems, as it is a strategy to achieve high optical merits (as described in this thesis introduction section)[147]. In consequence, the binding affinity to bio-interfaces or solubility in specific solvents may be limited. Moreover, due to the low electron density, SOD cannot be successfully applied in TEM imaging, thus additional staining (e.g. with uranyl acetate for proteins[199]) is necessary. Alternatively, for organic dyes, to achieve satisfying contrasting properties in electron imaging, it its necessary to perform a functionalization with heavy elements that may ultimately alter probe sensitivity for binding sites. Therefore, a functional probe (sensitive for hydrophobic domains) being inherently suitable for fluorescence and electron microscopy would be beneficial to conceptualize.

To ameliorate the understanding of the intricate organization of bio-structures, there is a growing need for simultaneous examination of the same sample at different scales, and modalities[64, 200]. The use of CLEM (correlative light and electron microscopy (EM)) is highly advantageous as it combines information obtained from functional fluorescent labeling (fluorescence microscopy - FM) with high-resolution contextual information derived from electron microscopy[73]. The suggested strategy allows researchers to link three distinct types of data, namely morphological, functional(FM) and ultrastructural (EM), from the same area of interest. Usually, CLEM is performed with aligned systems where samples embodied in resin (to withstand harsh conditions under an electron microscope) are investigated. However, herein, multimodality and CLEM are understood as a subsequent application of both microscopic techniques for samples stained with the same functional marker. Moreover, the application of nanomaterials in multimodal imaging for structural biology is still rare, mostly

because of limited access to consistent sample preparation protocols as well as due to the moderate availability of universal nano-staining agents.

Gold nanoclusters (GNCs) are a class of ultrasmall (less than 2 nm in diameter) and usually thiol-protected gold nanoparticles that have become increasingly popular in the last decade due to their robust luminescent properties, low toxicity, and tunable chemical and optical properties[94], as comprehensively described in the previous chapter. They are characterized by tunable photoluminescence, large Stokes shifts, high electron density, and high photostability. Moreover, the molecule-like UV-VIS spectral properties of GNCs are easily tuned by modification of the cluster core composition and protecting ligand type[88]. Thus, their physicochemical properties can be also tailored, solely by the surface ligand functionality, which may help to control the efficiency of binding to biological materials[201-202]. Therefore, due to their superior physicochemical properties, when compared to SOD, they are a promising candidate for a multimodal imaging probe (especially for fluorescence and electron correlated imaging). In state-of-the-art research, GNCs functionalized with fluorescent dye have been used to visualize hydrophobic pockets of selected enteroviruses and protein structures[118]. Although GNCs with more than 100 gold atoms are characterized by a high electron density resulting in excellent TEM contrasting properties, they generally do not exhibit luminescence. Therefore, for multimodal imaging, GNCs need to be beforehand functionalized with fluorescent molecules or size-adjusted to open up emissive relaxation channels. Moreover, it would be beneficial if their protecting ligand could introduce additional functionality. Among numerous possible ligands, crown ethers possess extraordinary properties (as described in introduction section)[154]. Among others, due to the macrocyclic molecular architecture based on ethylene oxide, crown ethers are amphiphilic and prone to selectively interact with cations *via* non-covalent interactions[159]. Moreover, as plasmonic nanoparticles were already functionalized by crown ethers and exhibited amphiphilic properties[203-204], I decided to design inherently fluorescent, electron-rich, and amphiphilic nano-probes with molecule-like properties for bio-imaging.

2 Comment and acknowledgements

Part of the data presented in this subchapter is published in Obstarczyk, P.; Pniakowska, A.; Nonappa; Grzelczak, M. P.; Olesiak-Bańska, J., Crown Ether-Capped Gold Nanoclusters as a Multimodal Platform for Bioimaging. *ACS Omega* **2023,** *8* (12), 11503-11511. TEM imaging of amyloid fibrils was performed at Tampere University (Tampere, Finland) under the Photonics Research and Innovation (PREIN) and Tampere Microscopy Center facilities flagship. Sample preparation and imaging were performed under the supervision of Professor Nonappa, during my internship financed by the Erasmus+ program. TEM imaging of gold nanoclusters was performed due to courtesy of the Hirszfeld Institute of Immunology and Experimental Therapy - Polish Academy of Sciences (Poland, Wrocław).

3 Materials and experimental methods

3.1. Chemicals

All chemicals were used as purchased, without further purification. Gold(III) chloride trihydrate ($HAuCl_4 \times 3H_2O$, ≥ 99.9% trace metals basis), sodium borohydride ($NaBH_4$, ≥ 98.0%), hydrochloric acid (HCl, 37%, ACS reagent), insulin from bovine pancreas (≥25 units/mg (HPLC), I5500), Styryl 9 M (dye content of ∼96%), l-glutathione (reduced (GSH) ≥ 98.0%), sodium cyanoborohydride ($NaBH_3CN$, 95%) were purchased from Sigma-Aldrich, in powder form. Mili-Q quality water (resistivity: 18.2 MΩ·cm @ 25 °C) was used throughout all the experiments. Organic solvents, *i.e.* methanol (CH_3OH, suitable for HPLC, ≥99.9%), hexane ($CH_3(CH_2)_4CH_3$, suitable for HPLC, ≥95%), isopropanol ($(CH_3)_2CHOH$, suitable for HPLC, 99.9%), diethyl ether ($(CH_3CH_2)_2O$, contains 1 ppm BHT as an inhibitor, anhydrous, ≥99.7%), and chloroform (CH_3Cl, suitable for HPLC, ≥99.8%, containing 0.5–1.0% ethanol as a stabilizer) were also purchased from Sigma-Aldrich. Stabilizing ligand - 2-(Mercaptomethyl)-12-crown-4 (12-crown-4-SH, for short) - was purchased from Prochimia Surfaces.

3.2. Gold nanoclusters synthesis: 12-crown-4 ligand

To synthesize ultra-small (~ 1.7 nm) GNCs stabilized with 12-crown-4-SH ligand I adapted the protocol preparation for the synthesis of plasmonic nanoparticles stabilized with 18-crown-6-SH, described by Grzelczak et al.[204]. However, some changes (beside crown ether macrocyclic ring size) were introduced. In the first step, a mixture of $HAuCl_4$ and 12-crown-4-SH with a 1:3 molar ratio was prepared by mixing (1000 rpm) methanolic solutions of 2.5 mL of 3 mM gold (III) chloride trihydrate with 2.5 mL of 9 mM solution of 12-crown-4-SH. The reaction was carried out in a 20 mL scintillator vial (27.3 x 60 mm, BIONOVO), for approximately 1h at 0 °C. Then, freshly prepared and ice-cold $NaBH_4$ methanolic solution was rapidly injected into the aforementioned mixture. After that, the solution was left gently stirred (200 rpm) for approximately 1h (till complete $NaBH_4$ hydrolysis). In the next step, the resulting 12-crown-4-capped gold nanoparticles solution was poured into a 50 mL round-bottom flask (with additional methanol washing) and rotary-evaporated (30° C) to dryness. The remaining powder was washed multiple times with 30 mL of hexane, dried, and subsequently washed with the consequent amount of diethyl ether. When diethyl ether evaporated completely, the dry residue was dispersed in 5 mL of isopropanol and filtered off through a 0.22µm pore size Millex-GP PES Millipore Express membrane syringe filter. The resulting solution was again rotary evaporated at 30 °C. The dried and purified residue was dispersed in 10 mL of Mili-Q water (12-crown-4-SH capped GNCs stock solution).

3.3. Gold nanoclusters synthesis: glutathione ligand

To synthesize gold nanoclusters stabilized with hydrophilic ligand, namely glutathione, the combination of several available protocols was utilized[202, 205-206]. In brief, 1.2 mL of the 1:1

methanol to water solution was prepared in a 20 mL round-bottom flask. In the following step, 150 mg of glutathione powder was added and rapidly (1200 rpm) stirred. After that, a 0.3 mL aliquot of 0.636 M $HAuCl_4$ x $3H_2O$ (aqueous solution) was pipetted into the flask and left until the solution became colorless. Subsequently, the reaction mixture was diluted to the total volume of 15 mL with methanol. The gold-thiol polymers were reduced by a drop-wise addition of $NaBH_3CN$ (220 mM, 2.25 mL). After 4 hours from the last portion of the reducing agent, the precipitate formed. The supernatant was removed and the remaining product was thoroughly washed with methanol, three times fold. The product was rotary-evaporated (30 °C), and the resulting purified dry residue (reddish powder) was dispersed in 2 mL of Mili-Q water ($Au_{18}(SG)_{14}$ stock solution).

3.4. Gold nanoclusters phase transfer: preferential solvent and process reversibility

To test GNCs amphiphilicity, a 1 mL aliquot of corresponding GNCs stock solutions (12-crown-4 and glutathione-capped) was mixed (by hand) with the corresponding volume of chosen organic solvent (*i.e.* chloroform). After that, the vials were left undisturbed for 6h (loosely capped). Then, the phases were separated. A reversible process is not possible, however, after chloroform evaporation (e.g. *via* rotary evaporation), the remaining residue could be successfully redispersed in water. Thus, a full cycle of aqueous to organic and back phase transfers was tested with UV-Vis spectroscopy.

3.5. Amyloid incubation: fibrils and spherulites

To prepare the bio-interface model – amyloid fibrils – 10 mg of bovine insulin powder was dissolved in 1 mL of Mili-Q water/HCl mixture (pH 2). In the following step, the solution was incubated in an Eppendorf Thermomixer C (70 °C, 700 rpm, 24h). To obtain amyloid superstructures (spherulites), the same procedure was applied, with a slight modification, namely no mixing. The aforementioned processes were conducted in 1.5 mL Eppendorf Safe-Lock Tubes (polypropylene) sealed thoroughly with PTFE thread seal tape (12 mm x 12 mm x 0.1 mm, 60 gm^2). For the need of experiments, the as-incubated amyloid fibrils and spherulite solutions were diluted with Mili-Q water from 10 mg/mL to the final concentration of 0.05 and 0.5 mg/mL, respectively.

3.6. UV-Vis and FT-IR spectroscopy

The UV-Vis spectra as well as the fluorescence measurements of all GNCs solutions (both, in aqueous and organic solvents) were registered in a QS high-precision cell (10 mm optical length, Hellma Analytics) with JASCO V-670 spectrometer and Edinburgh Instruments FLS100 spectrofluorometer (excitation wavelength: 450 nm). Fluorescence quantum yields (QY) were calculated by indirect method, with styryl 9M used as the reference [207] :

$$\xi s = \xi r \frac{\zeta_r(\lambda_{ex})}{\zeta_s(\lambda_{ex})} \frac{\int_{\lambda_{em}} Q^s(\lambda_{em})}{\int_{\lambda_{em}} Q^r(\lambda_{em})} \frac{n_s^2}{n_r^2} \quad (1)$$

$$f_x(\lambda_{ex}) = 1 - 10^{-A_x(\lambda_{ex})} \quad (2)$$

Where: ξ_s and ξ_r – sample (s) and reference (r) fluorescence quantum yields; $Q^s(\lambda_{em})$ and $Q^r(\lambda_{em})$ - fluorescence integral of sample and reference; n_s and n_r - refractive indices of sample and reference; $A_x(\lambda_{ex})$ – corresponding absorbance at excitation wavelength; $\zeta_x(\lambda_{ex})$ – corresponding absorption factor at the excitation wavelength.

Corresponding FT-IR spectra were recorded with Bruker Optic GmbH: Vertex 70v FT-IR spectrometer.

3.7. **Multimodal imaging**

To investigate the 12-crown-4-SH capped GNCs utility in bio-imaging I performed the multimodal imaging of GNCs-labelled and label-free amyloids with atomic force (AFM), transmission electron (TEM), photoluminescence, bright-field, and polarized-light microscopy. Sample preparation protocols, as well as technical details regarding enlisted techniques, are described in the following paragraphs.

Atomic force microscopy (AFM): Typically, a 100 µL aliquot of amyloid stock solution (0.05 mg per mL) was mixed with the corresponding volume of 12-crown-4-SH capped GNCs stock solution (or Mili-Q water, for a label-free sample) and left undisturbed to let GNCs diffuse onto bio-surfaces (in 5 °C, for 6h). In the next step, a 100 µL aliquot of the aged solution was pipetted onto the mica surface (15 mm x 15 mm, V-1 Quality, Sigma-Aldrich) and left for 1 minute to allow the sedimentation. After that, the mica surface was washed with 5 mL of Mili-Q water and left to dry under ambient conditions. The remaining dry samples were imaged. AFM images were obtained using a Dimension V Veeco AFM instrument (in the tapping mode) and analyzed with the Nanoscope 7.30 software.

Transmission electron microscopy (TEM): The stock solution of amyloid fibrils stained with 12-crown-4-SH GNCs (as well as the label-free sample) was prepared in the same manner, as described above (in the AFM sample preparation description). In the next step, the aforementioned solution was gently stirred by hand. Subsequently, a 10 µL aliquot was taken and pipetted onto the copper grid with carbon-only support film (AgarScientific, AGG2200). Before the deposition of the aged solution, the copper grids were plasma-cleaned (EMITECH, K1050X). Samples were left undisturbed for 5 min, for fibrils to sediment. After that, to prevent a thick film formation, the copper grids were picked up and subsequently dipped into 2 mL of water and methanol (Eppendorf Safe-Lock Tubes). In the last step, all samples were left to dry under ambient conditions. TEM images were obtained using a JEOL F200 S/TEM microscope with an accelerating voltage of 200 kV. Gold nanoclusters (as-synthesized) were simply drop-casted on copper grids (AgarScientific, AGG2200), left to dry and subsequently imaged under JEOL JEM F-200 microscope (accelerating voltage 150 kV).

Fluorescence, bright field, and polarized-light microscopy: All images were taken under an Olympus BX60 optical microscope, using an Olympus UPlanFLN 20x/0.5 NA objective. Fluorescence imaging was performed for the excitation wavelength set in the 460 – 495 nm range, in a wide-field epifluorescence mode. To perform polarized-light microscopy imaging, the aforementioned microscopy setup was additionally equipped with two orthogonally crossed polarizers (allocated between the sample plane). In detail, a 50 µL aliquot of amyloid spherulites stock solution was pipetted onto a microscope slide with a single well (Super White Glass, 76 x 26 x 1 mm, CHEMLAND) and imaged in a bright field and polarized-light modes. After that, 50 µL of the GNCs stock solution (either $Au_{18}(SG)_{14}$ or 12-crown-4-SH capped ones) was added. Subsequently, the microscopic samples were covered with a coverslip. Immediately after, imaging in fluorescence mode was performed. To exclude diffusion, images were taken in the 30 min timescale (15 min intervals, t = 0, 15, 30 min).

4 Results and discussion

According to my hypothesis, 2-(mercapto methyl)-12-crown-4 ether can be utilized as a stabilizing and simultaneously functional (amphiphilic) agent for the synthesis of ultra-small nanoclusters, with sizes nearly *Fermi's* wavelength of *gold* (approx. 0.5 nm). Moreover, by the adjustments of the GNCs core size, the photoluminescence in the NIR-I region can be achieved[94]. I selected 12-crown-4 ether as stabilizing ligand intentionally, as it is characterized by the cavity size suitable to preferentially interact with Li^+ cations. Therefore, its potential influence on the physiological hemostasis in living organisms (driven by Ca^{2+}, K^+, and Na^+ cation distribution) is limited, in comparison to bigger ethylene oxide macrocyclic compounds[156, 208]. Importantly, the 12-crown-4 ether was proven to cross the blood-brain barrier, and non-covalently interact with charged amino acids and hydrogen bond networks that are crucial for amyloid formation (e.g. amyloid-β (Aβ))[169, 209]. Herein, in figure no. 44, I present a schematic architecture, as well as conceptual functionality of 12-crown-4 ether-capped GNCs.

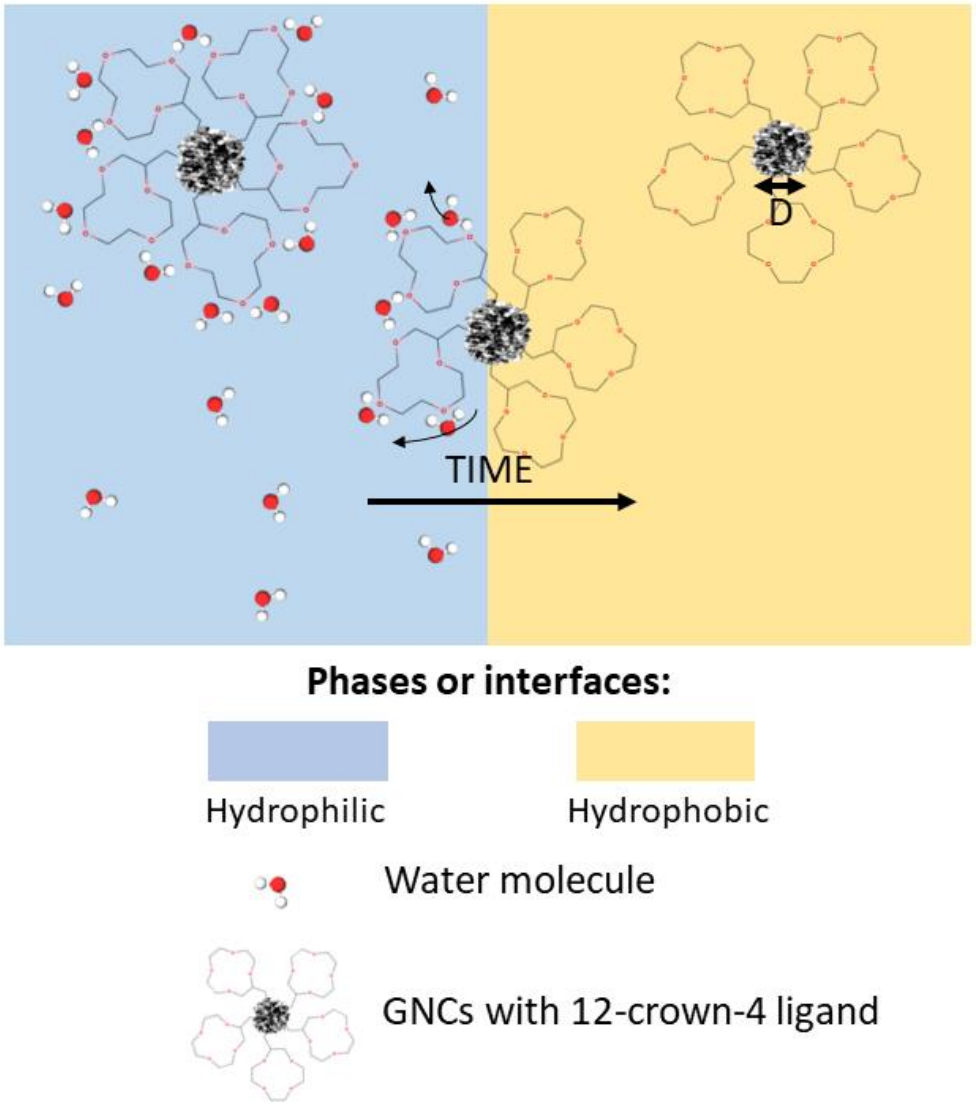

Figure 44. Schematic representation of GNCs capped with a 12-crown-4 ether and its amphiphilic properties, namely phase transfer from a hydrophilic to hydrophobic medium. Water molecules that are solvating the crown ether ligands are released on contact with the hydrophobic phase or interface. The clusters' core (with diameter, marked with "D", in size range approximate to the Fermi's *wavelength of* gold), water molecules, and ligand sizes are not proportional to real equivalents. Potential crown ether conformational changes upon interaction with protic (aqueous) and aprotic solvents are also schematically depicted. Adapted from reference no.[210] (*https://doi.org/10.1021/acsomega.3c00426*), Copyright © 2023 Patryk Obstarczyk *et al.*, Published by American Chemical Society.

Based on the modified procedure proposed by Grzelczak *et al.*[204], as comprehensively described in the Materials and experimental methods section (Chapter V, subchapter 3.2.), I successfully synthesized 12-crown-4 ether-capped ultra-small nanoparticles. In brief, a reducing agent was added to the methanolic solution containing gold salt and thiolate, co-dissolved with a 1:3 molar ratio. The resulting solution was purified and dried. To test if the products of my synthesis inherited the amphiphilic properties from the supramolecular ligand I decided to dissolve it in water and chloroform ($CHCl_3$). Therefore, the product of my synthesis was split into two halves and respectively dispersed in the corresponding volumes of H_2O, and

$CHCl_3$. The powder could be effortlessly dissolved in both solvents, thus clusters' amphiphilicity was confirmed. The as-prepared GNCs solutions, in water and chloroform (from now on denoted as Aq-GNCs and Ch-GNCs, respectively) were further characterized with a UV-Vis spectroscopy, as presented in figure no. 45, a.

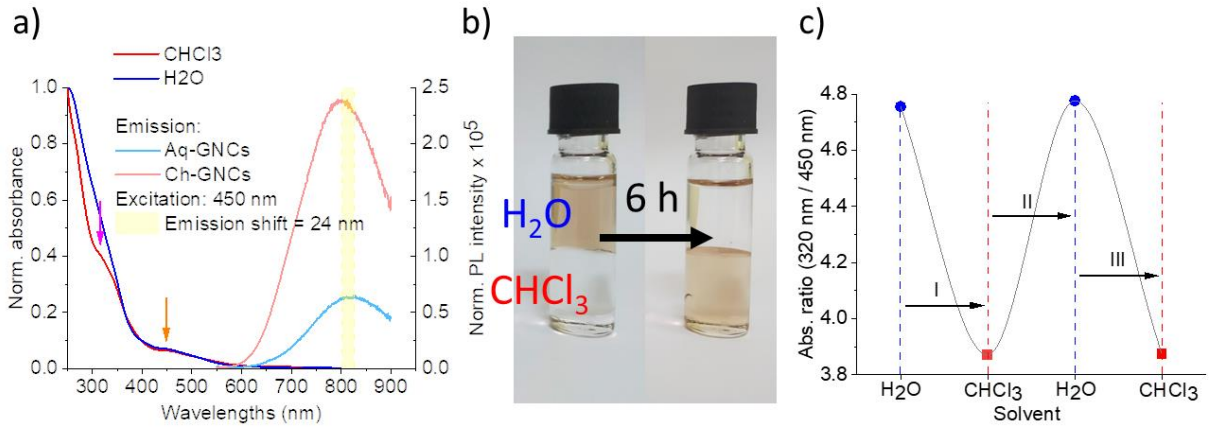

Figure 45. UV-Vis characterization of amphiphilic GNCs. a) Normalized absorption and emission (divided by corresponding absorbances at the excitation wavelength, i.e., 450 nm) of Aq-GNCs (blue lines) and Ch-GNCs (red lines). Magenta and orange arrows indicate distinctive bands at 320 and 450, respectively. b) The photographs of vials before and after phase transfer from the aqueous phase to the organic phase (water to chloroform) for GNCs capped with a 12-crown-4 ether ligand. Photos were taken within a 6 h time interval. c) Reversibility of the phase transfer process monitored by the sample absorbance ratio (Abs at 320 nm/Abs at 450 nm) measured alternately in a protic and aprotic solvent (from H_2O to $CHCl_3$ (I), *vice versa* (II) and to $CHCl_3$ again (III). Adapted from reference no.[210] (https://doi.org/10.1021/acsomega.3c00426), Copyright © 2023 Patryk Obstarczyk *et al.*, Published by American Chemical Society.

Both, the aqueous and organic solutions are characterized by the discrete and simultaneously similar absorption spectra with a common band at 450 nm (orange arrow). In both cases, there are no bands characteristic of plasmonic nanoparticles, therefore formation of nanoclusters is confirmed. Interestingly, GNCs in chloroform (aprotic solvent) are characterized by an additional band at 320 (magenta arrow), not registered for GNCs dispersed in the protic solvent (water). Aq-GNCs as well as Ch-GNCs solutions exhibit NIR fluorescence with emission band maximum at 826 and 802 nm, respectively (with a 24 nm shift). The 12-crown-4 capped GNCs quantum yields are equal to 0.93 and 7.03 % for Aq-GNCs and Ch-GNCs, respectively.

The interaction of crown ethers with solvents and molecules of various polarity may play a crucial role in their utility for the sufficient staining of bio-interfaces[209]. Interestingly, the partition coefficient (the measure of the lipophilicity of a molecule) of 12-crown-4 ether was already presented in the literature and is within the 0.25 – 0.35 range[211]. However, for supramolecular compounds, the determination of hydrophobicity is not trivial, as it is governed by the numerous non-covalent interactions (including complex formation)[158]. To further investigate the amphiphilic properties of 12-crown-4-capped GNCs, and to determine

if they can preferentially transfer from aqueous to organic solvent, I decided to perform a phase transfer experiment. Briefly, as-synthesized 12-crown-4 ether-capped clusters were dissolved in water and the resulting solution was mixed with pure $CHCl_4$. I observed that, after 6 h from the phase separation event, GNCs spontaneously and irreversibly transferred from aqueous to organic solvent (see figure no. 45, b). However, after organic solvent evaporation, GNCs can be successfully re-dispersed in water. The aforementioned processing is not affecting the clusters' optical properties (see figure 45, c).

Due to the peculiar optical properties of 12-crown-4 ether-capped GNCs (*i.e.* fluorescence emission shift, quantum yield increase, and absorption change) registered for the corresponding Aq-GNCs and Ch-GNCs, I decided to investigate it further. I hypothesized that the observed phenomena may be the result of the solvent-induced (i) nanoparticles' size distribution, or (ii) aggregation. However, it is well established that crown ethers are characterized by the high flexibility of macrocyclic rings, and multiple conformers may be adapted in the presence of specific solvents or ions[159]. Perez *et al.* [158] showed the existence of mechanisms changing the conformation of 12-crown-4 ether, even for a "soft" ligand like water. Therefore, solvent-induced optical properties alteration may be also connected to (ii) the conformational changes of crown ether ligands. Hence, to probe whether either nanoparticles' size distribution or aggregation is present in our samples, TEM imaging was performed.

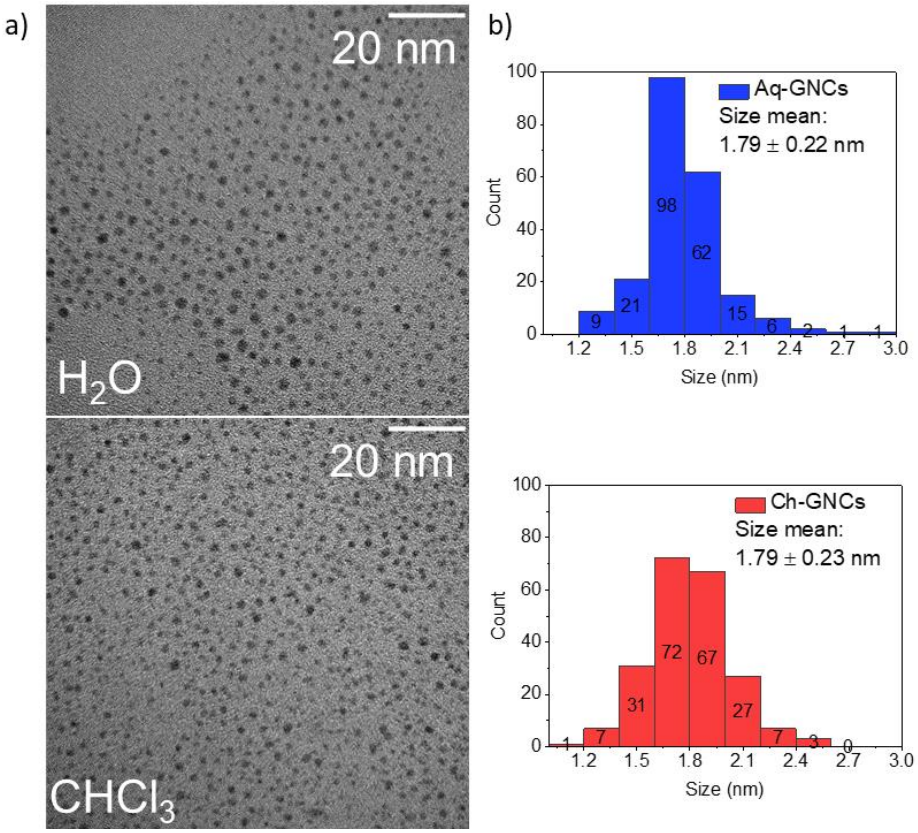

Figure 46. Gold nanoclusters size determination. a) TEM images of Aq-GNCs and Ch-GNCs and b) corresponding cluster size distribution (n = 215 for both TEM images). Adapted from reference no.[210] *(https://doi.org/10.1021/acsomega.3c00426)*, Copyright © 2023 Patryk Obstarczyk et al., Published by American Chemical Society.

According to the data presented in figure no. 46, 12-crown-4 ether-capped GNCs from both solutions are size-wise identical. Their sizes were measured to be in the range of 1.79 ± 0.22 nm and 1.79 ± 0.23 nm for Aq-GNCs and Ch-GNCs, respectively. Overall, 215 individual clusters were measured per sample. Neither aggregation, nor cluster size distribution change was observed, thus their structural integrity is maintained despite the solvent change. To support the claim, GNCs' discrete electronic structures were already proven to be sensitive to a single metal atom change, and cluster aggregation usually leads to a significant change in the UV-Vis spectra[106]. However, despite being in the size range typical for atomically-precise nanoclusters (< 2 nm)[81], based on TEM imaging alone, it is not possible to undoubtedly determine the number of gold atoms within the individual cluster. Presented herein 12-crown-4 ether-capped clusters are not atomically-precise.

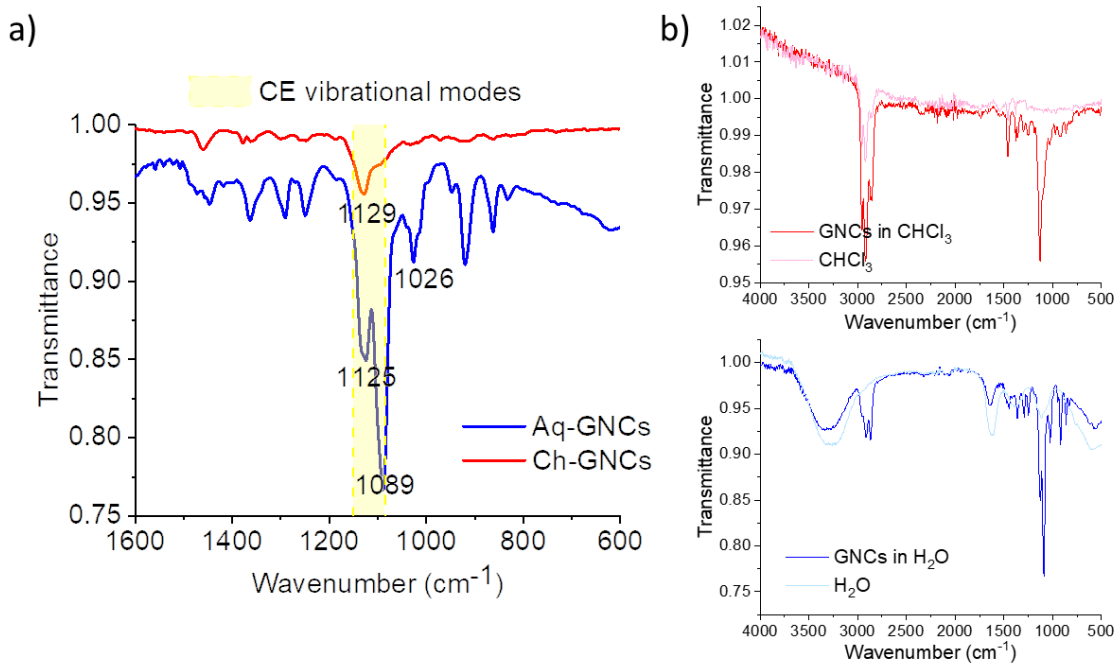

Figure 47. Crown ethers vibrational modes. a) The comparison of IR spectra of Aq- and Ch-GNCs, b) corresponding IR spectra of GNCs in aqueous (blue) and organic (red) solutions in comparison to signals generated by pure solvents. Adapted from reference no.[210] *(https://doi.org/10.1021/acsomega.3c00426)*, Copyright © 2023 Patryk Obstarczyk et al., Published by American Chemical Society.

Interestingly, the FT-IR spectra of Aq- and Ch-GNCs are different (see figure no. 47, a). Aq-GNCs are characterized by peaks located in the crown ether vibrational modes' wavenumber range. Namely, at 1125 and 1089 cm^{-1}, which may correspond to C-O stretching. These peacks are not registered for Ch-GNCs, which are characterized by a single peak at 1129 cm^{-1}. Moreover, the peak at 1026 cm^{-1} was registered for Aq-GNCs, which can be assigned to O–H deformation. If the response of pure solvents is considered (see figure no. 47, b), a 35 cm^{-1} peak shift was observed for Aq-GNCs, in comparison to pure H_2O spectra. It may correspond to O–H stretching (in the 3800–2800 cm^{-1} wavenumber range), associated with crown ether solvation. The data presented herein is a good agreement with FT-IR studies on bare crown ethers[212], where bands correlated with O-H stretching were broadened and shifted due to the

intramolecular interactions of crown ethers with solvent molecules. I hypothesize that the 12-crown-4 ether, in H_2O, adopts a folded conformation. The aforementioned phenomenon is governed by the non-covalent interactions between oxygen atoms from the macrocyclic ring (negatively charged) and hydrogen atoms (with a partial positive charge) from the water molecule, as determined by broadband rotational studies[213]. However, theoretical calculations including molecular restrictions arising from the gold-sulfur interfaces would be beneficial to perform.

Bearing in mind the investigation results presented above, the assumption regarding the peculiar optical properties of Aq- and Ch-GNCs resulting from (iii) 12-crown-4 ether conformational changes are favored by me. To further support it, in the literature, the claim that the photoluminescent properties of GNCs can be altered by surface ligands was already established, both experimentally and theoretically [91, 131, 214]. The ligand charge, rotational freedom as well as Au-S geometry has a profound influence on GNCs' electronic structure, and the non-radiative as well as radiative channels of GNCs relaxation. Therefore, I suggest that the 7-fold QY yield increase, 24 nm emission maxima shift, and distinct absorption change at 320 nm are indeed arising from 12-crown-4 ether conformational changes induced by solvents.

The photoluminescence, high electron density, as well as amphiphilic character of my GNCs can be advantageous for cross-platform imaging. Therefore I was eager to apply them as markers for bio-interface imaging. For that, I chose model structures, namely amyloid spherulites (comprehensively defined in Chapter I, subchapter 1.3.). In brief, spherulites are complex and densely-packed structures composed of amorphous core (rich in α-helices) and radially growing fibrils (rich in β-sheets)[14]. Spherulites are morphologically characterized by a complex mix of domains of distinct hydrophobicity, which was found to limit their susceptibility to being stained by hydrophilic dyes[190-191]. I prepared insulin spherulites (see the Materials and experimental methods section – Chapter V, subchapter 3.5.) and stained them by mixing them with 12-crown-4 GNC. However, to discuss the amphiphilicity of crown ethers and its influence on binding to spherulites, a control experiment was designed. With the help of A. Pniakowska, and A. Hajda, the water-soluble GNCs stabilized with a hydrophilic ligand were synthesized, namely $Au_{18}(SG)_{14}$ (where SG stands for glutathione). Absorption and emission spectra of Au_{18} GNCs were measured, and their hydrophilic character was confirmed by negative results from the phase transfer experiment (see figure no. 48, a).

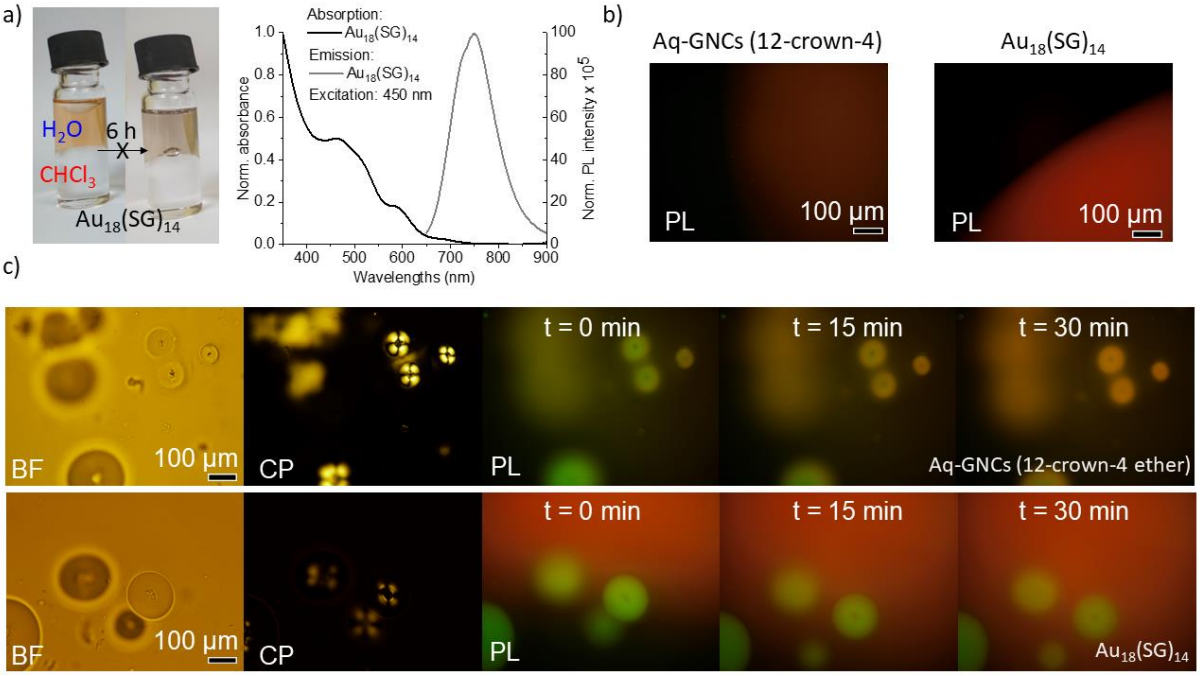

Figure 48. Amyloid spherulites and gold nanoclusters. a) Negative results from the phase transfer (water to chloroform) experiment for $Au_{18}(SG)_{14}$ stabilized with hydrophilic ligand (SG - glutathione), and $Au_{18}(SG)_{14}$ GNCs' optical properties (measured in water), (b) fluorescence microscopy images of an aqueous solution droplet of Aq-GNCs (12-crown-4 ether) and $Au_{18}(SG)_{14}$, (c) corresponding bright-field optical microscopy images of spherulites mixed with 12-crown-4 ether-capped GNCs (upper panel) and $Au_{18}(SG)_{14}$ GNCs (lower panel) taken without polarizers (BF), with crossed polarizers (CP), and in the epifluorescence mode where red photoluminescence (PL) was registered. Photos in the PL mode were taken within a 30 min period (every 15 min), starting from GNC solution addition. Green signal is identified as incident light scattering. Reprinted from reference no.[210] (*https://doi.org/10.1021/acsomega.3c00426*), Copyright © 2023 Patryk Obstarczyk et al., Published by American Chemical Society.

I performed imaging of the hybrid samples (composed of amyloids and clusters), in their native, and hydrated environment (see figure no. 48, c). Images were taken under a microscope in the bright field (BF) and epifluorescence mode (PL). Comprehensive sample preparation description, as well as technical aspects of microscopes, are available in the Materials and experimental methods section. Additionally, to confirm the presence of spherulites in the samples, I performed imaging under polarized light (in a setup with crossed polarizers – CP, figure no. 48, c). A characteristic extinction pattern (*i.e.* Maltase cross) was observed, which proved the successful incubation of amyloid spherulites. However, to probe GNCs' affinity to amyloids time-resolved imaging, in the epifluorescence mode (figure no. 48, c PL), was performed. Photos were taken every 15 min, starting from the GNCs addition event. As presented in figure no. 48c, the spherulites tend to glow green, which is the result of the incident light scattering. However, a red emission of clusters was also clearly visible. Interestingly, the 12-crown-4 ether-capped GNCs immediately assembled in the spherulites, as red emission could be measured in a no-time from the entire superstructures (figure no. 48, c, upper panel). In contrast, the hydrophilic Au_{18} GNCs did not penetrate the spherulites, under

the same experimental conditions, thus no red emission was registered from the spherulites' inner areas.

As already mentioned, amyloid spherulites (and fibrils) are composed of hydrophilic and hydrophobic domains. The amyloid superstructures were already studied as hosts for the lipophilic and lipophobic fluorescent probes, namely 1-anilinonapthalene-8 sulfonic acid (ANS), and Alexa647, respectively. In studies performed by Vetri *et al.,* [191] the hydrophilic staining agent was proven to be unsuccessful in staining internal parts of the spherulites. Herein, I observed a similar behavior, where glutathione-stabilized GNCs (hydrophilic) could not successfully penetrate the densely packed bio-system. However, the amphiphilic clusters were able to do it immediately after addition, which indicates the high affinity to the model surfaces. I hypothesized that 12-crown-4 ether-capped GNCs can release water molecules from the closest environment and preferentially interact with amyloids utilizing hydrogen bonding, electrostatic interactions, and van der Walls/hydrophobic interactions (revisit proposed model, see figure no. 43). Interestingly, it has been reported, based on theoretical calculations as well as experimental data, that 12-crown-4 ether molecules are indeed interacting with Aβ40 fibrils, based on mechanisms enlisted in my hypothesis description[208-209].

The spontaneous phase transfer (from aqueous to organic solvent) of 12-crown-4 ether-capped GNCs, as well as their distinct interactions with bio-interfaces (efficient binding to amyloids) inspired me to investigate it further. Although, from the first concept, my GNCs were designed to be suitable for multimodal imaging, their enhanced functionality has emerged. I hypothesized, that presented herein amphiphilic GNCs can be also utilized for the spatially resolved detection of hydrophobic domains on bio-interfaces, on a nano-scale. Since my probe design is based on electron-dense components (gold atoms), they might be an excellent candidate for electron imaging. Therefore, I decided to prepare amyloid fibrils, stained them with 12-crown-4 ether-capped GNCs, and perform TEM imaging with subsequent image analysis.

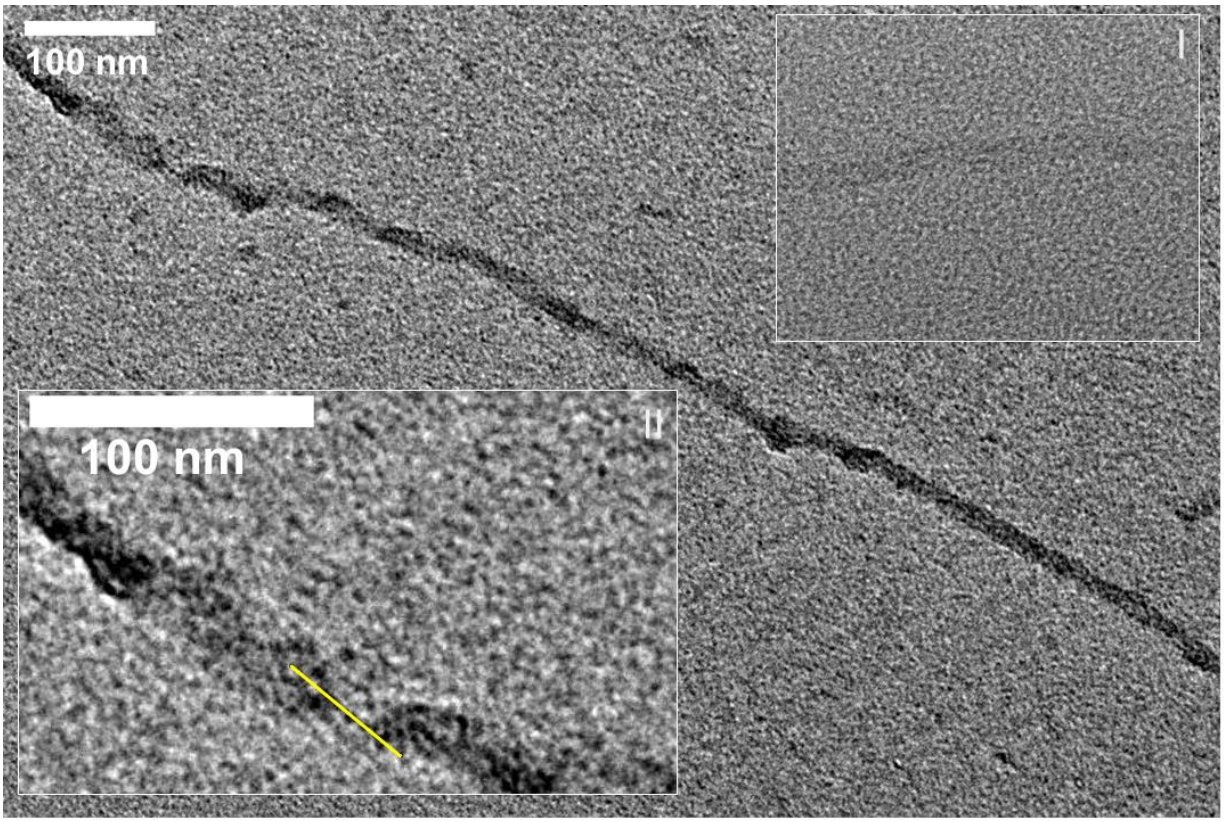

Figure 49. Electron imaging. High-magnification TEM image of a single amyloid fibril stained with GNCs (12-crown-4 ether-capped) with an inset showing GNCs organization. Inset in the upper-right (I) corner shows a stain-free amyloid fibril, from the corresponding solution. For the inset that is located in the left-down corner (II), the yellow line corresponds to an exemplary area within which cluster organization was analyzed. Adapted from reference no.[210] *(https://doi.org/10.1021/acsomega.3c00426),* Copyright © 2023 Patryk Obstarczyk et al., Published by American Chemical Society.

As presented in figure no. 49, the 12-crown-4 ether-capped GNCs are an excellent contrasting agent for amyloid TEM imaging. Amphiphilic clusters heavily decorated amyloid surfaces. The majority of clusters are deposited on fibril, as their number in the amyloid-free areas is insignificant and can be neglected. The bare (label-free) amyloid fibrils are composed of amino acids, therefore they are barely visible (see inset in the upper-right corner - I). Therefore, for amyloid fibrils TEM image analysis, the structural data cannot be obtained if stain-free conditions are applied. Most importantly, my GNCs are deposited on fibrils in patterns, which might be utilized to reveal the morphological features of amyloid aggregates. Therefore, I decided to analyze the grey scale values across the longitudinal as well as transverse axis of the fibrils. Additionally, I performed the analysis of cluster-to-cluster distance, for the individuals located in the middle of fibrils (see the yellow line, figure no. 49 (the lower-left inset - II)). Grey values profiles, where low intensity is correlated to the presence of the clusters, are presented in figure no. 50.

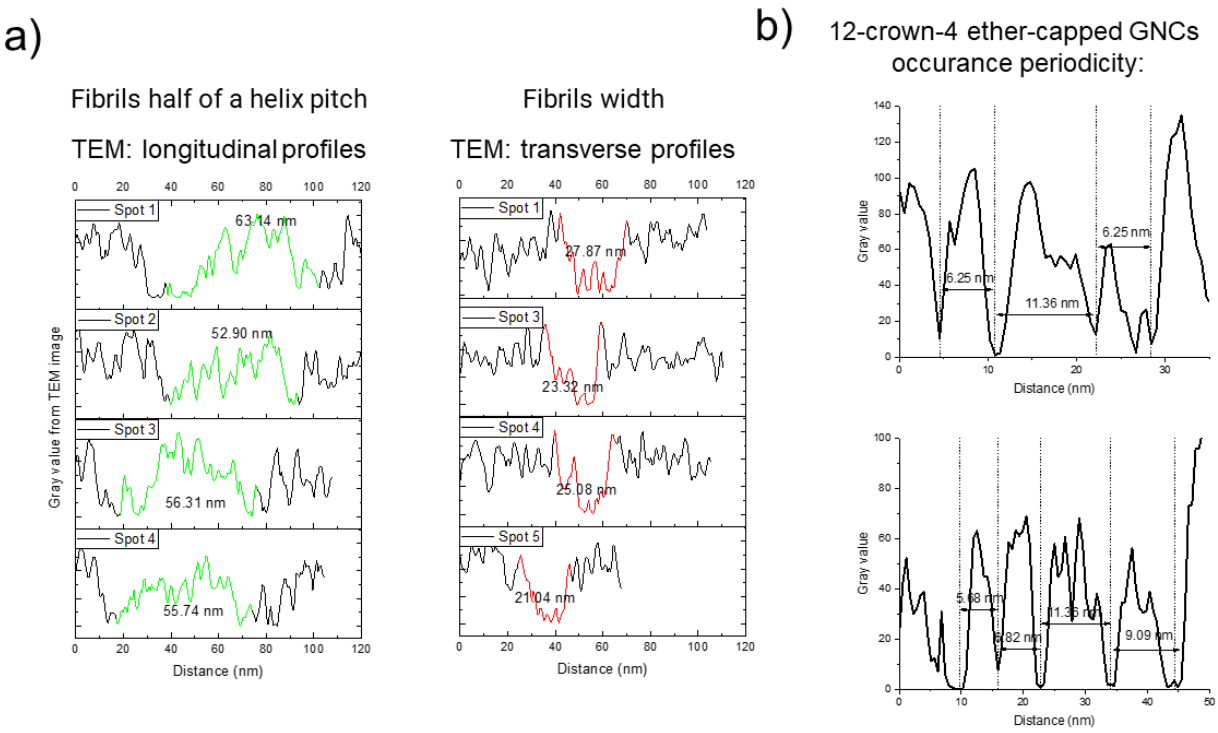

Figure 50. GNCs decorated fibrils structural analysis. a) Longitudinal and transverse grey scale profiles taken from TEM image of amyloid fibril (decorated with 12-crown-4 ether-capped GNCs), b) exemplary amyloid fibril longitudinal gray-scale intensity profile measured from TEM images corresponding to the GNCs' occurrence periodicity. Adapted from reference no.[210] *(https://doi.org/10.1021/acsomega.3c00426),* Copyright © 2023 Patryk Obstarczyk et al., Published by American Chemical Society.

I used the data presented herein (figure no. 50a) to calculate the fibril mean width and half of a helix pitch, which were equal to 24.34 ± 2.87 and 55.15 ± 5.62 nm, respectively. I hypothesized that 12-crown-4 ether-capped GNCs might reveal the structural information on amyloid fibrils morphology, which cannot be resolved *via* stain-free electron imaging. However, atomic force microscopy (AFM) is the method of choice for the morphological investigations on the amyloid fibrils[29]. Therefore, I decided to employ the aforementioned technique to compare results obtained under the transmission electron microscope (see fig. no. 51).

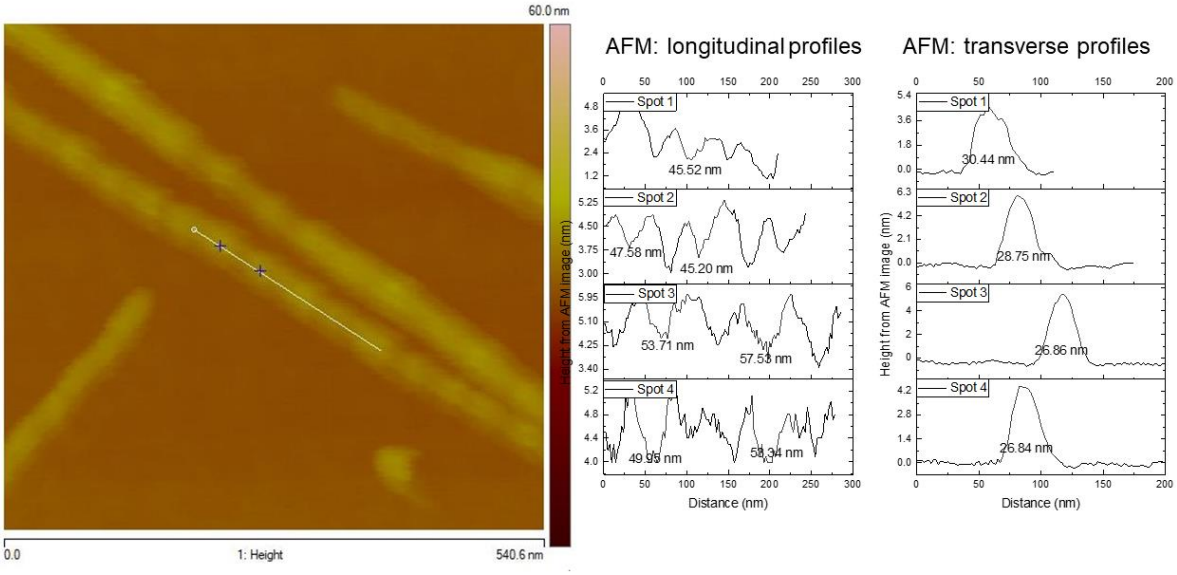

Figure 51. Atomic force microscopy. Atomic force microscopy height scan of corresponding stain-free amyloid fibrils, as well as their longitudinal and transverse profiles. Reprinted from reference no.[210] *(https://doi.org/10.1021/acsomega.3c00426)*, Copyright © 2023 Patryk Obstarczyk et al., Published by American Chemical Society.

The morphology of stain-free amyloid fibrils performed with atomic force microscopy revealed that the mean width and the half of a helix pitch values were equal to 28.22 ± 1.73 and 55.96 ± 8.26 nm, respectively. It corresponds to values observed with GNCs-decorated fibrils, from electron imaging.

However, as presented in figure no. 50b, gold nanoclusters on amyloid fibrils surface tend to form patterns by occurring repetitively (*i.e.* every 5 or 10 nm, in straight lines). Such a phenomenon may arise due to the inherited properties of amyloid fibrils, namely steric anchors created by the protofilament's twist[44]. However, apart from geometric constraints, the hydrophobic domains spatial distribution may be also responsible. Interestingly, insulin amyloid fibrils are characterized by a distinct distribution of hydrophobic and mixed (partially hydrophilic) domains. According to Deckert-Gaudig *et al.*[45], these domains occur alternatively, every 5 or 10 nm (as measured along the 24 nm segment from the inner part of the fibril). Presented herein, 12-crown-4 ether-capped GNCs distribution is well corresponding to the aforementioned report. Moreover, it was already theoretically as well as experimentally established that the gold nanoparticles' affinity to amyloids is strongly dependent on the hydrophobic contacts (between the ligand and fibril)[77, 112]. Therefore, 12-crown-4 ether-capped GNCs can be applied as a versatile and multimodal staining agent, with an enhanced functionality, namely high affinity to hydrophobic surfaces.

5 Conclusions

I synthesized and characterized ultra-small (~ 1.7 nm) gold nanoclusters with molecule-like properties. Additionally, for bio-imaging, their size is particularly beneficial to achieve high spatial resolution, in comparison to large (above 100 nm) plasmonic nanostructures. The supramolecular ligand of my choice donated its remarkable properties onto nanoclusters, which allowed me to apply them in bio-imaging. My research demonstrates that 12-crown-4 ether-capped gold nanoclusters are potent for application as effective markers for fluorescent bioimaging in the near-infrared range. Moreover, due to the high electron density of gold, they are also suitable for electron imaging. Therefore, clusters synthesized in frames of the scientific endeavors undertaken within the frames of this thesis are potentially multimodal. The amphiphilic properties of the supramolecular ligand system result in a strong binding to bio-interfaces, due to the non-covalent interactions. I showed that these clusters can be successfully and repeatedly transferred between solvents (aqueous and organic) without any changes in their size, as confirmed via TEM imaging. The ligand system introduces a sensitivity to clusters nearest molecular environment. The flexibility of the macrocyclic compounds allows them to adjust their conformation, which can be controlled by the solvent change. It also influences clusters' electronic structure, as the absorption spectra, quantum yields, and emission wavelength were tuned. My research opens up attractive paths for the research on ligands' influence on nanocluster luminescence. I believe that the presented herein gold nanocluster system, based on crown ethers capping agent, can provide valuable insight into manipulating the physicochemical properties at the nano-scale for both nanomaterials and bio-interfaces. I believe that the affinity to hydrophobic environments exhibited by 12-crown-4 ether-capped nanoclusters can be used as a functional tool for versatile and multimodal imaging or biomedical applications.

Chapter VI – Summary and perspectives

Within the framework of this thesis, I conducted a series of experiments to examine and substantiate hypotheses put forth at the outset of this work. Herein I will re-draw the main points form the foregoing discussion from chapter no. III, IV, and IV to present a summary of my findings, specifically as they pertain to the aforementioned hypotheses. After that, I will discuss future challenges and perspectives to further improve my findings.

Hypothesis I: It is possible to utilize the intrinsic nonlinear optical properties of amyloids to develop a label-free imaging method based on the two-photon excited fluorescence microscopy.

I prepared amyloid spherulites and designed the preparative methodology to perform sample imaging based on fluorescence, in an amyloid native and hydrated environment. Then, I confirmed the presence of spherulites by the observation of Maltese cross patterns, as seen under polarized light microscopy, with crossed polarizers. Additionally, I imaged them under a scanning electron microscope. The structural aspect ratio (defined as the spherulites overall diameter divided by core diameter) of stain-free and ThT-labelled spherulites was equal to 6.55 ± 3.33 and 6.4 ± 1.89 μm, respectively. In the next step, their one-photon emission was measured, for the excitation wavelength set to 375 nm. Correspondingly, two-photon autofluorescence (2PAF) was registered for 810 nm excitation. The multi-photon character of emission was confirmed, as the ~quadratic dependence of the two-photon fluorescence intensity on incident laser power was observed (1.85 and 1.93, for autofluorescence and ThT, respectively). Thus, intrinsic two-photon excited autofluorescence of amyloids could be probed. I utilized polarization-sensitive two-photon microscopy to examine unstained amyloid superstructures and determined that the angular distribution of amyloid autofluorescence is located at 29 degrees from the long axis of the fibrils. This result was validated by a control experiment involving Thioflavin-T-stained amyloids, where the angular distribution of the dye bound to amyloid fibrils was found to be equal to 30 degrees. Therefore, the second assumption from the hypothesis was validated with a positive result. Moreover, the atomic force microscopy of individual fibrils indicated that the relative angle between the long axis of amyloid fibrils and the transition dipole moments of two-photon excited amyloid autofluorescence can be affected by the number or conformation of protofibrils (i.e. fibrils morphology). Thereby, my method could enable the potential detection and differentiation of amyloid polymorphs in a stain-free manner.

Hypothesis II: It is possible to utilize the polarization analysis of two-photon excited amyloid autofluorescence to resolve the structural ordering in a densely packed sample and identify the distorted or intermediate states of amyloid fibrils.

I prepared the amyloid spherulites and imaged them under PS-2PFM. Correspondingly, the method based on fixation and thin sectioning of tissues was adapted for spherulites, to enable co-imaging under a transmission electron microscope (TEM). With two modalities I detected the heterogeneity within the spherulitic ensembles: corresponding regions of distinct organization and packing could be depicted by both modalities. The qualitative analysis of TEM imaging allowed me to detect well-developed and organized fibrils in the spherulite's outer corona. However, the inner corona of spherulite as well as the core were characterized by decreasing ordering and the presence of amorphous aggregates or distorted fibrils. The corresponding areas from spherulites raster scans derived from PS-2PFM were characterized by distinctive ΔΨ values (*i.e.* aberration of conical distribution of the orientation of emission dipole moments) – increasing along the spherulite's radius, from the spherulite periphery to the core. Therefore, local molecular ordering and structural information on amyloids were revealed. Bearing in mind the foregoing, my second hypothesis was also validated with positive

results, as two-photon excited autofluorescence of amyloids was proved to be structure dependent and can serve to detect the distorted or intermediate states of amyloid-fibrils.

Hypothesis III: It is possible to design a near-infra-red emitting and functional probe based on electron-dense nanomaterials (e.g. gold nanoclusters) for multimodal amyloid imaging (fluorescence and electron microscopy).

I synthesized ultra-small (~ 1.7 nm) gold nanoclusters via the gold salt reduction in the presence of a supramolecular ligand (12-crown-4 ether). In the next step, I performed the physicochemical characterization of my nano-material. I show that these clusters are stable and can be successfully and spontaneously transferred from aqueous to organic solvent. Therefore, the amphiphilic character with a higher affinity to the organic medium was confirmed. Moreover, in both solvents, these clusters are characterized by common molecule-like optical properties, namely discrete electronic transition at 450 nm. However, upon transition into the organic solvent, my nanoclusters develop an additional band at 320 nm. Independently of the solvent, clusters are near infra-red (NIR) luminescent. The emission maximum for an aqueous solution was registered at 802 nm, whereas the 24 nm emission red shift was observed for nanoclusters in organic solvent (826 nm). The corresponding quantum yields were equal to 0.93 and 7.03%, for aqueous and organic gold nanoclusters solutions, respectively. To confirm that clusters maintain their structural integrity upon solvent change, TEM imaging was performed. The corresponding cluster sizes were 1.79 ± 0.22 and 1.79 ± 0.23, for water and chloroform solutions, correspondingly. Therefore, potential aggregation or core size alteration was excluded. To explain the peculiar changes in the optical properties of clusters upon solvent change, additional FT-IR measurements were conducted. I show that 12-crown-4 ether can adapt distinctive conformations, in dependence on its closest environment (including solvent molecules). Thus, I assigned the aforementioned modulation of optical properties to alterations of gold sulfur interface geometry, highly influenced by the conformation of the stabilizing ligand. I applied an aqueous solution of 12-crown-4 ether-capped nanoclusters to stain amyloid fibrils and spherulites. My amphiphilic clusters immediately stained amyloid spherulites, as observed under a microscope operated in the epi-fluorescence mode. The control experiment, where clusters stabilized with hydrophilic ligand (glutathione) was also introduced. However, glutathione-stabilized clusters did not penetrate the spherulites, under the same experimental conditions. Therefore, I show that my clusters can be utilized as an effective marker for fluorescent bioimaging in the near-infrared range. Due to the high electron density of gold, my clusters were also applied as markers for electron imaging of amyloid fibrils. They successfully stained individual amyloid fibrils and revealed information on their structure (e.g. fibrils helix pitch and width). Moreover, cluster pattering was corresponding to the previously reported distribution of hydrophobic domains on amyloid insulin fibrils. Overall, all aspects of hypothesis no. III have been tested, and validated with positive results.

Findings presented within the framework of this thesis are corresponding to modern problems depicted by the leaders of the amyloid bio-imaging field. However, some additional challenges have been identified, and in perspective, it would be beneficial to address the issues enlisted herein:

- To better understand the correlation between the structure and corresponding polarization dependence of amyloid two-photon excited autofluorescence it would be beneficial to perform the polarization analysis of amyloids grown from a variety of proteins and peptides, especially for systems characterized by the parallel and anti-parallel cross-β organization. Additionally, amyloid polymorphs should be thoroughly tested, to set the detection limitations for PS-2PFM.
- Numerous biological materials tend to be fluorescent, as excited with UV light. However, the aforementioned phenomenon is usually based on aromatic amino acids. It would be beneficial to apply the same experimental (PS-2PFM) for samples derived from living organisms, where the aberrations potentially introduced by the structures not related to amyloids could be estimated. Such a strategy could help to speed up the transition of PS-2PFM based on amyloid autofluorescence onto *in vivo* imaging.
- The protocol for 12-crown-4 ether-capped gold nanoclusters synthesis could be altered to obtain atomically-precise structures. According to recent reports, the introduction of NaOH could be beneficial, to decrease the reducing potential of $NaBH_4$, thus helping to achieve higher control on gold-thiol polymers reduction kinetics. Alternatively, future research could focus on a different size-selective synthesis method, or advanced separation techniques.
- Since the relative quantum yields of the presented herein clusters are low in comparison to the standard organic dyes, future research could focus on its enhancement (e.g. by ligand immobilization, or gold/sulfur oxidation).
- It would be beneficial to achieve control over the 12-crown-4 ether-capped gold nanoclusters hydrophobicity by utilization of 12-crown-4 ether supramolecular properties. In detail, it was reported that upon non-covalent metal cation complexation, crown ether's moiety can become more hydrophobic. Therefore, the specific molar ratios of e.g. Li^+ to 12-crown-4-SH could highly influence the amphiphilicity of the entire clusters. The aforementioned strategy could help to detailly image the surface polarity of various biological materials, in a multimodal manner.
- Gold nanoclusters were already applied as robust materials for nonlinear optical applications. Therefore, it would be beneficial to characterize the nonlinear performance (e.g. two-photon absorption cross sections) of 12-crown-4 ether-capped nanoclusters and apply them as a multi-photon staining agent.

Bibliography

1. Ke, P. C.; Zhou, R.; Serpell, L. C.; Riek, R.; Knowles, T. P. J.; Lashuel, H. A.; Gazit, E.; Hamley, I. W.; Davis, T. P.; Fändrich, M.; Otzen, D. E.; Chapman, M. R.; Dobson, C. M.; Eisenberg, D. S.; Mezzenga, R., Half a century of amyloids: past, present and future. *Chemical Society Reviews* **2020,** *49* (15), 5473-5509.
2. Fändrich, M.; Nyström, S.; Nilsson, K. P. R.; Böckmann, A.; LeVine, H., 3rd; Hammarström, P., Amyloid fibril polymorphism: a challenge for molecular imaging and therapy. *Journal of internal medicine* **2018,** *283* (3), 218-237.
3. Segers-Nolten, I.; van Raaij, M.; Subramaniam, V., 2.219 - Biophysical Analysis of Amyloid Formation. In *Comprehensive Biomaterials*, Ducheyne, P., Ed. Elsevier: Oxford, 2011; pp 347-359.
4. Sipe, J. D.; Benson, M. D.; Buxbaum, J. N.; Ikeda, S. I.; Merlini, G.; Saraiva, M. J.; Westermark, P., Amyloid fibril proteins and amyloidosis: chemical identification and clinical classification International Society of Amyloidosis 2016 Nomenclature Guidelines. *Amyloid : the international journal of experimental and clinical investigation : the official journal of the International Society of Amyloidosis* **2016,** *23* (4), 209-213.
5. Collins, S. R.; Douglass, A.; Vale, R. D.; Weissman, J. S., Mechanism of Prion Propagation: Amyloid Growth Occurs by Monomer Addition. *PLOS Biology* **2004,** *2* (10), e321.
6. Iadanza, M. G.; Jackson, M. P.; Hewitt, E. W.; Ranson, N. A.; Radford, S. E., A new era for understanding amyloid structures and disease. *Nature Reviews Molecular Cell Biology* **2018,** *19* (12), 755-773.
7. Prince, M.; Bryce, R.; Albanese, E.; Wimo, A.; Ribeiro, W.; Ferri, C. P., The global prevalence of dementia: A systematic review and metaanalysis. *Alzheimer's & Dementia* **2013,** *9* (1), 63-75.e2.
8. Huang, Y.; Mucke, L., Alzheimer Mechanisms and Therapeutic Strategies. *Cell* **2012,** *148* (6), 1204-1222.
9. Cimler, R.; Maresova, P.; Kuhnova, J.; Kuca, K., Predictions of Alzheimer's disease treatment and care costs in European countries. *PLOS ONE* **2019,** *14* (1), e0210958.
10. Magill, J. H., Review Spherulites: A personal perspective. *Journal of Materials Science* **2001,** *36* (13), 3143-3164.
11. Bassett, D. C., Polymer Spherulites: A Modern Assessment. *Journal of Macromolecular Science, Part B* **2003,** *42* (2), 227-256.
12. Khurana, R.; Gillespie, J. R.; Talapatra, A.; Minert, L. J.; Ionescu-Zanetti, C.; Millett, I.; Fink, A. L., Partially Folded Intermediates as Critical Precursors of Light Chain Amyloid Fibrils and Amorphous Aggregates. *Biochemistry* **2001,** *40* (12), 3525-3535.
13. Smith, M. I.; Foderà, V.; Sharp, J. S.; Roberts, C. J.; Donald, A. M., Factors affecting the formation of insulin amyloid spherulites. *Colloids and Surfaces B: Biointerfaces* **2012,** *89*, 216-222.
14. Krebs, M. R. H.; MacPhee, C. E.; Miller, A. F.; Dunlop, I. E.; Dobson, C. M.; Donald, A. M., The formation of spherulites by amyloid fibrils of bovine insulin. *Proceedings of the National Academy of Sciences of the United States of America* **2004,** *101* (40), 14420-14424.
15. House, E.; Jones, K.; Exley, C., Spherulites in Human Brain Tissue are Composed of Beta Sheets of Amyloid and Resemble Senile Plaques. *Journal of Alzheimer's Disease* **2011,** *25*, 43-46.

16. Exley, C.; House, E.; Collingwood, J. F.; Davidson, M. R.; Cannon, D.; Donald, A. M., Spherulites of amyloid-beta42 in vitro and in Alzheimer's disease. *Journal of Alzheimer's disease : JAD* **2010,** *20* (4), 1159-65.
17. Manuelidis, L.; Fritch, W.; Xi, Y.-G., Evolution of a Strain of CJD That Induces BSE-Like Plaques. *Science (New York, N.Y.)* **1997,** *277* (5322), 94-98.
18. Rogers, S. S.; Krebs, M. R. H.; Bromley, E. H. C.; van der Linden, E.; Donald, A. M., Optical Microscopy of Growing Insulin Amyloid Spherulites on Surfaces In Vitro. *Biophysical Journal* **2006,** *90* (3), 1043-1054.
19. De Luca, G.; Fennema Galparsoro, D.; Sancataldo, G.; Leone, M.; Foderà, V.; Vetri, V., Probing ensemble polymorphism and single aggregate structural heterogeneity in insulin amyloid self-assembly. *Journal of Colloid and Interface Science* **2020,** *574*, 229-240.
20. Zhang, M.; Pinholt, H. D.; Zhou, X.; Bohr, S. S. R.; Banetta, L.; Zaccone, A.; Foderà, V.; Hatzakis, N. S., Direct observation of heterogeneous formation of amyloid spherulites in real-time by super-resolution microscopy. *Communications Biology* **2022,** *5* (1), 850.
21. Sipe, J. D.; Cohen, A. S., Review: History of the Amyloid Fibril. *Journal of Structural Biology* **2000,** *130* (2), 88-98.
22. Hippius, H.; Neundörfer, G., The discovery of Alzheimer's disease. *Dialogues in clinical neuroscience* **2003,** *5* (1), 101-8.
23. Shirahama, T.; Cohen, A. S., High-resolution electron microscopic analysis of the amyloid fibril. *The Journal of cell biology* **1967,** *33* (3), 679-708.
24. Cohen, A. S.; Calkins, E., Electron Microscopic Observations on a Fibrous Component in Amyloid of Diverse Origins. *Nature* **1959,** *183* (4669), 1202-1203.
25. Geddes, A. J.; Parker, K. D.; Atkins, E. D. T.; Beighton, E., "Cross-β" conformation in proteins. *Journal of Molecular Biology* **1968,** *32* (2), 343-358.
26. Li, D.; Liu, C., Hierarchical chemical determination of amyloid polymorphs in neurodegenerative disease. *Nature Chemical Biology* **2021,** *17* (3), 237-245.
27. Hiramatsu, T.; Yamamoto, N.; Ha, S.; Masuda, Y.; Yasuda, M.; Ishigaki, M.; Yuzu, K.; Ozaki, Y.; Chatani, E., Iodine staining as a useful probe for distinguishing insulin amyloid polymorphs. *Scientific Reports* **2020,** *10* (1), 16741.
28. Cohen, M. L.; Kim, C.; Haldiman, T.; ElHag, M.; Mehndiratta, P.; Pichet, T.; Lissemore, F.; Shea, M.; Cohen, Y.; Chen, W.; Blevins, J.; Appleby, B. S.; Surewicz, K.; Surewicz, W. K.; Sajatovic, M.; Tatsuoka, C.; Zhang, S.; Mayo, P.; Butkiewicz, M.; Haines, J. L.; Lerner, A. J.; Safar, J. G., Rapidly progressive Alzheimer's disease features distinct structures of amyloid-β. *Brain : a journal of neurology* **2015,** *138* (Pt 4), 1009-22.
29. Adamcik, J.; Mezzenga, R., Study of amyloid fibrils via atomic force microscopy. *Current Opinion in Colloid & Interface Science* **2012,** *17* (6), 369-376.
30. Kad, N. M.; Myers, S. L.; Smith, D. P.; Smith, D. A.; Radford, S. E.; Thomson, N. H., Hierarchical assembly of beta2-microglobulin amyloid in vitro revealed by atomic force microscopy. *J Mol Biol* **2003,** *330* (4), 785-97.
31. Ries, J.; Udayar, V.; Soragni, A.; Hornemann, S.; Nilsson, K. P.; Riek, R.; Hock, C.; Ewers, H.; Aguzzi, A. A.; Rajendran, L., Superresolution imaging of amyloid fibrils with binding-activated probes. *ACS Chem Neurosci* **2013,** *4* (7), 1057-61.
32. Dong, J.; Revilla-Sanchez, R.; Moss, S.; Haydon, P. G., Multiphoton in vivo imaging of amyloid in animal models of Alzheimer's disease. *Neuropharmacology* **2010,** *59* (4), 268-275.
33. Żak, A., Guide to controlling the electron dose to improve low-dose imaging of sensitive samples. *Micron (Oxford, England : 1993)* **2021,** *145*, 103058.

34. Jagota, M.; Townshend, R. J. L.; Kang, L.-W.; Bushnell, D. A.; Dror, R. O.; Kornberg, R. D.; Azubel, M., Gold nanoparticles and tilt pairs to assess protein flexibility by cryo-electron microscopy. *Ultramicroscopy* **2021,** *227*, 113302.
35. Gremer, L.; Schölzel, D.; Schenk, C.; Reinartz, E.; Labahn, J.; Ravelli, R. B. G.; Tusche, M.; Lopez-Iglesias, C.; Hoyer, W.; Heise, H.; Willbold, D.; Schröder, G. F., Fibril structure of amyloid-β(1-42) by cryo-electron microscopy. *Science (New York, N.Y.)* **2017,** *358* (6359), 116-119.
36. Fitzpatrick, A. W. P.; Falcon, B.; He, S.; Murzin, A. G.; Murshudov, G.; Garringer, H. J.; Crowther, R. A.; Ghetti, B.; Goedert, M.; Scheres, S. H. W., Cryo-EM structures of tau filaments from Alzheimer's disease. *Nature* **2017,** *547* (7662), 185-190.
37. Vadukul, D. M.; Al-Hilaly, Y. K.; Serpell, L. C., Methods for Structural Analysis of Amyloid Fibrils in Misfolding Diseases. *Methods in molecular biology (Clifton, N.J.)* **2019,** *1873*, 109-122.
38. Gobeaux, F.; Wien, F., Reversible Assembly of a Drug Peptide into Amyloid Fibrils: A Dynamic Circular Dichroism Study. *Langmuir* **2018,** *34* (24), 7180-7191.
39. Zandomeneghi, G.; Krebs, M. R.; McCammon, M. G.; Fändrich, M., FTIR reveals structural differences between native beta-sheet proteins and amyloid fibrils. *Protein science : a publication of the Protein Society* **2004,** *13* (12), 3314-21.
40. Buell, A. K., The growth of amyloid fibrils: rates and mechanisms. *Biochemical Journal* **2019,** *476* (19), 2677-2703.
41. Ladner, C. L.; Chen, M.; Smith, D. P.; Platt, G. W.; Radford, S. E.; Langen, R., Stacked sets of parallel, in-register beta-strands of beta2-microglobulin in amyloid fibrils revealed by site-directed spin labeling and chemical labeling. *The Journal of biological chemistry* **2010,** *285* (22), 17137-47.
42. Biessels, G. J.; Kappelle, L. J., Increased risk of Alzheimer's disease in Type II diabetes: insulin resistance of the brain or insulin-induced amyloid pathology? *Biochemical Society Transactions* **2005,** *33* (5), 1041-1044.
43. Tzotzos, S.; Doig, A. J., Amyloidogenic sequences in native protein structures. *Protein Science* **2010,** *19* (2), 327-348.
44. Jiménez, J. L.; Nettleton, E. J.; Bouchard, M.; Robinson, C. V.; Dobson, C. M.; Saibil, H. R., The protofilament structure of insulin amyloid fibrils. *Proceedings of the National Academy of Sciences* **2002,** *99* (14), 9196-9201.
45. Deckert-Gaudig, T.; Kurouski, D.; Hedegaard, M. A. B.; Singh, P.; Lednev, I. K.; Deckert, V., Spatially resolved spectroscopic differentiation of hydrophilic and hydrophobic domains on individual insulin amyloid fibrils. *Scientific Reports* **2016,** *6* (1), 33575.
46. Ghisaidoobe, A. B.; Chung, S. J., Intrinsic tryptophan fluorescence in the detection and analysis of proteins: a focus on Förster resonance energy transfer techniques. *International journal of molecular sciences* **2014,** *15* (12), 22518-38.
47. Cheng, Z.; Kuru, E.; Sachdeva, A.; Vendrell, M., Fluorescent amino acids as versatile building blocks for chemical biology. *Nature Reviews Chemistry* **2020,** *4* (6), 275-290.
48. Chan, F. T.; Kaminski Schierle, G. S.; Kumita, J. R.; Bertoncini, C. W.; Dobson, C. M.; Kaminski, C. F., Protein amyloids develop an intrinsic fluorescence signature during aggregation. *The Analyst* **2013,** *138* (7), 2156-62.
49. Shukla, A.; Mukherjee, S.; Sharma, S.; Agrawal, V.; Radha Kishan, K. V.; Guptasarma, P., A novel UV laser-induced visible blue radiation from protein crystals and aggregates: scattering artifacts or fluorescence transitions of peptide electrons delocalized through hydrogen bonding? *Archives of biochemistry and biophysics* **2004,** *428* (2), 144-53.

50. Pinotsi, D.; Grisanti, L.; Mahou, P.; Gebauer, R.; Kaminski, C. F.; Hassanali, A.; Kaminski Schierle, G. S., Proton Transfer and Structure-Specific Fluorescence in Hydrogen Bond-Rich Protein Structures. *Journal of the American Chemical Society* **2016,** *138* (9), 3046-3057.
51. Grisanti, L.; Sapunar, M.; Hassanali, A.; Došlić, N., Toward Understanding Optical Properties of Amyloids: A Reaction Path and Nonadiabatic Dynamics Study. *Journal of the American Chemical Society* **2020,** *142* (42), 18042-18049.
52. Shaban, H. A.; Valades-Cruz, C. A.; Savatier, J.; Brasselet, S., Polarized super-resolution structural imaging inside amyloid fibrils using Thioflavine T. *Scientific Reports* **2017,** *7* (1), 12482.
53. Xue, C.; Lin, T. Y.; Chang, D.; Guo, Z., Thioflavin T as an amyloid dye: fibril quantification, optimal concentration and effect on aggregation. *Royal Society Open Science* **2017,** *4* (1), 160696.
54. Obstarczyk, P.; Lipok, M.; Grelich-Mucha, M.; Samoć, M.; Olesiak-Bańska, J., Two-Photon Excited Polarization-Dependent Autofluorescence of Amyloids as a Label-Free Method of Fibril Organization Imaging. *The Journal of Physical Chemistry Letters* **2021,** *12* (5), 1432-1437.
55. Groenning, M., Binding mode of Thioflavin T and other molecular probes in the context of amyloid fibrils-current status. *J Chem Biol* **2010,** *3* (1), 1-18.
56. Duboisset, J.; Ferrand, P.; He, W.; Wang, X.; Rigneault, H.; Brasselet, S., Thioflavine-T and Congo Red Reveal the Polymorphism of Insulin Amyloid Fibrils When Probed by Polarization-Resolved Fluorescence Microscopy. *The Journal of Physical Chemistry B* **2013,** *117* (3), 784-788.
57. Ziaunys, M.; Sakalauskas, A.; Smirnovas, V., Identifying Insulin Fibril Conformational Differences by Thioflavin-T Binding Characteristics. *Biomacromolecules* **2020,** *21* (12), 4989-4997.
58. Arad, E.; Green, H.; Jelinek, R.; Rapaport, H., Revisiting thioflavin T (ThT) fluorescence as a marker of protein fibrillation - The prominent role of electrostatic interactions. *J Colloid Interface Sci* **2020,** *573*, 87-95.
59. Xu, M.-m.; Ren, W.-m.; Tang, X.-c.; Hu, Y.-h.; Zhang, H.-y., Advances in development of fluorescent probes for detecting amyloid-β aggregates. *Acta Pharmacologica Sinica* **2016,** *37* (6), 719-730.
60. Biancalana, M.; Koide, S., Molecular mechanism of Thioflavin-T binding to amyloid fibrils. *Biochim Biophys Acta* **2010,** *1804* (7), 1405-1412.
61. Liu, H.; Yang, J.; Wang, L.; Xu, Y.; Zhang, S.; Lv, J.; Ran, C.; Li, Y., Targeting β-amyloid plaques and oligomers: development of near-IR fluorescence imaging probes. *Future Med Chem* **2017,** *9* (2), 179-198.
62. Miller-Thomas, M. M.; Sipe, A. L.; Benzinger, T. L. S.; McConathy, J.; Connolly, S.; Schwetye, K. E., Multimodality Review of Amyloid-related Diseases of the Central Nervous System. *RadioGraphics* **2016,** *36* (4), 1147-1163.
63. Biga, L.; Quick, D.; Dawson, S.; Harwell, A.; Hopkins, R.; Kaufmann, J.; LeMaster, M.; Matern, P.; Morrison-Graham, K.; Runyeon, J., *Anatomy & Physiology*. Oregon State Open Educational Resources: 2019.
64. Walter, A.; Paul-Gilloteaux, P.; Plochberger, B.; Sefc, L.; Verkade, P.; Mannheim, J. G.; Slezak, P.; Unterhuber, A.; Marchetti-Deschmann, M.; Ogris, M.; Bühler, K.; Fixler, D.; Geyer, S. H.; Weninger, W. J.; Glösmann, M.; Handschuh, S.; Wanek, T., Correlated Multimodal Imaging in Life Sciences: Expanding the Biomedical Horizon. *Frontiers in Physics* **2020,** *8*.

65. Liu, S.; Hoess, P.; Ries, J., Super-Resolution Microscopy for Structural Cell Biology. *Annual Review of Biophysics* **2022,** *51* (1), 301-326.
66. Ji, N.; Shroff, H.; Zhong, H.; Betzig, E., Advances in the speed and resolution of light microscopy. *Current Opinion in Neurobiology* **2008,** *18* (6), 605-616.
67. Franken, L. E.; Grünewald, K.; Boekema, E. J.; Stuart, M. C. A., A Technical Introduction to Transmission Electron Microscopy for Soft-Matter: Imaging, Possibilities, Choices, and Technical Developments. *Small* **2020,** *16* (14), 1906198.
68. Nienhaus, K.; Nienhaus, G. U., Where Do We Stand with Super-Resolution Optical Microscopy? *Journal of Molecular Biology* **2016,** *428* (2, Part A), 308-322.
69. Cao, J.; Zhu, B.; Zheng, K.; He, S.; Meng, L.; Song, J.; Yang, H., Recent Progress in NIR-II Contrast Agent for Biological Imaging. *Frontiers in Bioengineering and Biotechnology* **2020,** *7*.
70. Porter , K. R.; Claude , A.; Fullam , E. F., A STUDY OF TISSUE CULTURE CELLS BY ELECTRON MICROSCOPY : METHODS AND PRELIMINARY OBSERVATIONS. *Journal of Experimental Medicine* **1945,** *81* (3), 233-246.
71. Masters, B. R., History of the Electron Microscope in Cell Biology. In *eLS*.
72. Kapoor, V.; McCook, B. M.; Torok, F. S., An Introduction to PET-CT Imaging. *RadioGraphics* **2004,** *24* (2), 523-543.
73. van den Dries, K.; Fransen, J.; Cambi, A., Fluorescence CLEM in biology: historic developments and current super-resolution applications. *FEBS Letters* **2022,** *596* (19), 2486-2496.
74. Kim, J.; Piao, Y.; Hyeon, T., Multifunctional nanostructured materials for multimodal imaging, and simultaneous imaging and therapy. *Chemical Society Reviews* **2009,** *38* (2), 372-390.
75. Combes, G. F.; Fakhouri, H.; Moulin, C.; Girod, M.; Bertorelle, F.; Basu, S.; Ladouce, R.; Bakulić, M. P.; Maršić, Ž. S.; Russier-Antoine, I.; Brevet, P.-F.; Dugourd, P.; Krisko, A.; Trajković, K.; Radman, M.; Bonačić-Koutecký, V.; Antoine, R., Functionalized Au15 nanoclusters as luminescent probes for protein carbonylation detection. *Communications Chemistry* **2021,** *4* (1), 69.
76. Nonappa, Luminescent gold nanoclusters for bioimaging applications. *Beilstein J Nanotechnol* **2020,** *11*, 533-546.
77. Cendrowska, U.; Silva, P. J.; Ait-Bouziad, N.; Müller, M.; Guven, Z. P.; Vieweg, S.; Chiki, A.; Radamaker, L.; Kumar, S. T.; Fändrich, M.; Tavanti, F.; Menziani, M. C.; Alexander-Katz, A.; Stellacci, F.; Lashuel, H. A., Unraveling the complexity of amyloid polymorphism using gold nanoparticles and cryo-EM. *Proceedings of the National Academy of Sciences* **2020,** *117* (12), 6866-6874.
78. Algar, W. R.; Massey, M.; Rees, K.; Higgins, R.; Krause, K. D.; Darwish, G. H.; Peveler, W. J.; Xiao, Z.; Tsai, H.-Y.; Gupta, R.; Lix, K.; Tran, M. V.; Kim, H., Photoluminescent Nanoparticles for Chemical and Biological Analysis and Imaging. *Chemical Reviews* **2021,** *121* (15), 9243-9358.
79. Zhou, M.; Zeng, C.; Chen, Y.; Zhao, S.; Sfeir, M. Y.; Zhu, M.; Jin, R., Evolution from the plasmon to exciton state in ligand-protected atomically precise gold nanoparticles. *Nature Communications* **2016,** *7* (1), 13240.
80. Chakraborty, I.; Pradeep, T., Atomically Precise Clusters of Noble Metals: Emerging Link between Atoms and Nanoparticles. *Chemical Reviews* **2017,** *117* (12), 8208-8271.
81. Jin, R.; Zeng, C.; Zhou, M.; Chen, Y., Atomically Precise Colloidal Metal Nanoclusters and Nanoparticles: Fundamentals and Opportunities. *Chemical Reviews* **2016,** *116* (18), 10346-10413.

82. Kang, X.; Li, Y.; Zhu, M.; Jin, R., Atomically precise alloy nanoclusters: syntheses, structures, and properties. *Chemical Society Reviews* **2020,** *49* (17), 6443-6514.
83. Mahmoudi, M., Debugging Nano–Bio Interfaces: Systematic Strategies to Accelerate Clinical Translation of Nanotechnologies. *Trends in Biotechnology* **2018,** *36* (8), 755-769.
84. Schaaff, T. G.; Knight, G.; Shafigullin, M. N.; Borkman, R. F.; Whetten, R. L., Isolation and Selected Properties of a 10.4 kDa Gold:Glutathione Cluster Compound. *The Journal of Physical Chemistry B* **1998,** *102* (52), 10643-10646.
85. Ingram, R. S.; Hostetler, M. J.; Murray, R. W., Poly-hetero-ω-functionalized Alkanethiolate-Stabilized Gold Cluster Compounds. *Journal of the American Chemical Society* **1997,** *119* (39), 9175-9178.
86. Negishi, Y.; Nobusada, K.; Tsukuda, T., Glutathione-Protected Gold Clusters Revisited: Bridging the Gap between Gold(I)−Thiolate Complexes and Thiolate-Protected Gold Nanocrystals. *Journal of the American Chemical Society* **2005,** *127* (14), 5261-5270.
87. Kang, X.; Zhu, M., Transformation of Atomically Precise Nanoclusters by Ligand-Exchange. *Chemistry of Materials* **2019,** *31* (24), 9939-9969.
88. Kang, X.; Zhu, M., Tailoring the photoluminescence of atomically precise nanoclusters. *Chemical Society Reviews* **2019,** *48* (8), 2422-2457.
89. Walter, M.; Akola, J.; Lopez-Acevedo, O.; Jadzinsky, P. D.; Calero, G.; Ackerson, C. J.; Whetten, R. L.; Grönbeck, H.; Häkkinen, H., A unified view of ligand-protected gold clusters as superatom complexes. *Proceedings of the National Academy of Sciences* **2008,** *105* (27), 9157-9162.
90. Zhu, M.; Aikens, C. M.; Hollander, F. J.; Schatz, G. C.; Jin, R., Correlating the Crystal Structure of A Thiol-Protected Au25 Cluster and Optical Properties. *Journal of the American Chemical Society* **2008,** *130* (18), 5883-5885.
91. Rambukwella, M.; Sakthivel, N. A.; Delcamp, J. H.; Sementa, L.; Fortunelli, A.; Dass, A., Ligand Structure Determines Nanoparticles' Atomic Structure, Metal-Ligand Interface and Properties. *Frontiers in Chemistry* **2018,** *6* (330).
92. Jin, R.; Zhu, Y.; Qian, H., Quantum-Sized Gold Nanoclusters: Bridging the Gap between Organometallics and Nanocrystals. *Chemistry – A European Journal* **2011,** *17* (24), 6584-6593.
93. Schmidbaur, H.; Schier, A., Aurophilic interactions as a subject of current research: an up-date. *Chemical Society Reviews* **2012,** *41* (1), 370-412.
94. Jin, R., Atomically precise metal nanoclusters: stable sizes and optical properties. *Nanoscale* **2015,** *7* (5), 1549-1565.
95. Yu, Y.; Chen, X.; Yao, Q.; Yu, Y.; Yan, N.; Xie, J., Scalable and Precise Synthesis of Thiolated Au10–12, Au15, Au18, and Au25 Nanoclusters via pH Controlled CO Reduction. *Chemistry of Materials* **2013,** *25* (6), 946-952.
96. Dolamic, I.; Knoppe, S.; Dass, A.; Bürgi, T., First enantioseparation and circular dichroism spectra of Au38 clusters protected by achiral ligands. *Nature Communications* **2012,** *3* (1), 798.
97. Negishi, Y.; Hashimoto, S.; Ebina, A.; Hamada, K.; Hossain, S.; Kawawaki, T., Atomic-level separation of thiolate-protected metal clusters. *Nanoscale* **2020,** *12* (15), 8017-8039.
98. Li, Y.; Higaki, T.; Du, X.; Jin, R., Chirality and Surface Bonding Correlation in Atomically Precise Metal Nanoclusters. *Advanced Materials* **2020,** *32* (41), 1905488.
99. Kang, X.; Chong, H.; Zhu, M., Au25(SR)18: the captain of the great nanocluster ship. *Nanoscale* **2018,** *10* (23), 10758-10834.
100. Heaven, M. W.; Dass, A.; White, P. S.; Holt, K. M.; Murray, R. W., Crystal Structure of the Gold Nanoparticle [N(C8H17)4][Au25(SCH2CH2Ph)18]. *Journal of the American Chemical Society* **2008,** *130* (12), 3754-3755.

101. Olesiak-Banska, J.; Waszkielewicz, M.; Obstarczyk, P.; Samoc, M., Two-photon absorption and photoluminescence of colloidal gold nanoparticles and nanoclusters. *Chemical Society Reviews* **2019,** *48* (15), 4087-4117.
102. Mitsui, M.; Arima, D.; Uchida, A.; Yoshida, K.; Arai, Y.; Kawasaki, K.; Niihori, Y., Charge-Transfer-Mediated Mechanism Dominates Oxygen Quenching of Ligand-Protected Noble-Metal Cluster Photoluminescence. *The Journal of Physical Chemistry Letters* **2022,** *13* (40), 9272-9278.
103. Wang, Y.; Bürgi, T., Ligand exchange reactions on thiolate-protected gold nanoclusters. *Nanoscale Advances* **2021**.
104. Si, S.; Gautier, C.; Boudon, J.; Taras, R.; Gladiali, S.; Bürgi, T., Ligand Exchange on Au25 Cluster with Chiral Thiols. *The Journal of Physical Chemistry C* **2009,** *113* (30), 12966-12969.
105. Chen, Y.; Zeng, C.; Kauffman, D. R.; Jin, R., Tuning the Magic Size of Atomically Precise Gold Nanoclusters via Isomeric Methylbenzenethiols. *Nano Letters* **2015,** *15* (5), 3603-3609.
106. Zhu, S.; Wang, X.; Cong, Y.; Li, L., Regulating the Optical Properties of Gold Nanoclusters for Biological Applications. *ACS Omega* **2020,** *5* (36), 22702-22707.
107. Pyo, K.; Thanthirige, V. D.; Kwak, K.; Pandurangan, P.; Ramakrishna, G.; Lee, D., Ultrabright Luminescence from Gold Nanoclusters: Rigidifying the Au(I)–Thiolate Shell. *Journal of the American Chemical Society* **2015,** *137* (25), 8244-8250.
108. Wu, Z.; Jin, R., On the Ligand's Role in the Fluorescence of Gold Nanoclusters. *Nano Letters* **2010,** *10* (7), 2568-2573.
109. Sperling, R. A.; Rivera Gil, P.; Zhang, F.; Zanella, M.; Parak, W. J., Biological applications of gold nanoparticles. *Chemical Society Reviews* **2008,** *37* (9), 1896-1908.
110. Porret, E.; Le Guével, X.; Coll, J.-L., Gold nanoclusters for biomedical applications: toward in vivo studies. *Journal of Materials Chemistry B* **2020,** *8* (11), 2216-2232.
111. Xiao, H.; Li, P.; Tang, B., Recent progresses in fluorescent probes for detection of polarity. *Coordination Chemistry Reviews* **2021,** *427*, 213582.
112. Tavanti, F.; Pedone, A.; Menziani, M. C.; Alexander-Katz, A., Computational Insights into the Binding of Monolayer-Capped Gold Nanoparticles onto Amyloid-β Fibrils. *ACS Chemical Neuroscience* **2020,** *11* (19), 3153-3160.
113. Lai, L.; Zhao, C.; Li, X.; Liu, X.; Jiang, H.; Selke, M.; Wang, X., Fluorescent gold nanoclusters for in vivo target imaging of Alzheimer's disease. *RSC Advances* **2016,** *6* (36), 30081-30088.
114. Brach, K.; Waszkielewicz, M.; Olesiak-Banska, J.; Samoc, M.; Matczyszyn, K., Two-Photon Imaging of 3D Organization of Bimetallic AuAg Nanoclusters in DNA Matrix. *Langmuir* **2017,** *33* (36), 8993-8999.
115. Hou, K.; Zhao, J.; Wang, H.; Li, B.; Li, K.; Shi, X.; Wan, K.; Ai, J.; Lv, J.; Wang, D.; Huang, Q.; Wang, H.; Cao, Q.; Liu, S.; Tang, Z., Chiral gold nanoparticles enantioselectively rescue memory deficits in a mouse model of Alzheimer's disease. *Nature Communications* **2020,** *11* (1), 4790.
116. Zheng, J.; Zhou, C.; Yu, M.; Liu, J., Different sized luminescent gold nanoparticles. *Nanoscale* **2012,** *4* (14), 4073-4083.
117. Shang, L.; Dörlich, R. M.; Brandholt, S.; Schneider, R.; Trouillet, V.; Bruns, M.; Gerthsen, D.; Nienhaus, G. U., Facile preparation of water-soluble fluorescent gold nanoclusters for cellular imaging applications. *Nanoscale* **2011,** *3* (5), 2009-2014.
118. Martikainen, M.; Salorinne, K.; Lahtinen, T.; Malola, S.; Permi, P.; Häkkinen, H.; Marjomäki, V., Hydrophobic pocket targeting probes for enteroviruses. *Nanoscale* **2015,** *7* (41), 17457-17467.

119. Zhou, M.; Du, X.; Wang, H.; Jin, R., The Critical Number of Gold Atoms for a Metallic State Nanocluster: Resolving a Decades-Long Question. *ACS Nano* **2021,** *15* (9), 13980-13992.
120. Svoboda, K.; Yasuda, R., Principles of Two-Photon Excitation Microscopy and Its Applications to Neuroscience. *Neuron* **2006,** *50* (6), 823-839.
121. Li, J.-B.; Liu, H.-W.; Fu, T.; Wang, R.; Zhang, X.-B.; Tan, W., Recent Progress in Small-Molecule Near-IR Probes for Bioimaging. *Trends in Chemistry* **2019,** *1* (2), 224-234.
122. Zipfel, W. R.; Williams, R. M.; Webb, W. W., Nonlinear magic: multiphoton microscopy in the biosciences. *Nature Biotechnology* **2003,** *21* (11), 1369-1377.
123. Golovynskyi, S.; Golovynska, I.; Stepanova, L. I.; Datsenko, O. I.; Liu, L.; Qu, J.; Ohulchanskyy, T. Y., Optical windows for head tissues in near-infrared and short-wave infrared regions: Approaching transcranial light applications. *Journal of Biophotonics* **2018,** *11* (12), e201800141.
124. Lefort, C., A review of biomedical multiphoton microscopy and its laser sources*. *Journal of Physics D: Applied Physics* **2017,** *50* (42), 423001.
125. Göppert-Mayer, M., Über Elementarakte mit zwei Quantensprüngen. *Annalen der Physik* **1931,** *401* (3), 273-294.
126. Kaiser, W.; Garrett, C. G. B.; Wood, D. L., Fluorescence and Optical Maser Effects in Ca${\mathrm{F}}_{2}$: ${\mathrm{Sm}}^{++}$. *Physical Review* **1961,** *123* (3), 766-776.
127. Denk, W.; Strickler, J. H.; Webb, W. W., Two-Photon Laser Scanning Fluorescence Microscopy. *Science (New York, N.Y.)* **1990,** *248* (4951), 73-76.
128. Pascal, S.; David, S.; Andraud, C.; Maury, O., Near-infrared dyes for two-photon absorption in the short-wavelength infrared: strategies towards optical power limiting. *Chemical Society Reviews* **2021,** *50* (11), 6613-6658.
129. Xu, L.; Zhang, J.; Yin, L.; Long, X.; Zhang, W.; Zhang, Q., Recent progress in efficient organic two-photon dyes for fluorescence imaging and photodynamic therapy. *Journal of Materials Chemistry C* **2020,** *8* (19), 6342-6349.
130. Murugan, N. A.; Zaleśny, R.; Kongsted, J.; Nordberg, A.; Ågren, H., Promising two-photon probes for in vivo detection of β amyloid deposits. *Chemical Communications* **2014,** *50* (79), 11694-11697.
131. Bertorelle, F.; Moulin, C.; Soleilhac, A.; Comby-Zerbino, C.; Dugourd, P.; Russier-Antoine, I.; Brevet, P.-F.; Antoine, R., Bulky Counterions: Enhancing the Two-Photon Excited Fluorescence of Gold Nanoclusters. *ChemPhysChem* **2018,** *19* (2), 165-168.
132. Bonačić-Koutecký, V.; Antoine, R., Enhanced two-photon absorption of ligated silver and gold nanoclusters: theoretical and experimental assessments. *Nanoscale* **2019,** *11* (26), 12436-12448.
133. Olesiak-Banska, J.; Gordel, M.; Kolkowski, R.; Matczyszyn, K.; Samoc, M., Third-Order Nonlinear Optical Properties of Colloidal Gold Nanorods. *The Journal of Physical Chemistry C* **2012,** *116* (25), 13731-13737.
134. Olesiak-Banska, J.; Waszkielewicz, M.; Matczyszyn, K.; Samoc, M., A closer look at two-photon absorption, absorption saturation and nonlinear refraction in gold nanoclusters. *RSC Advances* **2016,** *6* (101), 98748-98752.
135. Pniakowska, A.; Kumaranchira Ramankutty, K.; Obstarczyk, P.; Perić Bakulić, M.; Sanader Maršić, Ž.; Bonačić-Koutecký, V.; Bürgi, T.; Olesiak-Bańska, J., Gold-Doping Effect on Two-Photon Absorption and Luminescence of Atomically Precise Silver Ligated Nanoclusters. *Angewandte Chemie International Edition* **2022,** *61* (43), e202209645.
136. Russier-Antoine, I.; Bertorelle, F.; Calin, N.; Sanader, Ž.; Krstić, M.; Comby-Zerbino, C.; Dugourd, P.; Brevet, P.-F.; Bonačić-Koutecký, V.; Antoine, R., Ligand-core NLO-phores: a

combined experimental and theoretical approach to the two-photon absorption and two-photon excited emission properties of small-ligated silver nanoclusters. *Nanoscale* **2017,** *9* (3), 1221-1228.
137. Ramakrishna, G.; Varnavski, O.; Kim, J.; Lee, D.; Goodson, T., Quantum-sized gold clusters as efficient two-photon absorbers. *J Am Chem Soc* **2008,** *130* (15), 5032-3.
138. Russier-Antoine, I.; Bertorelle, F.; Hamouda, R.; Rayane, D.; Dugourd, P.; Sanader, Ž.; Bonačić-Koutecký, V.; Brevet, P.-F.; Antoine, R., Tuning Ag29 nanocluster light emission from red to blue with one and two-photon excitation. *Nanoscale* **2016,** *8* (5), 2892-2898.
139. Zhou, M.; Song, Y., Origins of Visible and Near-Infrared Emissions in [Au25(SR)18]− Nanoclusters. *The Journal of Physical Chemistry Letters* **2021,** *12* (5), 1514-1519.
140. Cao, Y.; Fung, V.; Yao, Q.; Chen, T.; Zang, S.; Jiang, D.-e.; Xie, J., Control of single-ligand chemistry on thiolated Au25 nanoclusters. *Nature Communications* **2020,** *11* (1), 5498.
141. Knoppe, S.; Häkkinen, H.; Verbiest, T.; Clays, K., Role of Donor and Acceptor Substituents on the Nonlinear Optical Properties of Gold Nanoclusters. *The Journal of Physical Chemistry C* **2018,** *122* (7), 4019-4028.
142. Mizuta, Y., Advances in Two-Photon Imaging in Plants. *Plant and Cell Physiology* **2021,** *62* (8), 1224-1230.
143. Matsuura, R.; Miyagawa, S.; Fukushima, S.; Goto, T.; Harada, A.; Shimozaki, Y.; Yamaki, K.; Sanami, S.; Kikuta, J.; Ishii, M.; Sawa, Y., Intravital imaging with two-photon microscopy reveals cellular dynamics in the ischeamia-reperfused rat heart. *Scientific Reports* **2018,** *8* (1), 15991.
144. Yamaguchi, K.; Kitamura, R.; Kawakami, R.; Otomo, K.; Nemoto, T., In vivo two-photon microscopic observation and ablation in deeper brain regions realized by modifications of excitation beam diameter and immersion liquid. *PLOS ONE* **2020,** *15* (8), e0237230.
145. Chen, C.; Liang, Z.; Zhou, B.; Li, X.; Lui, C.; Ip, N. Y.; Qu, J. Y., In Vivo Near-Infrared Two-Photon Imaging of Amyloid Plaques in Deep Brain of Alzheimer's Disease Mouse Model. *ACS Chemical Neuroscience* **2018,** *9* (12), 3128-3136.
146. Aliyan, A.; Cook, N. P.; Martí, A. A., Interrogating Amyloid Aggregates using Fluorescent Probes. *Chemical Reviews* **2019,** *119* (23), 11819-11856.
147. Nesterov, E. E.; Skoch, J.; Hyman, B. T.; Klunk, W. E.; Bacskai, B. J.; Swager, T. M., In Vivo Optical Imaging of Amyloid Aggregates in Brain: Design of Fluorescent Markers. *Angewandte Chemie International Edition* **2005,** *44* (34), 5452-5456.
148. Kim, H. M.; Yang, W. J.; Kim, C. H.; Park, W.-H.; Jeon, S.-J.; Cho, B. R., Two-Photon Dyes Containing Heterocyclic Rings with Enhanced Photostability. *Chemistry – A European Journal* **2005,** *11* (21), 6386-6391.
149. Calvo-Rodriguez, M.; Hou, S. S.; Snyder, A. C.; Dujardin, S.; Shirani, H.; Nilsson, K. P. R.; Bacskai, B. J., In vivo detection of tau fibrils and amyloid β aggregates with luminescent conjugated oligothiophenes and multiphoton microscopy. *Acta Neuropathologica Communications* **2019,** *7* (1), 171.
150. Hanczyc, P.; Samoc, M.; Norden, B., Multiphoton absorption in amyloid protein fibres. *Nature Photonics* **2013,** *7* (12), 969-972.
151. Johansson, P. K.; Koelsch, P., Label-free imaging of amyloids using their intrinsic linear and nonlinear optical properties. *Biomed. Opt. Express* **2017,** *8* (2), 743-756.
152. Li, L.; Lv, Z.; Man, Z.; Xu, Z.; Wei, Y.; Geng, H.; Fu, H., Polarity-active NIR probes with strong two-photon absorption and ultrahigh binding affinity of insulin amyloid fibrils. *Chemical Science* **2021,** *12* (9), 3308-3313.

153. Pedersen, C. J., The Discovery of Crown Ethers (Noble Lecture). *Angewandte Chemie International Edition in English* **1988,** *27* (8), 1021-1027.
154. Nicoli, F.; Baroncini, M.; Silvi, S.; Groppi, J.; Credi, A., Direct synthetic routes to functionalised crown ethers. *Organic Chemistry Frontiers* **2021,** *8* (19), 5531-5549.
155. Chehardoli, G.; Bahmani, A., The role of crown ethers in drug delivery. *Supramolecular Chemistry* **2019,** *31* (4), 221-238.
156. Al-Kahtani, A. A.; Al-Jallal, N. A.; El-Azhary, A. A., Conformational and vibrational analysis of 18-crown-6–alkali metal cation complexes. *Spectrochimica Acta Part A: Molecular and Biomolecular Spectroscopy* **2014,** *132*, 70-83.
157. Zhou, D.; Hao, H.; Ma, Y.; Zhong, H.; Dai, Y. n.; Cai, K.; Mukherjee, S.; Liu, J.; Bian, H., Specific Host–Guest Interactions in the Crown Ether Complexes with K+ and NH4+ Revealed from the Vibrational Relaxation Dynamics of the Counteranion. *The Journal of Physical Chemistry B* **2020,** *124* (41), 9154-9162.
158. Pérez, C.; López, J. C.; Blanco, S.; Schnell, M., Water-Induced Structural Changes in Crown Ethers from Broadband Rotational Spectroscopy. *The Journal of Physical Chemistry Letters* **2016,** *7* (20), 4053-4058.
159. Gámez, F.; Avilés-Moreno, J. R.; Berden, G.; Oomens, J.; Martínez-Haya, B., Proton in the ring: spectroscopy and dynamics of proton bonding in macrocycle cavities. *Physical Chemistry Chemical Physics* **2021,** *23* (38), 21532-21543.
160. Weirich, L.; Merten, C., Induced VCD and conformational chirality in host–guest complexes of a chiral ammonium salt with crown ethers. *Physical Chemistry Chemical Physics* **2021,** *23* (34), 18300-18307.
161. Móczár, I.; Huszthy, P., Optically active crown ether-based fluorescent sensor molecules: A mini-review. *Chirality* **2019,** *31* (2), 97-109.
162. Kralj, M.; Tušek-Božić, L.; Frkanec, L., Biomedical Potentials of Crown Ethers: Prospective Antitumor Agents. *ChemMedChem* **2008,** *3* (10), 1478-1492.
163. Mohammadzadeh Kakhki, R., Application of crown ethers as stationary phase in the chromatographic methods. *Journal of Inclusion Phenomena and Macrocyclic Chemistry* **2013,** *75* (1), 11-22.
164. Hill, A. P.; Kunstmann-Olsen, C.; Grzelczak, M. P.; Brust, M., Entropy-Driven Reversible Agglomeration of Crown Ether Capped Gold Nanoparticles. *Chemistry – A European Journal* **2018,** *24* (13), 3151-3155.
165. Kunstmann-Olsen, C.; Belić, D.; Bradley, D. F.; Danks, S. P.; Diaz Fernandez, Y. A.; Grzelczak, M. P.; Hill, A. P.; Qiao, X.; Raval, R.; Sorzabal-Bellido, I.; Brust, M., Ion shuttling between emulsion droplets by crown ether modified gold nanoparticles. *Nanoscale Advances* **2021**.
166. Mutihac, R.-C.; Buschmann, H.-J.; Schollmeyer, E., Influence of polar solvents upon the complex formation of 18-crown-6 with cations in chloroform. *Journal of Inclusion Phenomena and Macrocyclic Chemistry* **2010,** *68* (3), 411-416.
167. Baghdasaryan, A.; Brun, E.; Wang, Y.; Salassa, G.; Lacour, J.; Bürgi, T., Combined spectroscopic studies on post-functionalized Au25 cluster as an ATR-FTIR sensor for cations. *Chemical Science* **2021,** *12* (21), 7419-7427.
168. Baghdasaryan, A.; Brun, E.; Wang, Y.; Salassa, G.; Lacour, J.; Bürgi, T., Combined spectroscopic studies on post-functionalized Au25 cluster as an ATR-FTIR sensor for cations. *Chemical Science* **2021**.

169. Tian, Y.; Zhang, X.; Li, Y.; Shoup, T. M.; Teng, X.; Elmaleh, D. R.; Moore, A.; Ran, C., Crown ethers attenuate aggregation of amyloid beta of Alzheimer's disease. *Chemical communications (Cambridge, England)* **2014,** *50* (99), 15792-5.
170. Basu, A., Examining the effect of the crown ether, 18-crown-6, on lysozyme fibrillation. *New Journal of Chemistry* **2023,** *47* (6), 2924-2931.
171. Agrawal, N.; Skelton, A. A., 12-Crown-4 Ether Disrupts the Patient Brain-Derived Amyloid-β-Fibril Trimer: Insight from All-Atom Molecular Dynamics Simulations. *ACS Chemical Neuroscience* **2016,** *7* (10), 1433-1441.
172. Azubel, M.; Koivisto, J.; Malola, S.; Bushnell, D.; Hura, G. L.; Koh, A. L.; Tsunoyama, H.; Tsukuda, T.; Pettersson, M.; Häkkinen, H.; Kornberg, R. D., Electron microscopy of gold nanoparticles at atomic resolution. *Science (New York, N.Y.)* **2014,** *345* (6199), 909-912.
173. Brasselet, S., Polarization-resolved nonlinear microscopy: application to structural molecular and biological imaging. *Adv. Opt. Photon.* **2011,** *3* (3), 205.
174. Le Floc'h, V.; Brasselet, S.; Roch, J.-F.; Zyss, J., Monitoring of Orientation in Molecular Ensembles by Polarization Sensitive Nonlinear Microscopy. *The Journal of Physical Chemistry B* **2003,** *107* (45), 12403-12410.
175. Olesiak-Banska, J.; Mojzisova, H.; Chauvat, D.; Zielinski, M.; Matczyszyn, K.; Tauc, P.; Zyss, J., Liquid crystal phases of DNA: Evaluation of DNA organization by two-photon fluorescence microscopy and polarization analysis. *Biopolymers* **2011,** *95* (6), 365-375.
176. Olesiak-Banska, J.; Gordel, M.; Matczyszyn, K.; Shynkar, V.; Zyss, J.; Samoc, M., Gold nanorods as multifunctional probes in a liquid crystalline DNA matrix. *Nanoscale* **2013,** *5* (22), 10975-10981.
177. Mojzisova, H.; Olesiak, J.; Zielinski, M.; Matczyszyn, K.; Chauvat, D.; Zyss, J., Polarization-Sensitive Two-Photon Microscopy Study of the Organization of Liquid-Crystalline DNA. *Biophysical Journal* **2009,** *97* (8), 2348-2357.
178. Obstarczyk, P.; Lipok, M.; Żak, A.; Cwynar, P.; Olesiak-Bańska, J., Amyloid fibrils in superstructures – local ordering revealed by polarization analysis of two-photon excited autofluorescence. *Biomaterials Science* **2022,** *10* (6), 1554-1561.
179. Rao, J.; Dragulescu-Andrasi, A.; Yao, H., Fluorescence imaging in vivo: recent advances. *Current Opinion in Biotechnology* **2007,** *18* (1), 17-25.
180. Sulatsky, M. I.; Sulatskaya, A. I.; Povarova, O. I.; Antifeeva, I. A.; Kuznetsova, I. M.; Turoverov, K. K., Effect of the fluorescent probes ThT and ANS on the mature amyloid fibrils. *Prion* **2020,** *14* (1), 67-75.
181. Ivana, S.; Margherita, B.; Gaetano, I.; Clara, I., Intrinsic blue-green fluorescence in amyloyd fibrils. *AIMS Biophysics* **2018,** *5* (2), 155-165.
182. Pansieri, J.; Josserand, V.; Lee, S.-J.; Rongier, A.; Imbert, D.; Sallanon, M. M.; Kövari, E.; Dane, T. G.; Vendrely, C.; Chaix-Pluchery, O.; Guidetti, M.; Vollaire, J.; Fertin, A.; Usson, Y.; Rannou, P.; Coll, J.-L.; Marquette, C.; Forge, V., Ultraviolet–visible–near-infrared optical properties of amyloid fibrils shed light on amyloidogenesis. *Nature Photonics* **2019,** *13* (7), 473-479.
183. Serpell, L. C.; Sunde, M.; Benson, M. D.; Tennent, G. A.; Pepys, M. B.; Fraser, P. E., The protofilament substructure of amyloid fibrils11Edited by F. E. Cohen. *Journal of Molecular Biology* **2000,** *300* (5), 1033-1039.
184. Rogers, S. S.; Krebs, M. R.; Bromley, E. H.; van der Linden, E.; Donald, A. M., Optical microscopy of growing insulin amyloid spherulites on surfaces in vitro. *Biophys J* **2006,** *90* (3), 1043-54.

185. Cannon, D.; Eichhorn, S. J.; Donald, A. M., Structure of Spherulites in Insulin, β-Lactoglobulin, and Amyloid β. *ACS Omega* **2016,** *1* (5), 915-922.
186. Ishigaki, M.; Morimoto, K.; Chatani, E.; Ozaki, Y., Exploration of Insulin Amyloid Polymorphism Using Raman Spectroscopy and Imaging. *Biophysical Journal* **2020,** *118* (12), 2997-3007.
187. Diociaiuti, M.; Bonanni, R.; Cariati, I.; Frank, C.; D'Arcangelo, G., Amyloid Prefibrillar Oligomers: The Surprising Commonalities in Their Structure and Activity. *International journal of molecular sciences* **2021,** *22* (12).
188. Ragonis-Bachar, P.; Landau, M., Functional and pathological amyloid structures in the eyes of 2020 cryo-EM. *Current Opinion in Structural Biology* **2021,** *68*, 184-193.
189. Exley, C.; House, E.; Collingwood, J. F.; Davidson, M. R.; Cannon, D.; Donald, A. M., Spherulites of Amyloid-β 42 In Vitro and in Alzheimer's Disease. *Journal of Alzheimer's Disease* **2010,** *20*, 1159-1165.
190. Thorlaksen, C.; Stanciu, A.-M.; Busch Neergaard, M.; S. Hatzakis, N.; Foderà, V.; Groenning, M., Morphological integrity of insulin amyloid-like aggregates depends on preparation methods and post-production treatments. *European Journal of Pharmaceutics and Biopharmaceutics* **2022,** *179*, 147-155.
191. Vetri, V.; Piccirilli, F.; Krausser, J.; Buscarino, G.; Łapińska, U.; Vestergaard, B.; Zaccone, A.; Foderà, V., Ethanol Controls the Self-Assembly and Mesoscopic Properties of Human Insulin Amyloid Spherulites. *The Journal of Physical Chemistry B* **2018,** *122* (12), 3101-3112.
192. Savastano, A.; Jaipuria, G.; Andreas, L.; Mandelkow, E.; Zweckstetter, M., Solid-state NMR investigation of the involvement of the P2 region in tau amyloid fibrils. *Scientific Reports* **2020,** *10* (1), 21210.
193. Bhattacharya, A.; Bhowmik, S.; Singh, A. K.; Kodgire, P.; Das, A. K.; Mukherjee, T. K., Direct Evidence of Intrinsic Blue Fluorescence from Oligomeric Interfaces of Human Serum Albumin. *Langmuir* **2017,** *33* (40), 10606-10615.
194. Huang, Y.; Chen, W.; Chung, J.; Yin, J.; Yoon, J., Recent progress in fluorescent probes for bacteria. *Chemical Society Reviews* **2021,** *50* (13), 7725-7744.
195. Oren, O.; Taube, R.; Papo, N., Amyloid β structural polymorphism, associated toxicity and therapeutic strategies. *Cellular and Molecular Life Sciences* **2021,** *78* (23), 7185-7198.
196. Kaur, A.; New, E. J.; Sunde, M., Strategies for the Molecular Imaging of Amyloid and the Value of a Multimodal Approach. *ACS Sensors* **2020,** *5* (8), 2268-2282.
197. Pawlicki, M.; Collins, H. A.; Denning, R. G.; Anderson, H. L., Two-Photon Absorption and the Design of Two-Photon Dyes. *Angewandte Chemie International Edition* **2009,** *48* (18), 3244-3266.
198. Su, D.; Diao, W.; Li, J.; Pan, L.; Zhang, X.; Wu, X.; Mao, W., Strategic Design of Amyloid-β Species Fluorescent Probes for Alzheimer's Disease. *ACS Chemical Neuroscience* **2022,** *13* (5), 540-551.
199. Bielak, K.; Hołubowicz, R.; Zoglowek, A.; Żak, A.; Kędzierski, P.; Ożyhar, A.; Dobryszycki, P., N'-terminal- and Ca2+-induced stabilization of high-order oligomers of full-length Danio rerio and Homo sapiens otolin-1. *International Journal of Biological Macromolecules* **2022,** *209*, 1032-1047.
200. Żak, A. M., Light-Induced In Situ Transmission Electron Microscopy–Development, Challenges, and Perspectives. *Nano Letters* **2022,** *22* (23), 9219-9226.
201. Kundu, S.; Ghosh, B.; Nandi, S.; Ghosh, M.; Pyne, A.; Chatterjee, J.; Sarkar, N., Surface Ligand-Controlled Wavelength-Tunable Luminescence of Gold Nanoclusters: Cellular Imaging

and Smart Fluorescent Probes for Amyloid Detection. *ACS Applied Bio Materials* **2020,** *3* (7), 4282-4293.
202. Yang, Y.; Wang, S.; Chen, S.; Shen, Y.; Zhu, M., Switching the subcellular organelle targeting of atomically precise gold nanoclusters by modifying the capping ligand. *Chemical Communications* **2018,** *54* (66), 9222-9225.
203. Kunstmann-Olsen, C.; Belić, D.; Bradley, D. F.; Danks, S. P.; Diaz Fernandez, Y. A.; Grzelczak, M. P.; Hill, A. P.; Qiao, X.; Raval, R.; Sorzabal-Bellido, I.; Brust, M., Ion shuttling between emulsion droplets by crown ether modified gold nanoparticles. *Nanoscale Advances* **2021,** *3* (11), 3136-3144.
204. Grzelczak, M. P.; Hill, A. P.; Belic, D.; Bradley, D. F.; Kunstmann-Olsen, C.; Brust, M., Design of artificial membrane transporters from gold nanoparticles with controllable hydrophobicity. *Faraday Discussions* **2016,** *191* (0), 495-510.
205. Ghosh, A.; Udayabhaskararao, T.; Pradeep, T., One-Step Route to Luminescent Au18SG14 in the Condensed Phase and Its Closed Shell Molecular Ions in the Gas Phase. *The Journal of Physical Chemistry Letters* **2012,** *3* (15), 1997-2002.
206. Stamplecoskie, K. G.; Chen, Y.-S.; Kamat, P. V., Excited-State Behavior of Luminescent Glutathione-Protected Gold Clusters. *The Journal of Physical Chemistry C* **2014,** *118* (2), 1370-1376.
207. Rurack, K.; Spieles, M., Fluorescence Quantum Yields of a Series of Red and Near-Infrared Dyes Emitting at 600−1000 nm. *Analytical Chemistry* **2011,** *83* (4), 1232-1242.
208. Agrawal, N.; Skelton, A. A., Binding of 12-Crown-4 with Alzheimer's Aβ40 and Aβ42 Monomers and Its Effect on Their Conformation: Insight from Molecular Dynamics Simulations. *Molecular Pharmaceutics* **2018,** *15* (1), 289-299.
209. Agrawal, N.; Skelton, A. A., 12-Crown-4 Ether Disrupts the Patient Brain-Derived Amyloid-β-Fibril Trimer: Insight from All-Atom Molecular Dynamics Simulations. *ACS Chem Neurosci* **2016,** *7* (10), 1433-1441.
210. Obstarczyk, P.; Pniakowska, A.; Nonappa; Grzelczak, M. P.; Olesiak-Bańska, J., Crown Ether-Capped Gold Nanoclusters as a Multimodal Platform for Bioimaging. *ACS Omega* **2023,** *8* (12), 11503-11511.
211. Cheng, H.-W.; Rustenholtz, A.; Porter, R. A.; Ye, X. R.; Wai, C. M., Partition Coefficients and Equilibrium Constants of Crown Ethers between Water and Organic Solvents Determined by Proton Nuclear Magnetic Resonance. *Journal of Chemical & Engineering Data* **2004,** *49* (3), 594-598.
212. Nickolov, Z. S.; Ohno, K.; Matsuura, H., FTIR-ATR Studies of the Hydration of 15-Crown-5 and 18-Crown-6 in Aqueous Solutions. *The Journal of Physical Chemistry A* **1999,** *103* (37), 7544-7551.
213. López, J. C.; Pérez, C.; Blanco, S.; Shubert, V. A.; Temelso, B.; Shields, G. C.; Schnell, M., Water induces the same crown shapes as Li+ or Na+ in 15-crown-5 ether: a broadband rotational study. *Physical Chemistry Chemical Physics* **2019,** *21* (6), 2875-2881.
214. Aikens, C. M., Electronic and Geometric Structure, Optical Properties, and Excited State Behavior in Atomically Precise Thiolate-Stabilized Noble Metal Nanoclusters. *Accounts of Chemical Research* **2018,** *51* (12), 3065-3073.

Appendix

List of publications included in this dissertation:

1. Obstarczyk, P.; Lipok, M.; Grelich-Mucha, M.; Samoć, M.; Olesiak-Bańska, J., Two-Photon Excited Polarization-Dependent Autofluorescence of Amyloids as a Label-Free Method of Fibril Organization Imaging. *The Journal of Physical Chemistry Letters* **2021,** *12* (5), 1432-1437.

2. Obstarczyk, P.; Lipok, M.; Żak, A.; Cwynar, P.; Olesiak-Bańska, J., Amyloid fibrils in superstructures – local ordering revealed by polarization analysis of two-photon excited autofluorescence. *Biomaterials Science* **2022,** *10* (6), 1554-1561.

3. Obstarczyk, P.; Pniakowska, A.; Nonappa; Grzelczak, M. P.; Olesiak-Bańska, J., Crown Ether-Capped Gold Nanoclusters as a Multimodal Platform for Bioimaging. *ACS Omega* **2023,** *8* (12), 11503-11511.

List of publications not included in this dissertation:

1. Olesiak-Banska, J.; Waszkielewicz, M.; Obstarczyk, P.; Samoc, M., Two-photon absorption and photoluminescence of colloidal gold nanoparticles and nanoclusters. *Chemical Society Reviews* **2019,** *48* (15), 4087-4117.

2. Deska, R.; Obstarczyk, P.; Matczyszyn, K.; Olesiak-Bańska, J., Circular Dichroism of Gold Bipyramid Dimers. *The Journal of Physical Chemistry Letters* **2021**, 5208-5213.

3. Pniakowska, A.; Kumaranchira Ramankutty, K.; Obstarczyk, P.; Perić Bakulić, M.; Sanader Maršić, Ž.; Bonačić-Koutecký, V.; Bürgi, T.; Olesiak-Bańska, J., Gold-Doping Effect on Two-Photon Absorption and Luminescence of Atomically Precise Silver Ligated Nanoclusters. *Angewandte Chemie International Edition* **2022,** *61* (43), e202209645.

4. Lipok, M.; Obstarczyk, P.; Parzyszek, S.; Wang, Y.; Bagiński, M.; Buergi, T.; Lewandowski, W.; Olesiak-Bańska, J., Circularly Polarized Luminescence from Atomically Precise Gold Nanoclusters Helically Assembled by Liquid-Crystal Template. *Advanced Optical Materials* **2023,** *11* (3), 2201984

5. Ciesielski, K.; Synoradzki, K.; Szymański, D.; Tobita, K.; Berent, K.; Obstarczyk, P.; Kimura, K.; Kaczorowski, D., Half-Heusler phase TmNiSb under pressure: intrinsic phase separation, thermoelectric performance and structural transition. *Scientific Reports* **2023,** *13* (1), 1592.

List of grants:

1. **Laureate of the PRELUDIUM** - Polish National Science Centre grant (03.2023 – 28.02.2025, 2022/45/N/ST5/01510) - "Gold nanoclusters capped with crown ethers as smart markers with enhanced functionality for two-photon bio-imaging". Total amount granted: 139 600.00 PLN.

Role: Project leader.

2. **Laureate of the Bekker NAWA Programme** (edition 2021) – scholarship granted to implement the project entitled “Atomically precise gold nanoclusters functionalized by charged, zwitterionic and supramolecular ligands”, at Carnegie Mellon University, Department of Chemistry (Pittsburgh, USA). Total amount granted: 66 000.00 PLN.

Role: Project leader – canceled due to the pandemic regulations.

3. **Research project** - **FNP First TEAM/2017-3/27 -**: “Nonlinear Optics, Nanoparticles and Amyloids” (21.02.2018 – 28.02.2022). Project leader: Joanna Olesiak-Bańska. Wroclaw University of Science and Technology.

Role: Stipendist (PhD student).

4. **Research project** - 2019/34/E/ST5/00276 NCN (National Science Centre in Poland): "Atomically precise gold nanoclusters as new probes in single-photon and multiphoton imaging". (01.08.2023 – 30.09.2023). Project leader: Joanna Olesiak-Bańska. Wroclaw University of Science and Technology.

Role: Stipendist (PhD student).

List of internships:

1. 24.06.2020 - 24.07.2020 - Université de Genève, Faculté des Sciences (**Genève, Switzerland**). Supervisor: Thomas Bürgi.
2. 01.11.2021 – 31.12.2021 - Tampere University, Faculty of Engineering and Natural Sciences (**Tampere, Finland**). Supervisor: Nonappa.
3. 26.07.2022 - 30.07.2022 – University of Warsaw, Faculty of Chemistry (**Warsaw, Poland**). Supervisor: Wiktor Lewandowski.

List of international conferences:

1. P. Obstarczyk , A. Żak , J. Olesiak-Bańska, K. Matczyszyn, Synthesis of elongated gold plasmonic nanoparticles with designed optical properties, 4 th Metallic Nano Objects Workshop (MNO 2018), 5-7.11.2018, Lyon, Villeurbanne, France - **poster**.

2. P. Obstarczyk , R. Deska , A. Żak , J. Olesiak-Bańska, K. Matczyszyn, Plasmonic spindle-like gold nanoparticles and their optical characterization, The 11th International

Conference on Nanophotonics (ICNP 2018), PhoBiA Annual Nanophotonics International Conference 2018 (PANIC 2018), 2–6.07.2018, Wrocław, Poland – **poster and oral presentation**.

3. P. Obstarczyk, A. Żak, J. Olesiak-Bańska, Synthesis pathways of non-spherical gold plasmonic nanoparticles – an overview, PhoBiA Annual Nanophotonics International Conference 2019 (PANIC 2019), 2019, 15-17.05.2019, Wrocław, Poland – **poster**.

4. P. Obstarczyk, K. Nadolski, A. M. Żak, K. Matczyszyn, J. Olesiak-Bańska, Shape-dependent linear and nonlinear optical properties of elongated plasmonic gold nanoparticles, Sixth International Conference on Multifunctional, Hybrid and Nanomaterials, 11-15.03.2019, Sitges, Spain - **poster**.

5. P. Obstarczyk, M. Waszkielewicz, R. Kazan, T. Bürgi, M. Samoć, J. Olesiak-Bańska, Multi-photon excited properties of gold nanoclusters, Toward Atomic Precision in Nanochemistry: from Synthesis to Function, 9-14.02.2020, Galveston, United States – **poster**.

6. P. Obstarczyk, M. Lipok, A. M. Żak, J. Olesiak-Bańska, Probing of amyloid structure – microscopy and nanoparticles, S3IC 2020 Single-Molecule Sensors and NanoSystems International Conference, 9-11.11.2020, Barcelona, Spain (online) – **oral (flash) presentation**.

7. P. Obstarczyk, Maciej Lipok, A. M. Żak, J. Olesiak-Bańska, Polarization-sensitive microscopy of amyloid superstructures – spherulites, PhoBiA Annual Nanophotonics International Conference (PANIC 2020), 12-14.10.2020, Wrocław, Poland – **oral presentation.**

8. P. Obstarczyk, A. Pniakowska, M.P. Grzelczak, J. Olesiak-Bańska, Amphiphilic markers for bio-imaging: gold nanoclusters and amyloids under TEM and fluorescence examination, European Light Microscopy Initiative Meeting (ELMI 2021), 22-25.06.2021, Oxford, Great Britain, virtual conference (online) – **poster**.

9. P. Obstarczyk, A. Pniakowska, Nonappa, M.P. Grzelczak, J. Olesiak-Bańska, Noncovalent intramolecular forces – gold nanoparticles ligand chemistry and amyloid fibrils interfaces, PANIC Summer School 2022 : PhoBiA Annual Nanophotonics International Conference, 30.05- 3.06.2022, Wrocław, Poland – **oral presentation**.

List of awards:

1. An honorable distinction in Max Born scholarship program of Wroclaw Academic Hub (WCA) - and the president of Wroclaw (2021 edition) – physical and chemical sciences.
2. Laureate of Jan Mozrzymas scholarship of Wroclaw Academic Hub (WCA) and the president of Wroclaw (2022 edition) - interdisciplinary research.

3. Laureate of Award of the Rector of Wrocław University of Science and Technology for outstanding scientific achievements (2022 edition).
4. Laure of PRIMUS award granted by Wrocław University of Science and Technology for high impact scientific publications (2022, 2023 editions).
5. Laureate of FNP (Foundation for Polish Science) START scholarship - stipends for young, and talented researchers – category: materials science (2023 edition).